Mixed Polyanion and Clathrate Materials as Novel Materials for Lithium-ion and Sodium-ion Batteries

by

Ran Zhao

A Dissertation Presented in Partial Fulfillment
of the Requirements for the Degree
Doctor of Philosophy

Approved April 2017 by the
Graduate Supervisory Committee:

Candace K. Chan, Chair
Daniel Buttry
Jeffery Yarger

ARIZONA STATE UNIVERSITY

May 2017

ABSTRACT

This work describes the investigation of novel cathode and anode materials. Specifically, several mixed polyanion compounds were evaluated as cathodes for Li and Na-ion batteries. Clathrate compounds composed of silicon or germanium arranged in cage-like structures were studied as anodes for Li-ion batteries.

Nanostructured $Cu_4(OH)_6SO_4$ (brochantite) platelets were synthesized using polymer-assisted titration and microwave-assisted hydrothermal methods. These nanostructures exhibited a capacity of 474 mAh/g corresponding to the full utilization of the copper redox in an conversion reaction. X-ray diffraction (XRD) and X-ray photoelectron spectroscopy (XPS) studies were preformed to understand the mechanism and structural changes.

A microwave hydrothermal synthesis was developed to prepare a series compounds based on jarosite, $AM_3(SO_4)_2(OH)_6$ (A = K, Na; M = Fe, V). Both the morphology and electrochemical properties showed a compositional dependence. At potentials >1.5 V vs. Li/Li^+, an insertion-type reaction was observed in Na,Fe-jarosite but not in K,Fe-jarosite. Reversible insertion-type reactions were observed in both vanadium jarosites between 1 – 4 V with capacities around 40 - 60 mAh/g. Below 1 V vs. Li/Li^+, all four jarosite compounds underwent conversion reactions with capacities ~500 mAh/g for the Fe-jarosites.

The electrochemical properties of hydrogen titanium phosphate sulfate, $H_{0.4}Ti_2(PO_4)_{2.4}(SO_4)_{0.6}$ (HTPS), a new mixed polyanion material with NASICON structure was reported. A capacity of 148 mAh/g corresponding to2 Li^+ insertion per formula unit was observed. XRD and XPS were used to characterize the HTPS before and after cycling and to identify the lithium sites. Evaluation of the HTPS in Na-ion cell was also performed, and a discharge capacity of 93 mAh/g was observed.

A systematic investigation of the role of the processing steps, such as ball-milling and acid/base etching, on the electrochemical properties of a silicon clathrate compound with nominal composition of $Ba_8Al_{16}Si_{30}$ was performed. According to the transmission electron microscope (TEM), XPS, and electrochemical analysis, very few Li atoms can be electrochemically inserted, but the introduction of disorder through ball-milling resulted in higher capacity, while the oxidation layer made by the acid/base treatment prevented the reation. The electrochemical property of germanium clathrate was also investigated, unlike the silicon clathrate, the germanium one underwent a conversion reaction.

To my parents Yongsheng and Chunzhi, for your love and support, let me free to do what I want. Dad, you have set an example for me.

To my grandparents, especially grandpa, you are always in my heart.

To my husband, Hanyu, for your love.

To my little girl, Yang; I did it…so can you!

ACKNOWLEDGMENTS

I would like to thank my advisor, Prof. Candace K. Chan, for her help, guidance and patience over the course of my academic career. Prof. Chan is always the guiding star when I am confused or lost. Her passion, dedication and incredible drive are truly inspirational; she has set an example of an independent female scientist, and I could have not done it without her supervision.

I am also grateful to my committee members, Prof. Daniel Buttry, Prof. Jeff Yarger and my oral committee members Prof. Karl Sieradzki and Prof. Don Seo, for their time and valuable suggestion.

Special thanks to all my friends and colleagues that worked with me side by side. Thanks to Qian Cheng, Ting Yang, Man Li and Ying Li for discussing the problems I met in all projects, thanks to Chenchen Bing for the accompany during the first two years in my Ph.D program, thanks to my friends, Xiying Chen and Ke Geng. Finally, I want to thank Daniel Mieritz for providing HTPS materials and sample characterization information, Ting Yang for taking the TEM images and Jon Weller for Raman spectroscopy.

Funding from the American Chemical Society Petroleum Research Fund (52830-DNI10) for the polyanion work and National Science Foundation (DMR-1206795) for the clathrate work is gratefully appreciated. I also gratefully acknowledge the use of the John M. Cowley Center for High Resolution Electron Microscopy, the facilities within the LeRoy Eyring Center for Solid State Science and the Goldwater Environmental Laboratory at Arizona State University.

TABLE OF CONTENTS

Page

CHAPTER Page

LIST OF TABLES

Table Page

LIST OF FIGURES

Figure Page

Figure Page

Figure Page

Figure Page

Figure Page

Figure Page

Figure Page

1: INTRODUCTION

1.1 Lithium-ion Batteries

As the world becomes increasingly reliant on electronic devices, it also comes more dependent on the batteries, especially the rechargeable batteries. A rechargeable battery is known as a secondary cell because its electrochemical reactions are electrically reversible and can recharged and used multiple times. In the rechargeable battery, several different types have been commercialized and used in all aspects of human life, including: lead-acid, nickel cadmium (NiCd), nickel metal hydride (NiMH), lithium-ion, and lithium ion polymer batteries. Among them, Lithium-ion batteries will become the world's leading rechargeable battery technology, particularly because of the high energy density and low self-discharge. The comparison of the energy density of the different kinds of batteries is listed in Figure 1.1.[1]

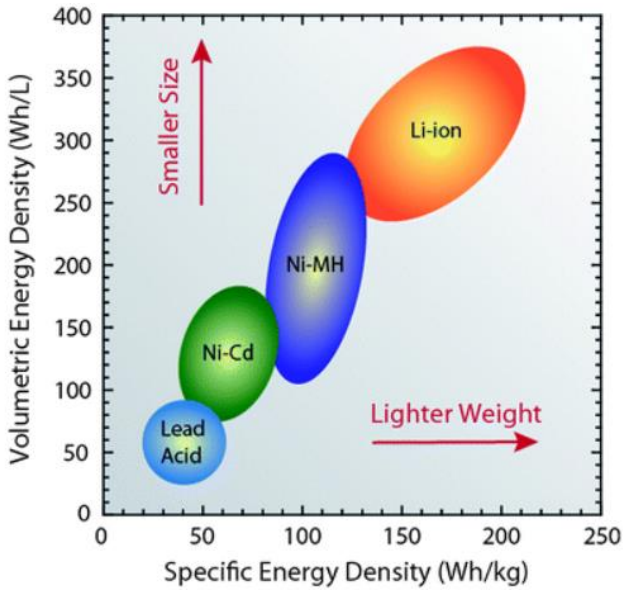

Figure 1. 1 Comparison of energy density in battery cells.

Lithium was incorporated into battery technology as it is the most electropositive (-3.04 V vs. standard hydrogen electrode) and lightest (specific gravity 0.53 $g.cm^{-3}$) metal which benefits the high energy density[2]. In 1970, the reversible Li intercalation reaction with layered transition-metal sulfides and selenides were first explored by Jean Rouxel[3]. Since the reversible reaction is needed in the rechargeable battery, Brian Steele[4] suggested that TiS_2 could be a candidate for a rechargeable lithium-ion battery, and in 1976, TiS_2 was used as a cathode with lithium metal as an anode for the first time by Whittingham[5]. Due to side reactions caused mainly by reduction or oxidation of solvents at the surface of anodes and cathodes, a solid electrolyte interfaces (SEI) layer will be formed, unfortunately, the SEI layer prevents uniform plating of Li and forms dendrites on repeated charging, which can grow across the separator and cause an internal short-circuit, or even explosion, so that the Li cell cannot be used safely. However, the fabrication of a discharged cathode $LiMO_2$ (M = Cr, Co, Ni) by Goodenough[6–8] and the exploration of Li intercalation into graphite by Yazami[9] avoids the problem of dendrite formation, therefore the Li metal is no longer needed, and the concept of the Li-ion battery was established.

There are three primary functional components in a lithium-ion battery, which are the cathode, anode and the electrolyte, which provides a conductive medium for lithium ions to move between the electrodes. Electrical energy flows out of or into the battery when electrons flow though the external circuit during discharge or charge. Both electrodes allow lithium ions to move in and out of their structure. During discharge, the lithium ions move from the anode to cathode, and when the cell in charging, the reverse occurs as shown in **Figure 1.2**.[10]

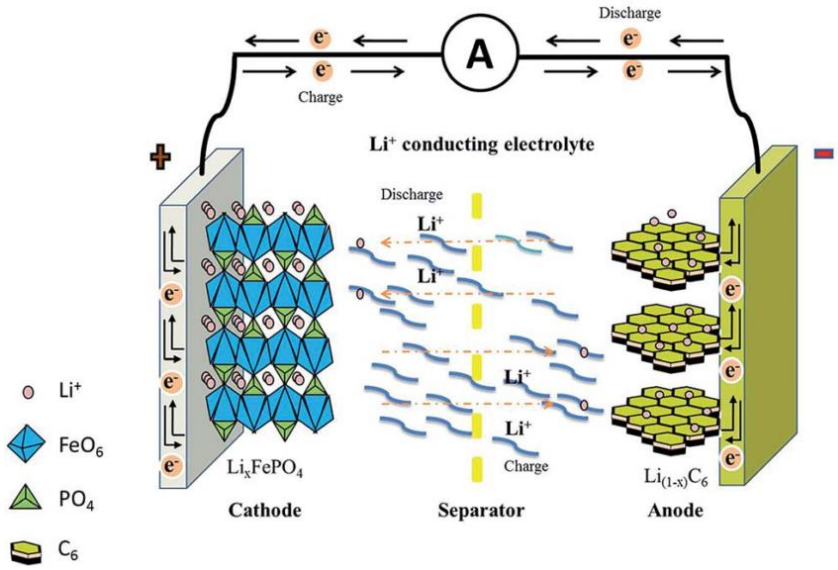

Figure 1. 2 Schematic illustration of a typical lithium-ion battery.[10]

In order to value the electrochemical properties of an electrode material, parameters such as voltage, capacity and energy density are used.

The voltage across the cell under open circuit conditions can be calculated from the balance between the chemical and electrical driving forces according to the Nernst equation[11]:

$$\mathrm{E} = -(^{RT}/_{z_i F})\ln[^{a_{i(+)}}/_{a_{i(-)}}] \quad (1.1)$$

Where R is the gas constant (8.315J•mol^{-1}•K^{-1}), T is the absolute temperature, z_i is the number of charge carried by species i, F is the Faraday constant (96485 C•mol^{-1}), $a_{i(+)}$ is the activity in the positive electrode and $a_{i(-)}$ for the activity in the negative electrode.

By applying the *Gibbs Phase Rule*, the voltage across an electrochemical cell with the state of charge has been investigated[11].

$$F = C - P + 2 \quad (1.2)$$

In which *F* is the number of degrees of freedom, *C* is the number of components, and *P* is the number of phases. The thermodynamic parameters considered are intensive variables, which are temperature, overall pressure, and the chemical potential or chemical composition of each of the phases present. For instance, for a reaction involving two phases: A+B→ AB, there are two phases: B and AB, and two elements A and B present in an electrode, so *P* is 2 and *C* also equals to 2; thus *F* is equal to 2. That means if the values of two intensive thermodynamic parameters, like temperature and pressure are specified, no degrees of freedom are left, suggesting that all the intensive properties are all defined, so the potential of the electrode does not vary with the state of charge as shown in **Figure 1.3A (**Adapted from ref[11]**)**.

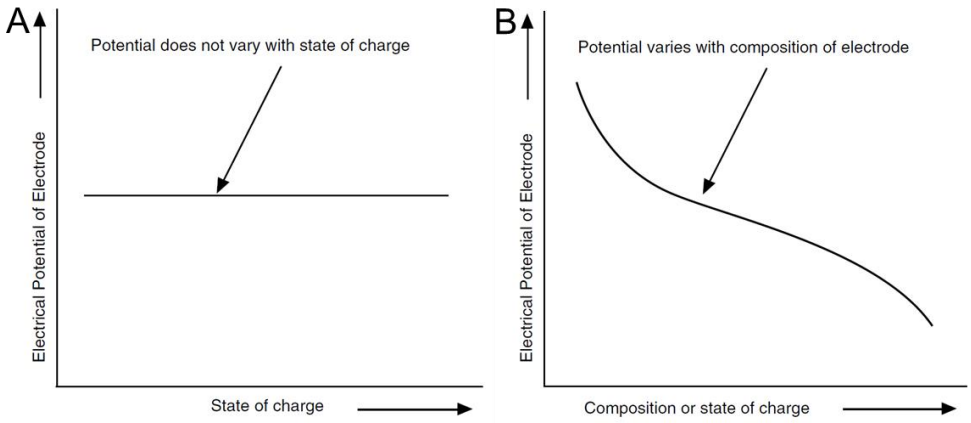

Figure 1. 3 Schematic representation of the potential as a function of its composition for a (A) two phase reaction (B) one phase reaction.

If some guest species could dissolve in the host phase, forming a solid solution, the number of components would be two, and in a solid solution, there is only one phase; therefore, the degree of freedom equals three. That means after defining two thermodynamic parameters, temperature and pressure, there is a residual of F, which should

be the potential; thus the potential should change with the different state of charge, as shown in **Figure 1.3B**.

Another parameter is capacity, which shows the amount of Li that can be stored reversibly in the electrode material. The gravimetric specific capacity (1.3) is typically used, but the volumetric specific capacity is also evaluated (1.4) when design a commercial battery.

$$C_g = {}^{1000xF}/_{3600M} \quad mAh/g \tag{1.3}$$

$$C_v = \rho C_g \qquad Ah/L \text{ or } mAh/cm^3 \tag{1.4}$$

Where *x* is the number of Li carried per unit formula, *F* is Faraday's constant (96485 $C.mol^{-1}$), M is the molar mass, ρ is the density.

The energy density, E, can be calculated by the reaction voltage and specific capacity:

$$E = VC \qquad Wh/kg \text{ or } Wh/L \tag{1.5}$$

Therefore, it is important to consider both reaction potential and capacity when developing new electrode materials for energy density improvement.

1.2 Cathodes

Existing Li-ion battery (LIB) technology is reaching its limit in energy density (per volume) and specific energy (per weight)[12]. The relatively low capacity of the electrodes (370 mAh/g for graphite carbon and 140–170 mAh/g for lithium metal oxide/phosphate) limit the total specific energy of the cell. To increase the energy density, great work has been devoted to finding high capacity electrode materials. On the anode side, silicon (highest known theoretical charge capacity 4,200mAh/g) has achieved the theoretical

charge capacity and maintain a discharge capacity close to 75% of this maximum by overcoming the structural degradation problems[13]. But the energy density gain of the battery utilizing silicon is limited to 30% due to the low capacity of cathode.

Since the commercialization of lithium-ion batteries in the 1990s[14], almost all of the research and commercialization of cathode materials has centered on two classes of materials[15]. The first class of materials contains $LiTiS_2$, $LiCoO_2$, $LiNi_{1-y}Co_yO_2$ and $LiNi_yMn_yCo_{1-2y}O_2$ etc.. Those materials are layered compounds with an anion close-packed lattice. In the alternate layers between the anion sheets are occupied by a transition metal and lithium then inserts into the empty remaining layers, while in the spinels the transition-metal are ordered in all the layers. Due to the compact lattices, the first group of materials have an inherent advantage of energy density per unit of volume. As shown in **Table 1.1**, the layered materials exhibit a theoretical capacity of 230 – 460 mAh/g (700 – 1300 mAh/cm^3), but the achieved capacities in the typical commercial cell are about half, with capacities of 180 – 210 mAh/g. The spinel materials shows an even lower capacity about 150 mAh/g theoretically, with achieved capacities of 84 – 120 mAh/g in commercial cells.

The second group of materials have more open structures, such as the vanadium oxides, manganese dioxides, and the transition-metal phosphates. Studies on fluorophosphates[16] , fluorosulfates[17,18], orthosilicates[19] and pyrophosphates[20] show that these materials have advantages such as environmental benignity, low cost, thermal stability, high voltage, and good cycle stability for LIBs. However, the theoretical capacities are even lower than the first group, about 150 - 170 mAh/g.

The capacity of cathode material has been improved as when it was first studied in 1970s, but is still well below the goal of one lithium per transition-metal ion[21]. Because of

the drawbacks of the intercalation-based cathode materials such as high cost, low actual capacity, toxicity and so on, there is a big need to replace it.

Table 1. 1 Theoretical and actual capacities, voltage of common cathode materials.[22]

Structure	Formula	Gravimetric capacity ($mAh.g^{-1}$) (theoretical/actual)	Volumetric capacity ($mAh.cm^{-3}$) (theoretical/actual)	Average voltage (V)[23]	
Layered	$LiTiS_2$	225/210 [24]	697	1.9	Commercialized
	$LiCoO_2$	274/148 [25]	1363/550	3.8	Commercialized
	$LiNiO_2$	275/150 [26]	1280	3.8	Research
	$LiMnO_2$	285/140 [27]	1148	3.3	Research
	$LiNi_{0.33}Mn_{0.33}Co_{0.33}O_2$	280/160 [22]	1333/600	3.7	Commercialized
	$LiNi_{0.8}Co_{0.15}Al_{0.05}O_2$	279/199 [28]	1284/700	3.7	Commercialized
	Li_2MnO_3	458/180 [29]	1708	3.8	Research
Spinel	$LiMn_2O_4$	148/120 [22]	596	4.1	Commercialized
	$LiCo_2O_4$	142/84 [30]	704	4.0	Research
Olivine	$LiFePO_4$	170/165 [31]	589	3.4	Commercialized
	$LiMnPO_4$	171/168 [32]	567	3.8	Research
	$LiCoPO_4$	167/125 [33]	510	4.2	Research
Tavorite	$LiFeSO_4F$	151/120 [34]	487	3.7	Research
	$LiVPO_4F$	156/129 [16]	484	4.2	Research

Recently, there has been much interest in materials that undergo conversion reactions upon reaction with lithium since these multi-electron processes can result in higher

theoretical capacities than conventional insertion electrodes. The generic form of a conversion reaction is shown in equation (1.6)[35]:

$$M_aX_b + (b \cdot n)\ Li \leftrightarrow aM + bLi_nX \quad (1.6)$$

Where M is a transition metal, X is the anion, and n is the formal oxidation state of X. This reaction can be described as conversion of the parent phase, M_aX_b, to the reduced metal, which is interspersed in a matrix phase, Li_nX,is typically electronically insulating.

Many Cu-containing materials such as copper oxides[36], vanadates[37–39], fluoride[40,41], chloride[42], thiospinels[43], phosphide[44,45], sulfate[46], and borate[47] have demonstrated conversion reactions upon lithiation with many varying results, while Fe-based conversion materials such as iron fluorides have shown promising cyclability when prepared as nanocomposites[41,48] or nanostructures[49,50].

For FeF_3 electrodes, Amatucci's group demonstrated a reversible conversion reaction with appreciable energy capacity[48,51,52]. They have proposed the following reaction schemes:

$$FeF_3 + Li \rightarrow LiFeF_3\ (4.5–2.5\ V) \quad (1.7)$$

$$LiFeF_3 + 2Li \rightarrow 3LiF + Fe\ (2.5–1.5\ V) \quad (1.8)$$

With reduction to the zero valence state of the metal, the capacity of FeF_3 can be as high as 700 mAh/g. However, these materials undergo large structural changes and experience voltage hysteresis that may impede commercial application.

1.3 Anode

Anode materials are required in Li-ion batteries as the dendrites formation from lithium metal batteries and the short-circuit and saftey issues make them unsuitable for commercial applications. According to the reaction machnism, anode materials can be classified to three groups: alloying, insertion and conversion, as shown in **Figure 1.4**.

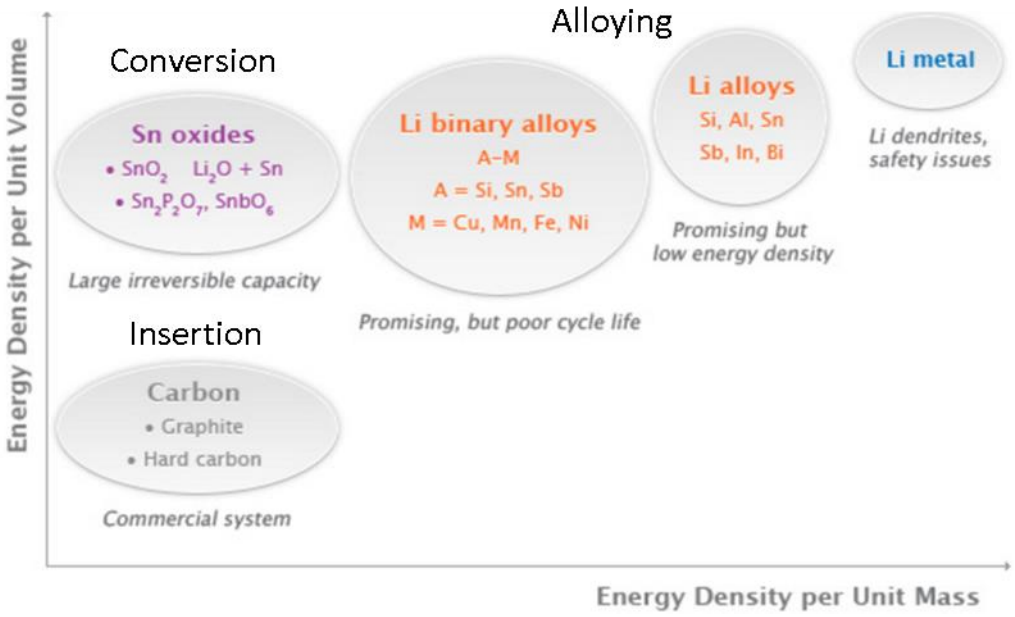

Figure 1. 4 Different groups of anode materials and the current issues.[53]

Li metal has the highest energy density per unit volume and mass, but because of the safety issue, it is not a good choice for anode material. In the case of Li alloy materials (Si, Ge, Sn, Al etc.) and conversion-based materials (CoO, Fe_2O_3 etc.), they are suffering the formation of SEI layers, large volume changes and poor cycle life. For the insertion-based materials (e.g. carbon and $Li_4Ti_5O_{12}$), the low capacity is the key factor which need to be improved (**Table 1.2**). The graphite carbon anode enabled the Li-ion battery to be used commercially more than 20 years ago, and still is the anode material of choice with the

advantages of long cycle life, abundant material supply and relatively low cost. However, the graphite anode is also suffering the disadvantages of low gravimetric (375 mAh/g)[54] and volumetric (330 – 430 mAh/cm^3) capacities, and safety issues related to lithium deposition. So, there has been a growing interest to develope new anode materials with higher energy density, low cost and long cycle life.

Table 1. 2 Comparison of the theoretical capacities, charge density, volume change and potential of different kinds of anode materials.[22,55]

Material	Lithiated phase	Theoretical capacity (mAh/g)	Potential vs. Li (V)	Volume change （%）
Li	Li	3862	0	100
C	LiC_6	372	0.05	12
Si	$Li_{4.4}Si$	4200	0.4	320
Ge	$Li_{4.4}Ge$	1623	0.5	240
Sn	$Li_{4.4}Sn$	994	0.6	260
Al	LiAl	993	0.3	96
$Li_4Ti_5O_{12}$	$Li_7Ti_5O_{12}$	175	1.6	1

1.4 Materials Characterization Techniques

1.4.1 X-ray Diffraction

X-ray diffraction is a unique technique for the determination of crystallinity in a compounds and can be primarily used for (1) characterization of crystalline materials, (2)

identification of fine-grained minerals such as clays and mixed layer clays that are difficult to determine optically, (3) determination of unit cell dimensions and (4) measurement of sample purity.[56] With specialized techniques, XRD is also used for the Rietveld refinement to obtain the detailed information such as element occupancies, cell parameters and isothermal parameters, and the crystallite size determination using the Scherrer equation.

In 1913, W. H. Bragg and his son W. L. Bragg developed a relationship to explain why the cleavage faces of crystals reflect X-ray beams at certain angles, which is know as the Bragg's law (1.9).

$$n\lambda = 2d\ sin\ \theta \tag{1.9}$$

Where n is an integer, λ is the wavelength of the incident x-ray beam, d is the distance between atomic layers in a crystal. For a crystalline sample with long range order structure, the signals will be shown as peaks in the XRD pattern, and for an amorphous material, X-rays will be randomly scattered which form a broad peak or even flat signal in a XRD pattern.

All the XRD analyses in this work were performed using a PANalytical X'Pert Pro high resolution X-ray diffractometer with the CuKα radiation. Powder samples were held by a zero background substrate, and the electrodes were stuck to the substrate. The lowest angle is 10° (2θ), with a step size of 0.025°.

1.4.2 Electron Microscopy

To evaluate the sample's morphology, scanning electron microscopy (SEM) was used. A SEM scans a focused electron beam over a surface to create an image. The beam of electrons is produced at the top of microscope by an electron gun. Once the beam hits the

sample, primary back-scattered electrons, secondary electrons, Auger electrons and X-rays[57] will be generated, which can be used to obtain the information such as the surface topography and composition. In this work, an XL30 Environmental FEG equipped with EDAX system was used. The powder samples were dispersed in ethanol by sonication. Then, several drops of the suspension were pipetted onto the surface of a clean Si wafer and dried. The electrodes samples were stuck to the sample tab using conducting carbon tape.

Transmission electron microscopy (TEM) collects transmitted electrons to obtain structure information. The TEM operates on the same basic principle as the light microscope but uses electrons whose wavelength is much smaller, so that the resolution is many orders of magnitude better than that from a light microscope. Thus, TEMs can reveal the finest details of internal structure, even the individual atoms. Therefore, TEM is very helpful to distinguish the amorphous and crystalline regions.

1.4.3 X-ray Photoelectron Spectroscopy

X-ray photoelectron spectroscopy (XPS) is the most widely used surface analysis technique which can provide the information such as the empirical formula, chemical state and electronic state. By combining XPS measurements with ion milling (sputtering), depth distribution information can be obtained.

XPS spectra are obtained by irradiating a surface with a beam of X-rays while measuring the kinetic energy and electrons emitted. The spectrum records the counts of the ejected electrons over a region of kinetic energies or binding energy, as shown in equation (1.10).

$$E_{binding} = E_{photon} - (E_{kinetic} + \Phi) \quad (1.10)$$

Where $E_{binding}$ is the binding energy of the electron, E_{photon} is the energy of X-ray photons, $E_{kinetic}$ is the kinetic energy of the electron being measured and Φ is the work function. The peaks that appear in the spectrum are used to identify the elements quantitatively. In this work, XPS was performed on a VG ESCALAB 220i-XL with Al Kα anode (E_{photon} = 1486.6 eV) operating at 60 W and 12 kV. A pass energy of 20 eV was used for high-resolution spectra. The spectra were calibrated to the hydrocarbon peak at 284.5 eV. Peak fitting was performed using CasaXPS processing software.

1.4.4 Wavelength-dispersive Spectroscopy

Wavelength-dispersive X-ray spectroscopy (WDS) is a technique used to count the number of X-rays of a specific wavelength diffracted by a crystal. The wavelength of the X-ray and the crystal are related by Bragg's law. Unlike the energy-dispersive X-ray spectroscopy, WDS only detects one wavelength a time, which can give more detailed and accurate information (**Fig. 1.5**). Because only X-rays of a given wavelength will enter the detector at one time, the electron microprobes typically have five spectrometers in order to work efficiently, allowing them to measure five elements simultaneously.

In this work, WDS was performed on a JEOL JXA-8530Ff equipped with five wavelength-dispersive spectrometers. The powder sample was mixed with epoxy and cured for two days at room temperature in a chemical hood. Then the sample was ground and polished to a flat surface for subsequent analysis. A 10 nA current with a 20 keV accelerating potential was used for the analysis. Seven spots were tested for each sample and the average values were discussed.

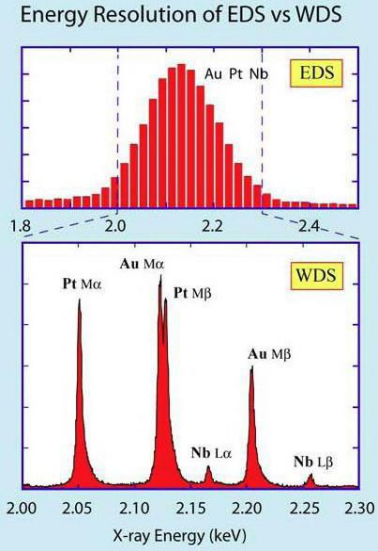

Figure 1. 5 A comparison of spectra collected form a Pt-Au-Nb alloy on an EDS/WDS system.

1.5 Electrochemical Characterization Techniques

1.5.1 Potentiodynamic Cycling with Galvanostatic Acceleration

Potentiodynamic cycling with galvanostatic acceleration (PCGA) is a technique in which the electrode cycles under stepwise potentiodynamic mode. The potential between the working electrode and reference electrode changes for a constant potential step, dE_s. The potential step amplitude (dE_s) and duration (dt_s) define the potential sweeps. By limiting the current or amount of charge, it is possible to go to the next step before the end of the last potential sweep (**Fig. 1.6**). The process is repeated until to the maximum set-up value, then the potential steps back to the minimum set-up value. If the potential step is small enough, the capacity of the tested material can be calculated.

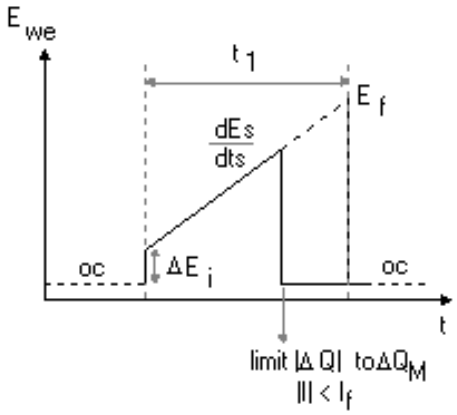

Figure 1. 6 One potential sweep of PCGA technique.[58]

PCGA can also be used to obtain the differential plots, -dQ/dV, as a function of potential. In a differential plot, there will be peaks at the voltage where the reaction occurs, providing a qualitative analysis of an electrochemical reaction.

1.5.2 Galvanostatic Cycling with Potential Limitation

Galvanostatic cycling with potential limitation (GCPL) is another technique which can be used to obtain the capacity of the electrode materials. Instead of potential steps, a constant current is applied between the working and reference electrodes (**Fig. 1.7**). After reaching the limit voltage or amount of charge, the current applies on the opposite direction, until reaching the other voltage limit or amount of charge. Because of the constant current, the capacity calculated from GCPL is more accurate than the value obtained by PCGA.

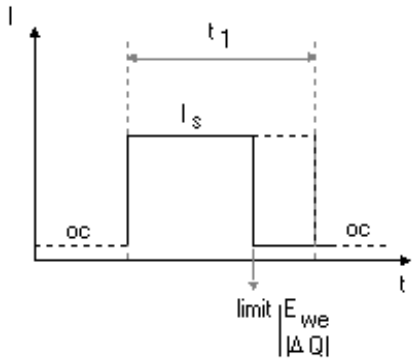

Figure 1. 7 A schematic representation of current applied in a GCPL measurement.

1.5.3 Galvanostatic Intermittent Titration

First described by Huggins and Weppner[59], the galvanostatic intermittent titration (GITT) technique is a powerful tool which can be employed to determine kinetic and thermodynamic information. The cell is discharged/charged with a constant current flux for an interval time followed by an open circuit rest, allowing the cell voltage to relax to its steady-state value. Assuming that the guest species transport in the electrode obeys Fick's second law, the chemical diffusion coefficients can be obtained by the following equation:

$$D = \frac{4}{\pi\tau}\left(\frac{mV_M}{M_w S}\right)^2 \left(\frac{\Delta E_s}{\Delta E_t}\right)^2, \; t \ll L^2/D \tag{1.11}$$

where D ($cm^2\ s^{-1}$) is the chemical diffusion coefficient, m is the mass of active material, V_M and M_w are the molar volume and weight, S is the active surface area of the electrode, τ was the time duration of the applied current, ΔE_s is the change in the steady-state voltage over the titration step, E is the voltage, t is the time and L is the thickness of the electrode.

1.5.4 Electrochemical Impedance Spectroscopy

Among the modern computational techniques, electrochemical impedance spectroscopy (EIS) has proven to be a powerful tool for examining many chemical and physical processes in solution as well as in solids. There are two types of impedance measurements: potentiostatic impedance (PEIS) and galvanostatic impedance (GEIS). The PEIS performs impedance measurements in potentiostatic mode by applying a sinus around a potential E that can be set to a fixed value relatively to the cell equilibrium potential. GEIS is very close to PEIS, except that the current is controlled instead of the potential.

The impedance spectra are usually evaluated by an equivalent circuit model to extract physically meaningful properties of the electrochemical system by modeling the data in terms of an electrical circuit composed of ideal resistor (R), capacitors (C), and Warburg (W). And for applications in lithium-ion batteries, the information such as solid state diffusion, charge transfer in the electrode and electrolyte interface, transfer through the SEI, electrode and current collector, electronic conductivity and lithium ion migration in the electrolyte can be obtained.

2: BROCHANTITE NANOPLATES AS CATHODE ELECTRODES FOR LITHIUM-ION BATTERIES

2.1 Introduction

Recently, there has been much interest in materials that undergo conversion reactions upon reaction with lithium since these multi-electron processes can result in higher theoretical capacities than conventional insertion electrodes. Many Cu-containing materials such as copper oxides[36], vanadates[37–39], fluoride[40,41], chloride[42], thiospinels[43], phosphide[44,45], sulfate[46], and borate[47] have demonstrated conversion reactions upon lithiation with many varying results. While Fe-based conversion materials such as iron fluorides have shown promising cyclability when prepared as nanocomposites[41,48] or nanostructures[49,50], the Cu analogs tend to show poorer reversibility. In some cases, the formation of large Cu nanoparticles[60] or even Cu dendrite extrusion is observed during discharge[39,43,61]. The formation of Cu metal deposits can improve the conductivity of the electrodes after discharge, but it can also promote irreversibility due to risk of Cu isolation from the electrode or dissolution into the electrolyte as soluble species during charging. For instance, the lithiation of CuF_2 is not reversible[40,41,60]. Recent studies on conversion reactions in nanostructured binary oxides and fluorides have shed new light on the role of electronic conductivity and relative diffusion rates of mobile cations (e.g. Cu^{1+}/Cu^{2+} vs. Li^+

mobility) and anions in the initial, intermediate and final phases found in conversion reactions, including the nucleation and growth mechanisms and the resulting morphologies found in the products[41,60]. For instance, in CuF_2, it is believed that the transport of F^- anions away from the Cu/CuF_2 interface may lead to formation of Cu nanoparticles completely isolated in the LiF matrix, which are unable to be oxidized during charging[60]. In contrast, CuO electrodes show much better reversibility and form only small 3 nm particles at the end of discharge, which may be attributed to the lower mobility of O^{2-} anions and Cu cations in CuO preventing large Cu dendrite formation. Despite the better cycling characteristics in CuO, its discharge potential of ~ 1.35 V vs. Li/Li^+[62] is too low for its application as a cathode and too high to be used as an anode in lithium-ion battery applications.

It is well established that the redox energies of metal ions can be tuned by an inductive effect introduced by the counter anions, with the electronegativity of X and the strength of the M−X bond playing a role in controlling the cell voltage. This has been frequently studied in polyanion and mixed anion materials such as $Fe_2(SO_4)_3$[63,64] and $Li(Fe_{1-\delta}Mn_\delta)SO_4F$[17]. In general, the less polarizable the anion (or ionic the M-X bonding), the higher the potential. The use of nanostructured materials has been found to be effective for promoting electron transport through these poorly conducting materials[65]. In this work, we

apply these strategies in order to obtain a more reversible, higher voltage Cu conversion electrode.

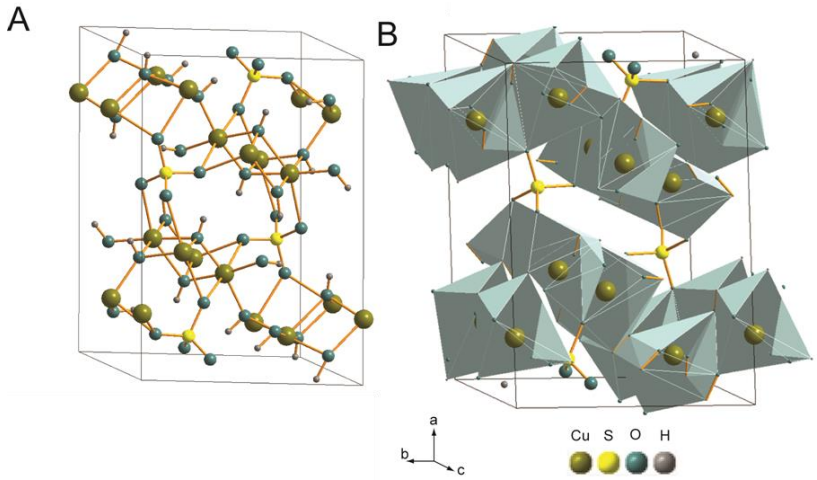

Figure 2. 1 Crystal structure of brochantite (A) ball-and-stick and (B) polyhedron representation.

Materials with sulfate and phosphate anions have been known to form a wide range of structural arrangements. For example, naturally occurring copper hydroxysulfate minerals of the form $M_x(OH)_y(SO_4)_n$ are found in a variety of expanded frameworks, tunnel, and layered structures[66]. Such structures may provide pathways for effective Li^+ diffusion, and the presence of mixed anions may be used to tune the redox potential of the metal and create different environments for Li^+ insertion. As a starting point, we have chosen to study the electrochemical properties of $Cu_4(OH)_6SO_4$ (**Fig. 2.1**). Also written as $CuSO_4 \cdot 3Cu(OH)_2$ and known as the mineral brochantite[67,68], this material is mostly

associated with corrosion products that impart the green color in patina layers[69–71], such as that found on the Statue of Liberty[70]. Brochantite has recently been studied for its magnetic properties[72,73] and as an electrocatalyst for oxidation of ascorbic acid[74], but has never been investigated as an electrode for lithium-ion battery applications.

Here we report the synthesis of brochantite using precipitation and microwave-assisted hydrothermal methods to produce different particle sizes and morphologies, including nanoplates. The electrochemical properties of the materials were evaluated in half-cells with Li metal counter electrodes. Capacities >400 mAh/g were observed for brochantite with nanoplate morphology. *Ex situ* X-ray diffraction (XRD), scanning electron microscopy (SEM), transmission electron microscopy (TEM), and X-ray photoelectron spectroscopy (XPS) were performed in order to characterize the structure and identify changes occurring during the electrochemical reactions. The fundamental knowledge gained from this study can be applied to better understanding of the electrochemical properties other mixed anion materials and add to the existing knowledge base related to Cu-based conversion electrodes for lithium-ion batteries.

2.2 Experimental Methods

2.2.1 Synthesis of Brochantite

Brochantite particles were synthesized using precipitation (P) or microwave hydrothermal (HT) techniques using as described as follows. After the synthesis, the blue-green powder was collected, washed with ethanol and water several times and dried at 50 ^{o}C overnight. Copper(II) sulfate, sodium hydroxide, and polyvinylpyrrolidone (MW = 29000) were obtained from Sigma-Aldrich and used as received.

2.2.1.1 Titration Method

Sample P: 15 mL of 0.1 M NaOH was titrated with stirring into a 15 mL solution of copper sulfate of the same concentration, based on the procedures in ref.[75].

Sample P-BM: Sample P was ball-milled for 10 min using a stainless steel grinding vial set.

Sample P-PVP1: 15 mL of 0.1M NaOH was titrated with stirring against a 15 mL solution of copper sulfate of the same concentration containing 0.621 g of PVP (n_{Cu2+}:n_{PVP}=70:1). Sample P-PVP2: 15 mL of 0.1 M NaOH was titrated with stirring against a solution of copper sulfate of the same concentration with 1.243 g PVP (n_{Cu2+}:n_{PVP}=35:1).

2.2.1.2 Microwave-assist Hydrothermal

Sample HT: Microwave-assisted hydrothermal treatment was performed on an aqueous suspension of $CuSO_4 \cdot 5H_2O$ and NaOH in molar proportions of Cu/Na/H_2O =

1/1.333/2222. The reactions were performed in vessels of volume 33 cm^3 with a 1/3 filling ratio. The precursor suspensions were heated to 170 ^oC within 10 min and were held for 5 min using a CEM Discover SP Reactor.

2.2.2 Materials Characterization

X-ray diffraction (XRD), scanning electron microscopy (SEM), transmission electron microscopy (TEM), and X-ray photoelectron spectroscopy (XPS) were used to perform structural characterization on the prepared brochantite powders, as well as the composite electrodes before and after cycling.

2.2.2.1 X-ray Diffraction

The electrodes were rinsed several times with ethanol and dried at 50℃ overnight. XRD data was collected using a Panalytical X'pert Pro with CuKα radiation operated at 40 kV/40 mA.

2.2.2.2 Electron Microscopy

Electron microscopy studies were performed using a XL 30 ESEM-FEG and a JEOL 2010F TEM. Powder samples were dispersed into ethanol with ultrasonication for 5 minutes and then dropped onto a Si wafer for SEM imaging or TEM grid. To mitigate charging, the brochantite samples were sputter coated with a thin layer of Au prior to SEM observation.

2.2.2.3 X-ray Photoelectron Spectroscopy

XPS was performed on a VG ESCALAB 220i-XL with Al Kα anode (1486.6eV) operated at 60 W and 12 kV. The X-ray takeoff angle was 45^o and the data was acquired

from the region within ~500μm of the outer surface of the sample. Charge compensator was used because brochantite is an insulator. A pass energy of 20 eV was used for high-resolution spectra (energy resolution 0.7 eV). The spectra were calibrated to the oxygen 2p peak at 531.8 eV instead of the typically used hydrocarbon peaks at 284.5 eV due to many different chemical environments for carbon in the electrodes (e.g. from PVDF, carbon black, dried electrolyte). Peak fitting was performed using CasaXPS processing software.

2.2.3 Electrochemical Measurement

Brochantite composite electrodes were prepared by mixing the brochantite active material with polyvinylidene difluoride (PVDF) binder (Kynar) and SuperP Li carbon black (TimCal) with a ratio of 70:10:20 by weight. N-methyl-2-pyrrolidone was added dropwise and the slurry was then stirred overnight to form a homogenous free-flowing paste. This slurry was then coated onto a piece of Al foil using an automated film coater equipped with a Meyer rod and dried in an oven at 110 ^{O}C for 1 h. The foil was then punched into disks and weighed prior to electrochemical testing.

Half cells were assembled in an argon-filed glove box using lithium metal foil as the anode, Celgard 2500 as separator, and 1 M $LiPF_6$ in EC: DMC (1:1 by vol, MTI) as electrolyte. Galvanostatic or potentiodynamic measurements were performed on a BioLogic VMP3 between 1 – 4 V vs. Li/Li^+. For galvanostatic measurements, C-rates were determined using a theoretical capacity of 474.13 mAh/g according to the 2 electron reduction for each of the 4 Cu (insertion of 8 Li^+) per brochantite formula unit. The current densities corresponding to the C-rates are as follows: C/20 (23.71 mA/g), C/10 (47.41

mA/g), C/5 (94.83 mA/g), C/2 (237.07 mA/g), 1C (474.13 mA/g). For potentiodynamic measurements, a 5 mV voltage step was used with a threshold current of 25 mA/mg of brochantite.

2.3 Results and Discussion

2.3.1 Structural Characterization

Synthetic brochantite is typically prepared using precipitation in alkaline solutions[76–78], although hydrothermal[72,79] and sonochemical methods[80] have also been reported. Because brochantite is a basic copper salt, it is easily obtained by precipitation from the titration of NaOH into a $CuSO_4$ solution. The morphologies of the as-prepared brochantite powders made by the precipitation method (sample P, **Fig. 2.2A**) were not uniform and ranged from hundreds of nanometers to as large as hundreds of microns. Ball-milling the material (sample P-BM, **Fig. 2.2B**) decreased the particle size to less than 10 microns.

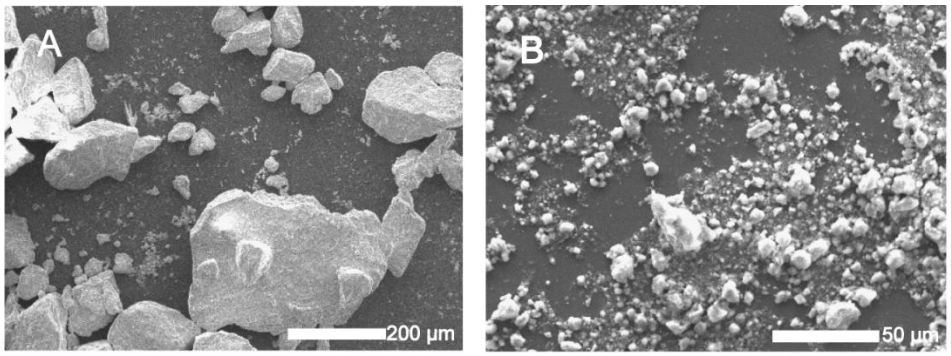

Figure 2. 2 SEM image of (A) sample P. (B) sample P-BM.

Since the uniformity and range of particle sizes was hard to control, polyvinylpyrrolidone (PVP) was applied as a structure directing agent at two different molar ratios with respect to the Cu^{2+}. PVP was chosen because it is a common polymer used to make shape-controlled nanostructures for many different materials, including brochantite nanorods[74]. Sample P-PVP1 (n_{Cu2+} : n_{PVP} = 70:1) consisted of thin plate-like nanostructures, but the sample was not very uniform (**Fig. 2.3A**). Some of the brochantite displayed tapered nanoplate morphology with triangular shaped ends, while other structures displayed hexagonal nanosheet morphology. Increasing the amount of PVP (n_{Cu2+} : n_{PVP} = 35:1 for sample P-PVP2) improved the sample uniformity (**Fig. 2.3B**). The sample was composed of tapered nanoplates with approximate dimensions of 100 nm in width, 600 nm in length, and 25 nm in thickness. Brochantite powders synthesized using microwave assisted hydrothermal reaction (sample HT) are shown in **Figure 2.3C**. These powders had a nanoplate morphology with an average length of 430 nm and thickness of about 40 nm. Compared to the samples prepared with PVP, the nanostructures in sample HT were thicker and did not have such tapered ends. The plate-like structures observed in samples P-PVP1 and P-PVP2 can be explained by the presence of PVP adsorbing onto certain crystallographic planes of brochantite to affect the crystal growth kinetics. The mechanism of shape control with PVP may be due to Cu^{2+} coordination to the polar oxygen or nitrogen groups of the PVP mers[81] or interaction with the hydroxyl groups[82] on the

terminal end of the PVP chains, as has been seen in other nanoparticle systems. The anisotropic particle morphology observed in the hydrothermal synthesis without requiring PVP or other structure directing agent indicates a preferred crystallographic growth direction.

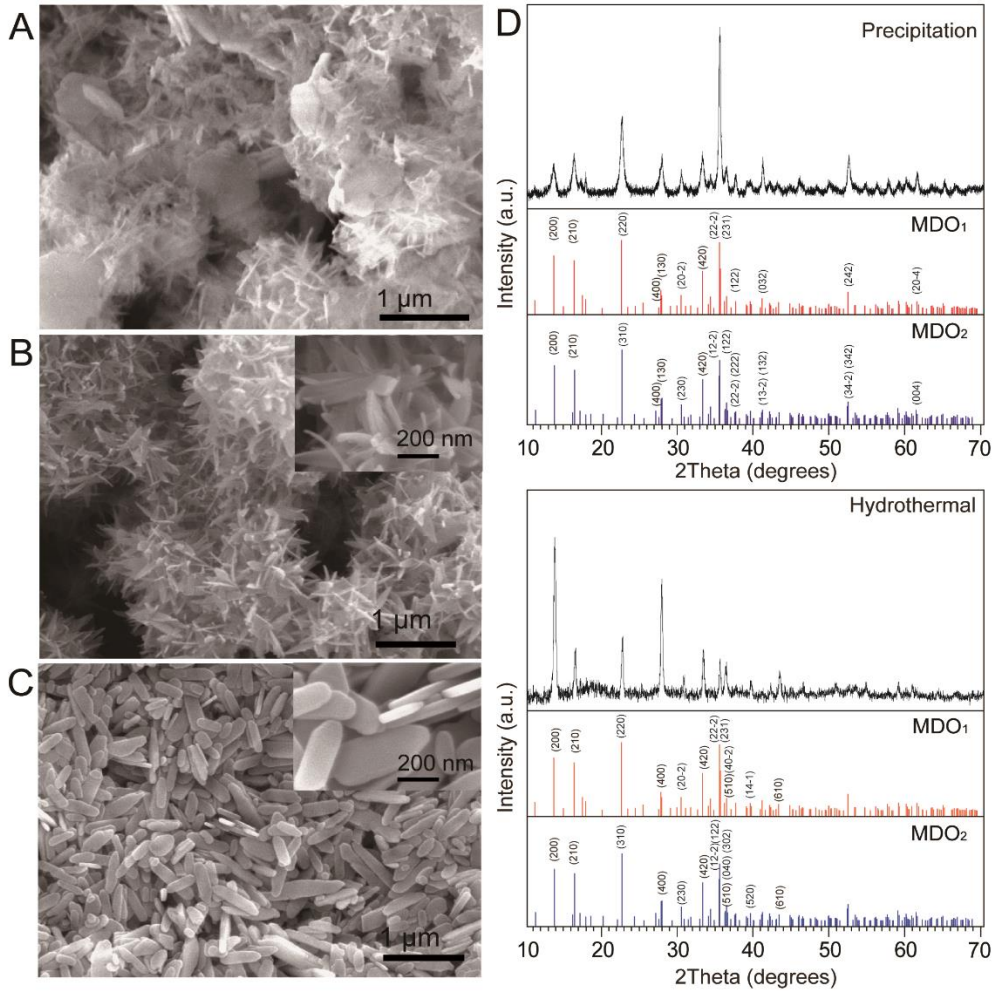

Figure 2. 3 (A)-(B) SEM images of brochantite made by precipitation with PVP (A) P-PVP1 (n_{Cu2+} : n_{PVP} = 70:1, (B) P-PVP2 (n_{Cu2+} : n_{PVP} = 35:1); (C) Brochantite nanoplates prepared using hydrothermal synthesis (HT). (D) XRD comparing brochantite prepared

using precipitation and hydrothermal synthesis compared to the two polytypes of brochantite. Only major reflections were labeled for clarity.

Brochantite is classified as a sheet-type sulfate mineral, with corner-linked and edge-linked chains consisting of distorted $Cu(OH)_4O_2$ and $Cu(OH)_5O$ octahedra that are connected with SO_4 tetrahedra to form corrugated layers parallel to the (100) plane[66,83]. Brochantite minerals typically display cleavage on the {100} planes due to the weak apical Cu-O bonds and H-bonds that form between these layers (**Fig. 2.1**). Planes propagating in the a-direction of brochantite require sulfate ions, while those propagating in the b- and c-directions require hydroxide ions in order to grow the double Cu polyhedra chains. The production and addition rates of these two anions compete and determine the shape of the crystal. Previous studies showed that anisotropic brochantite structures such as plates and needles can be synthesized using ultrasonication[80], but here we show that use of PVP as a structure directing agent or microwave assisted hydrothermal reaction can result in much smaller nanostructures with high surface area for Li^+ insertion into the interlayer space. Brochantite is considered an order-disorder (OD) material[68], in which different ways of stacking neighboring layers allows for disordered and ordered polytypes to exist.

Figure 2.3D shows the XRD pattern for sample P, which was prepared using precipitation, and sample HT prepared by microwave-hydrothermal reaction. The precipitated samples prepared with PVP showed identical XRD patterns to sample P.

Reference patterns for the MDO_1 and MDO_2 polytypes of brochantite are shown for comparison[68]. Both polytypes are monoclinic and have very similar structures. MDO_1 adopts the $P12_1/a1$ space group and has lattice constants of a = 13.140 Å, b = 9.863 Å, c = 6.024 Å, and $\beta = 103.16^o$. MDO_2 adopts the $P2_1/n11$ space group and has lattice parameters of a = 12.776 Å, b = 9.869 Å, c = 6.026 Å, $\alpha = 90.15^o$. The XRD pattern for sample P showed reflections that matched both polytypes, which may explain the broadness of some of the peaks. No characteristic diffraction peaks from other phases or impurities were detected. The XRD pattern of sample HT showed sharper and narrower peaks, with enhanced intensity for the (200) and (400) reflections compared to both reference patterns and also the samples prepared with precipitation. Compared to sample P, there were also fewer reflections, while the peaks that were present are common to both polytypes. The absence of reflections in addition to those expected based on the space group (i.e., non-space group absences) has been observed in brochantite and is a characteristics of its OD properties[68]. These results suggest that the microwave-hydrothermal synthesis may favor formation of brochantite with a different atomic connectivity than precipitation methods. The strong (200) and (400) reflections in sample HT indicate a preferred orientation and suggest that the layer-stacking direction, or a-axis, is along the thickness direction of the nanoplates, which tend to lay flat on the substrate (**Fig. 2.3C**).

To better understand the structure of the sample HT nanoplates, TEM characterization was performed (**Fig. 2.4**). Selected-area electron diffraction (SAED) of an individual brochantite nanoplate (Fig. 3A-B) showed d-spacings consistent with a [100] zone axis for the MDO_1 polytype, with the nanoplate long-axis (growth direction) in the [020] and a-axis along the layer-stacking direction, consistent with the XRD results. However, we cannot rule out that there might also be nanoplates with the MDO_2 structure. The nanoplates were beam-sensitive and could easily decompose under electron beam irradiation, making careful observation by TEM difficult. As soon as the electron beam hit the sample, pores started to appear within the nanoplates (**Fig. 2.4C**) and became larger over time (**Fig. 2.4D**) due to beam damage. The speed of this deterioration was dependent on the intensity of illumination. Some wave-like fringes swept across the particles, indicating that the internal structure was being altered by the beam. This was evident by another observation in which an amorphization process could clearly be seen. Initially the particles were crystalline, but after prolonged exposure to the incident beam, the lattice fringes of the outermost layer disappeared, enveloping the nanoplate with an amorphous shell (**Fig. 2.4E**). The shell grew inwards and the amorphous-crystalline interface advanced towards the core of the nanoplate until it turned completely amorphous. This process was also observed in the electron diffraction pattern, in which the diffraction spots gradually faded away with longer irradiation times. Thermal analysis of brochantite has suggested that it can decompose

following equation (1) between 325-500 ^{o}C, followed by a second decomposition step at 650-780 ^{o}C following equation (2)[84].

$$Cu_4(OH)_6SO_4 \rightarrow Cu_2OSO_4 + 2CuO + 3H_2O \quad (1)$$

$$Cu_2OSO_4 \rightarrow 2CuO + SO_3 \quad (2)$$

The removal of H_2O and SO_3 from the structure during these decomposition reactions can explain the formation of the pores in the brochantite upon heating from the electron beam. Based on these equations, the resulting material is likely amorphous CuO.

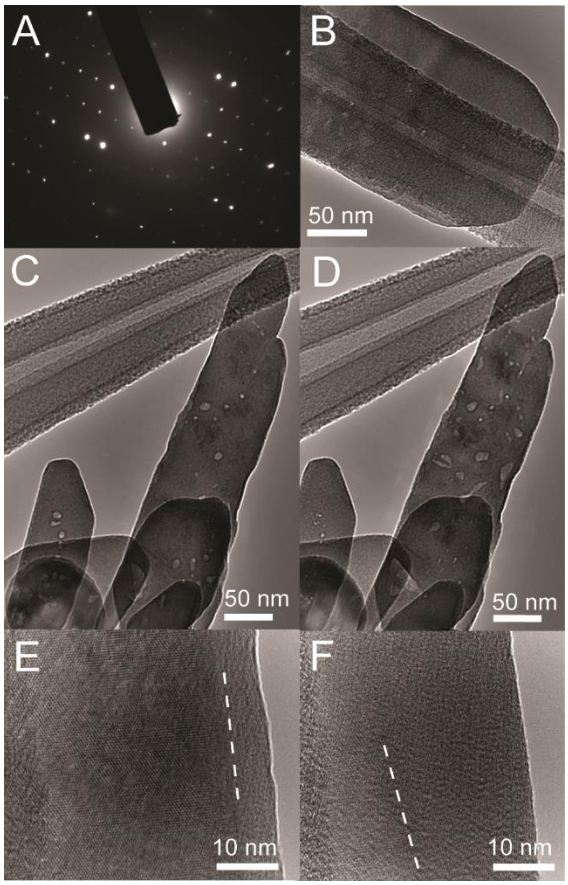

Figure 2. 4 TEM of HT brochantite nanoplates. (A) Selected-area electron diffraction pattern of nanoplate in (B). (C) Low-magnification TEM images of nanoplates showing

decomposition under exposure to electron beam, (D) same nanoplates in (C) after 1 min longer exposure. (E) High-magnification image of nanoplate showing amorphous surface region. The dashed line shows the amorphous-crystalline interface. (F) After 1 min longer exposure, the amorphous shell became thicker and the amorphous-crystalline interface moved towards the core of the particle.

2.3.2 Electrochemical Characterization

2.3.2.1 Brochantite made by Different Methods

To evaluate the electrochemical properties of the brochantite samples prepared using the various synthesis methods, potentiodynamic cycling was performed on composite electrodes made from brochantite, carbon black conducting additive, and polyvinylidene difluoride binder. The voltage profiles for the first discharge (lithiation) and charge (delithiation) cycles for the different samples and the corresponding differential plots are shown in **Figure 2.5 A**.

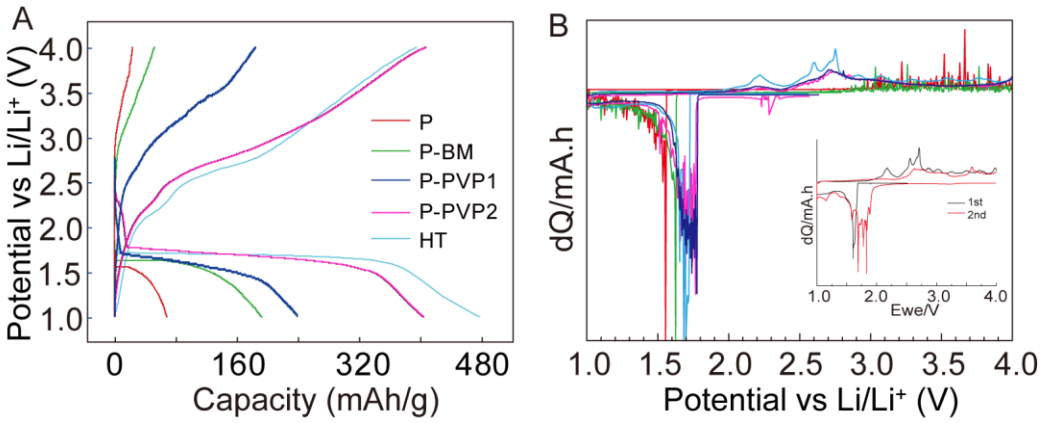

Figure 2. 5 (A) Voltage profiles of first discharge and charge and (B) differential charge plot for half-cells prepared with brochantite made by different methods. The inserted is the differential charge plot for first 2 cycles for HT brochantite.

The brochantite particles prepared by precipitation (sample P) displayed about 68 mAh/g of discharge capacity and 23 mAh/g of charge capacity, resulting in a Coulombic efficiency (CE) of 34%. After ball-milling the samples for 10 minutes (sample P-BM), the discharge capacity was increased to 191 mAh/g while the CE was about the same (27%), which indicated that decreasing the particle size can help the electrochemical reactivity due to the poor conductivity of the brochantite active material. The precipitated samples prepared with PVP showed even higher capacities and CE, with a discharge capacity of 238 mAh/g for P-PVP1 and 408 mAh/g for P-PVP2. The CE were 78% and 89%, respectively. This indicates that the nanoscale particle sizes can greatly improve the electrochemical performance by decreasing the electron and Li^+ transport distances.

The sample HT nanoplates showed the highest discharge capacity of 478 mAh/g, which is slightly higher than the theoretical capacity of 474 mAh/g corresponding to insertion of 8 Li^+ and electrons per brochantite formula unit, i.e. the 2 electron reduction of Cu^{2+}. It supports the conversion reaction mechanism. The charge capacity of 398 mAh/g corresponds to extraction of 1.68 Li^+/Cu. Furthermore, the discharge potentials of the nanostructured brochantite were slightly higher than that for bulk brochantite, which can be seen in **Figure 2.5B**. The discharge potential increased from 1.55 V vs. Li/Li^+ in sample P to 1.6-1.8 V in the PVP samples and 1.7 V for sample HT. The increase in discharge potential can be explained by a lower internal resistance in the nanostructured samples, since the electron transport distances are small and there is more contact area between the brochantite and the conducting carbon black in the composite. The values of the discharge potentials can be explained by the induction effect[63]. For instance, the discharge voltage of brochantite is higher than that for CuO (1.35 V)[60,62] and Cu_2O (1.5 V)[36] but lower than that for $CuSO_4 \cdot 5H_2O$ (3.2 V)[46]. The discharge voltage for brochantite is slightly higher than that for copper oxides due to the presence of the more ionic sulfate and hydroxyl groups, but its lower number of sulfate anions gives it a lower voltage than for copper sulfate. The plateaus in the discharge profiles suggest a two-phase reaction mechanism, whereby growth of a new phase occurred at the expense of the initial phase, and not a single-phase reaction (i.e. lithiation in the form of solid solution). Also, as the brochantite particle size

decreased, the discharge profiles became flatter, which is similar to what has been observed for particle size reduction in $CuSO_4 \cdot 5H_2O$[46] and CuO conversion electrodes[62], indicating improved kinetics. At higher depths of discharge, the voltage followed a sloped profile from 1.5-1 V. This is similar to the sloped profile observed in Cu_2O, which has been attributed to formation of Li_2O and Cu^0 [36].

In contrast, all of the charging profiles showed sloped features. Inspection of the differential charge plots for the nanostructured brochantite (**Fig. 2.5B insert**) suggests there could be major phase changes at 2.18 and 2.71 V vs. Li/Li^+ due to the presence of larger peaks at those potentials, there were also numerous small peaks from 2.71 to 4 V vs. Li/Li^+, suggesting other smaller phase transitions at these higher charging potentials. The electrochemical data are more complicated for the charging of brochantite compared to other similar compounds. Due to the mixed anion nature of brochantite, the electrochemical mechanism for its reaction with lithium may be a combination of reactions similar to those seen in CuO, $LiCuO_2$, or $CuSO_4$. This may explain the presence of so many peaks in the differential charge plots. Delithiation occurs as a two-phase reaction at 3.5 V in anhydrous $CuSO_4$ and at 3.65 V for $CuSO_4.5H_2O$, with well-defined plateaus at those potentials in the voltage curves[46]. In contrast, the sloped charging profile for brochantite might be more similar to processes in the copper oxides. The initial charging process seen as the sloped region in the voltage profile from 1-2 V is similar to that found when charging Li_2O/CuO

composites after full lithiation[85] and has been attributed to the oxidation of Cu^0 to Cu^+. The formation of multiple peaks during charging at higher potentials is similar to the delithiation of $LiCuO_2$, which is characterized by 4 small peaks between 3 – 3.6 V[86]. The nanoscale size of the brochantite particles may also lead to other phases and reactions not observed in the bulk counterparts, such as small structural changes or solid solution formation over small potential regions.

2.3.2.2 Brochantite made by Microwave-assisted Hydrothermal method

To better understand the structural changes upon cycling that occur in brochantite, the nanoplates (sample HT) were used for further electrochemical studies as well as *ex situ* SEM, XRD, and XPS investigation. The first 5 cycles of the brochantite nanoplates using galvanostatic cycling with a C/20 rate are shown in **Figure 2.6A**. The potential decreased then increased slightly in the first discharge (**Fig. 2.6A, inset**). This feature has been attributed to nucleation and growth of new phases and is frequently seen in materials that undergo conversion reactions[60]. **Figure 2.6C** shows the capacity as a function of cycle number and CE for each cycle. The capacities were observed to decrease quite rapidly, with less than 150 mAh/g capacity remaining at the 10^{th} cycle. The differential charge plot of the second cycle (**Fig. 2.5B insert**), shows that lithiation occurs at higher potentials in the 2^{nd} cycle, suggesting a structural change in the first discharge that is not reversible. Galvanostatic cycling at different C-rates (**Fig. 2.6B**) showed that the brochantite could maintain a high first cycle capacity until 1C, at which the observed capacity was about 50% lower.

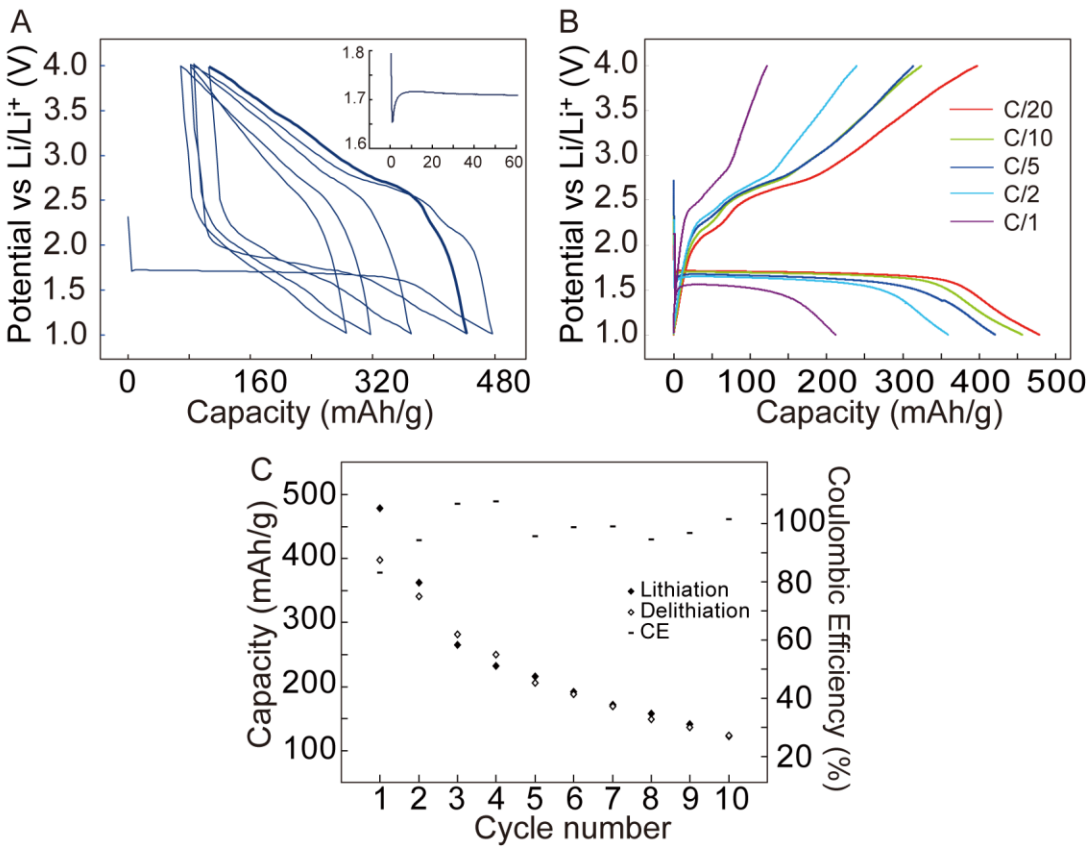

Figure 2. 6 (A) Cycling of HT brochantite using C/20 rate. The inset shows a zoomed in region in the first discharge. (B) First discharge and charge of HT at different C-rates. (C) Capacity and Coulombic efficiency for cycling of HT brochantite.

2.3.3 Structural Characterization during Electrochemical Reaction

To better understand the origin of the poor capacity retention, SEM, XRD, and XPS studies were performed on the unlithiated (as made), lithiated, and delithiated brochantite films.

2.3.3.1 Scanning Electron Microscopy

The brochantite nanoplates were well dispersed with the carbon black (**Fig. 2.7A**) in the prepared electrodes and were observed to maintain their morphology after lithiation to 447 mAh/g (**Fig. 2.7B**). No obvious signs of Cu metal dendrite extrusion were observed.

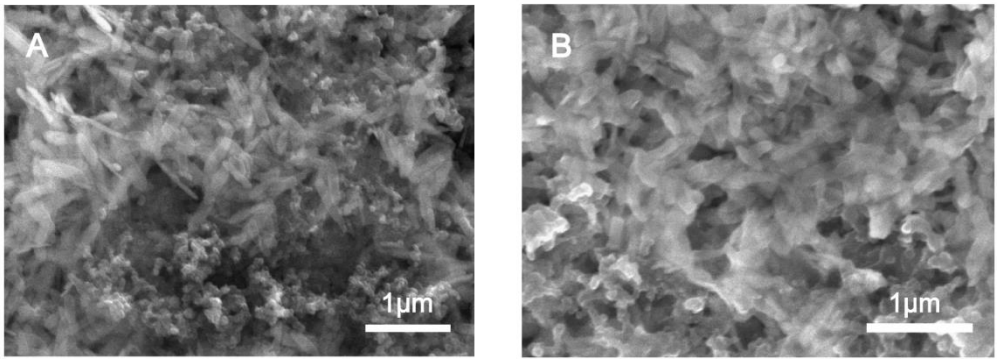

Figure 2. 7 (A) SEM of HT brochantite film before and (B) after lithiation.

2.3.3.2 X-ray Diffraction

XRD of the as-prepared film only showed peaks from the Al foil current collector and the brochantite (**Fig. 2.8**). After lithiation to a capacity of 447 mAh/g, the XRD pattern showed very weak reflections from the brochantite, suggesting the structure became amorphous after discharge. This also supports the conversion reaction mechanism, despite the feasibility of topotactic Li^+ insertion based on the occupiable volume calculations. No obvious peaks from Cu metal, Li_2SO_4 or other Li salts were observed. It is possible that the dispersed nature and small size of these phases make XRD observation difficult unless using high resolution XRD at a synchrotron source, which has been used for investigating discharge products in other Cu containing conversion materials[60]. Although the presence

of metallic Cu was not observed in the XRD patterns of discharged brochantite, the full reduction of Cu^{2+} to Cu^{0} is expected based on the high capacities observed. Without more structural characterization, it is difficult to determine what the other discharge products could be. Based on the formula of brochantite, LiOH, Li_2O, and Li_2SO_4 are all reasonable compounds, and they likely form an amorphous matrix.

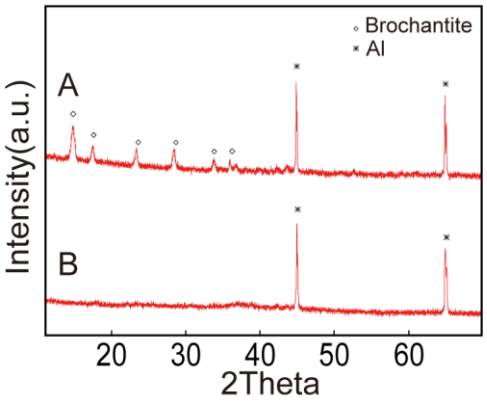

Figure 2. 8 XRD pattern of (A) as-made film, and (B) after lithiation.

2.3.3.3 X-ray Photoelectron Spectroscopy

In order to better characterize the oxidation state of the Cu in brochantite during electrochemical reaction, XPS measurements were performed. The instability of LiOH under X-ray irradiation under high vacuum[87] made it difficult to use XPS to better characterize the matrix products. **Figure 2.9** shows the high resolution scans from the Cu 2p region from different samples to identify the chemical states of the brochantite. **Figure 2.9A** shows the XPS spectrum for the sample HT brochantite powder as a reference. Peaks

associated with the Cu $2p_{3/2}$ and Cu $2p_{1/2}$ shells were observed along with shake-up satellite bands at higher binding energies to each of the peaks (centered at 942.3 eV for Cu $2p_{3/2}$ and 962.3 eV for Cu $2p_{1/2}$). These satellite peaks are characteristic of Cu^{2+} compounds and arise due to charge transfer transitions from the bound ligands into the unfilled d^9 valence level of Cu^{2+} [88]. The broader Cu 2p peaks in Cu^{2+} containing compounds compared to Cu^{+} and Cu^{0} compounds is due to the coupling between unpaired electrons in the paramagnetic Cu^{2+}. The peaks were deconvoluted and could each be fitted to two peaks as noted by the black dotted lines (approximately 935.2 eV and 933.2 eV for Cu $2p_{3/2}$, 955.1 eV and 953.0 eV for Cu $2p_{1/2}$). Because of the two types of Cu-O bonds in brochantite (i.e., Cu-O-Cu and Cu-O-SO_3), the Cu 2p peaks represent a combination of $CuSO_4$ (936.0 eV) and CuO (933.1 eV) type contributions[89], which can also contribute to the broadness of the peaks. The XPS spectrum of the HT brochantite nanoplates is in close agreement to that obtained for naturally occurring brochantite mineral[89].

In **Figure 2.9B**, the XPS spectrum for the HT brochantite electrode (with carbon black and PVDF) prior to electrochemical cycling is shown. Deconvolution of the Cu $2p_{3/2}$ peaks indicated an increase in peak area for the higher binding energy chemical environment compared to the brochantite powder. Because the XRD pattern of the electrodes showed the brochantite structure did not change after film preparation, this small difference may reflect interactions between the Cu and the fluorides in PVDF.

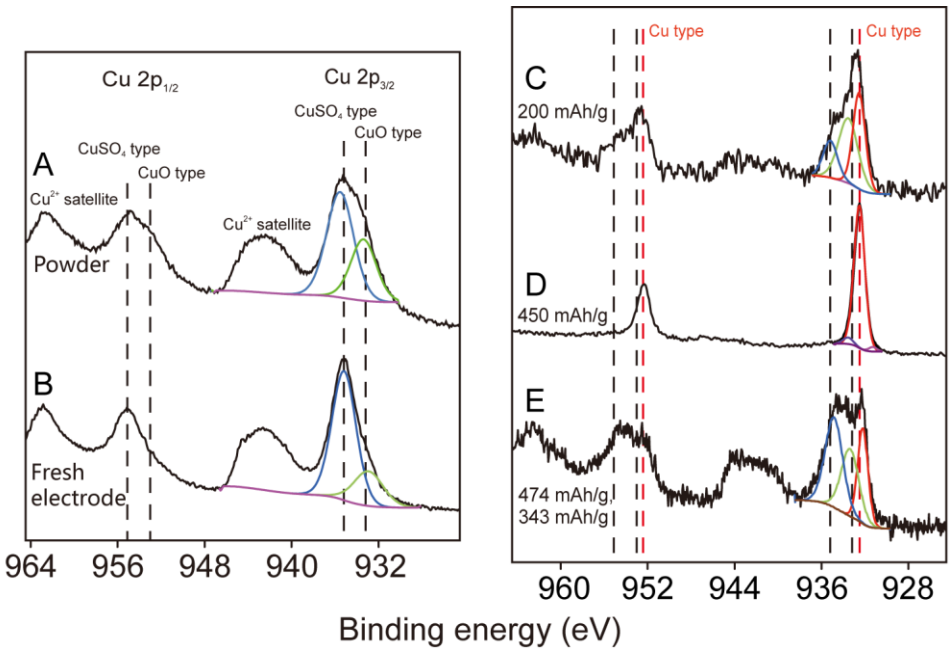

Figure 2. 9 XPS on HT brochanite (A) powder, (B) untested film, (C) after lithiation to 200 mAh/g, (D) after lithiation to 447 mAh/g, (E) after lithiation to 474 mAh/g followed by delithiation (charge capacity of 343 mAh/g).

After the film was lithiated to a capacity of about 200 mAh/g (corresponding to insertion of 0.85 Li^+/Cu), shoulders appeared at lower binding energies at 932.5 eV for Cu $2p_{3/2}$ and 952.4 eV for Cu $2p_{1/2}$, as noted by the red dotted lines (**Fig. 2.9C**). The intensity of the shake-up bands also decreased significantly. Both of these observations indicate the presence of lower valence species such as Cu^+ or Cu^0. Because the binding energies and peak widths for Cu^+ and Cu^0 are very similar (932.3 eV for Cu and 932.4 eV for Cu_2O), it is difficult to identify which oxidation state is present[90,91]. Deconvolution of the Cu $2p_{3/2}$ peak (**Fig. 2.9C**) showed a much lower $CuSO_4$-type contribution to the chemical

environment compared to CuO. The peak attributed to Cu^{+} or Cu^{0} had the highest intensity of the three contributions.

Lithiation of a film to a capacity of 447 mAh/g (1.89 Li^{+} inserted/Cu) resulted in a spectrum as shown in **Figure 2.9D**, where the satellite bands completely disappeared and only the Cu 2p peaks associated with Cu^{+} or Cu^{0} remained. Deconvolution of the $Cu2p_{3/2}$ peak showed contributions from three peaks at 931.3 eV, 932.5 eV and 933.5 eV (**Fig. 2.9D**). Since the discharge capacity for the film was 94.3% of the theoretical capacity for brochantite, it is likely that most of the copper is in the form of Cu^{0}. Hence, the large peak at 932.5 eV is assigned to Cu^{0}. Because of the disappearance of the satellite peaks, the small peak at 933.5 eV may be due to Cu^{+}, while the peak at the lowest binding energy may be due to Cu interactions with Li. Since these XPS results suggest that the Cu in the fully discharged brochantite is completely reduced, but no Cu^{0} reflections were observed in the XRD after lithiation (**Fig. 2.9D**), this suggests that the Cu must be in the form of very small nanoparticles. Unfortunately, the extreme beam sensitivity of the lithiated brochantite made it difficult for visualization of these particles using TEM.

Figure 2.9E shows the XPS spectrum of a brochantite film after one lithiation/delithiation cycle. The presence of Cu^{2+} after charging is apparent due to the large peak at 934.9 eV, which is associated with Cu bonding to sulfate. Other XPS studies on lithiation of CuO[92] and $Cu_3B_2O_6$[47] did not observe recovery of Cu^{2+} after charging. In the

case of $Cu_3B_2O_6$, improving the electronic conductivity by adding 65 wt% of carbon in the electrode was effective in improving reversibility and resulted in recovery of the Cu^{2+} peaks after charging[47]. Since the Cu^{2+} peaks were observed in our electrodes with only 20 wt% carbon, this suggests that the nanostructured morphology facilitated good reversibility in the conversion reaction, even for a poorly conducting material like brochantite. The discharge capacity observed in this sample was 474 mAh/g and charge capacity was 343 mAh/g, indicating the electrode was almost fully lithiated but during charging the copper was not fully re-oxidized to Cu^{2+}. The XPS spectrum is consistent with these results since the peak from Cu^0 (or Cu^+) is still present.

2.3.3.4 Energy Dispersive Spectrometer

Given that the XPS results indicate that the conversion reaction does have some reversibility due to the presence of Cu^{2+} after the electrode was fully lithiated and then charged, the poor capacity retention observed in the brochantite electrodes is likely due to some other reason. Upon disassembly of a cell that was cycled 20 times, the Li metal counter electrode was observed to have some brown coloration. **Figure 2.10** shows the SEM micrograph and energy dispersive x-ray spectroscopy (EDS) analysis of the Li metal once removed from the cell. Under backscattered electron imaging mode, a phase clearly distinctive from the background can be observed. EDS analysis of this region confirmed this phase to be copper metal. Therefore, we believe that the poor capacity retention upon

extended cycling of the brochantite nanoplates is due to copper dissolution into the electrolyte and re-deposition on the Li counter electrode. This would result in fewer Cu atoms available in the electrode to participate in the electrochemical reaction and coating of the Li electrode, both of which would affect the cycling performance. The oxidation of Cu^0 to Cu^+ species that dissolve in the electrolyte has been observed in other Cu-containing conversion materials[46,93].

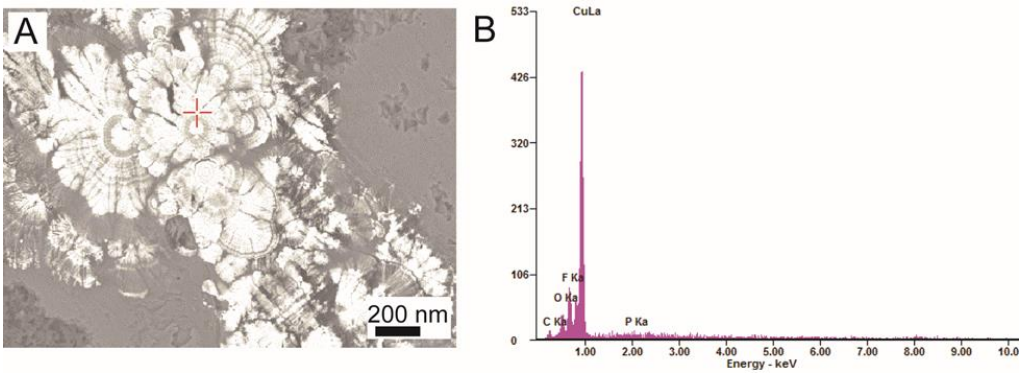

Figure 2. 10 SEM and EDS of Cu metal deposition on Li counter electrode after cycling.

2.4 Conclusion

In conclusion, we found that brochantite can undergo an electrochemical reaction with lithium, with nanostructured morphologies demonstrating the theoretical discharge capacity based on the 2 electron reduction of Cu^{2+}. Despite occupiable volume calculations that show topotactic Li^+ insertion into brochantite might be feasible, we found that

brochantite with nanoplate structure underwent a conversion reaction based on XPS results showing formation of Cu^0 after lithiation. XRD characterization suggested that the discharge products consist of Cu nanoparticles too small to be detected by X-rays within an amorphous matrix. High Coulombic efficiencies indicate that the conversion reaction in brochantite nanoplates has high reversibility, unlike other Cu conversion materials such as CuF_2. However, poor capacity retention was observed due to Cu dissolution from brochantite during charging. The results indicate that copper hydroxysulfate materials such as brochantite may be promising electrode materials for lithium-ion batteries if this dissolution problem is addressed. Further work on similar materials containing different transition metals may lead to other promising targets with improved cycling performance and higher discharge potentials.

3: JAROSITE AS CATHODE ELECTRODES FOR LITHIUM-ION BATTERY

3.1 Introduction

Recently, there has been a great deal of interest in polyanion [$(XO_n)^{m-}$] materials for Li-ion battery electrodes due to their low cost, good stability, and safety. Materials with sulfate and phosphate anions have been known to form a wide range of structural arrangements. For example, naturally occurring metal copper hydroxysulfate minerals of the form $M_x(OH)_y(SO_4)_n$ are found in a variety of expanded framework, tunnel, and layered structures[66]. Such structures may provide pathways for effective Li^+ diffusion and the presence of mixed anions may be used to tune the redox potential of the metal and create different environments for Li^+ insertion. In our previous work[94], we reported the electrochemical study of the mixed anion material $Cu_4(OH)_6SO_4$, also known as the mineral brochantite. We found that microwave hydrothermal synthesis was effective for obtaining nanostructured brochantite with a nanoplate morphology using short reaction times. The brochantite materials underwent a conversion reaction upon reaction with lithium, but capacity retention was limited due to Cu dissolution from brochantite during charging.

To expand this work, we have chosen to study the morphology and electrochemical properties of materials in the jarosite family of compounds prepared using microwave

hydrothermal reaction. Jarosite, which has a chemical formula of $KFe_3(OH)_6(SO_4)_2$, is a widespread mineral on Earth[95–97] and is found in the oxidized zones of sulfide ore deposits, acid sulfate soils, hydrometallurgical and bioleaching systems, and fluvial environments contaminated by acid mine drainage[95,98,99]. It was also identified via Mössbauer spectroscopy at the Eagle crater landing site of the Mars Opportunity rover[100,101], which is mineralogical evidence for aqueous processes on Mars, probably under acid-sulfate conditions[102]. The precipitation of jarosite-type compounds is commonly used in the metallurgical industry to eliminate dissolved ions and is especially effective for removing certain trivalent ions such as Al^{3+}, Cr^{3+}, In^{3+}, and Ga^{3+}, which substitute Fe^{3+} in the jarosite structure[103]. Jarosites have also attracted considerable attention as prominent models of a Kagomé Heisenberg-type antiferromagnet because of their unusual magnetic property of spin frustration[104].

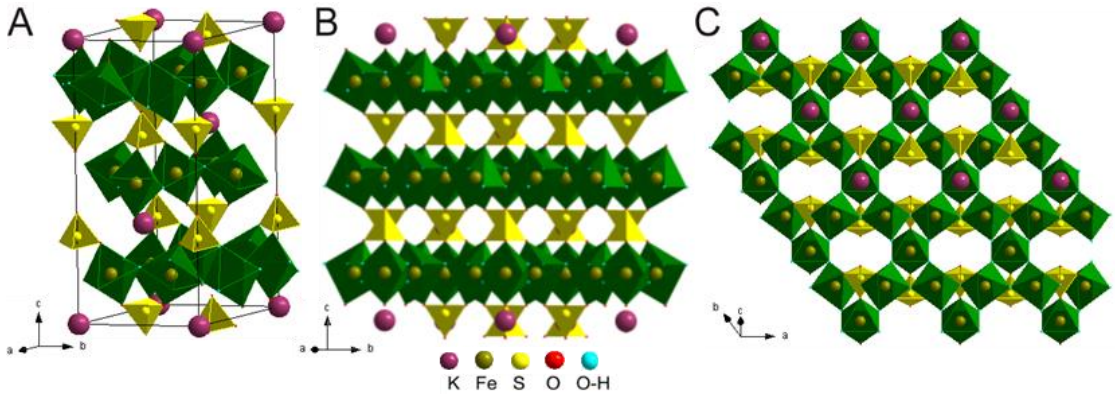

Figure 3. 1 (A) Polyhedron representation of jarosite $KFe_3(SO_4)_2(OH)_6$ unit cell; (B) layered structure when viewing along the [210] direction; (C) vacant channels when

viewing along the [-1-21] direction. The hydroxyl group is represented as one unit in turquoise.

Recently, jarosite compounds have been investigated as electrodes for Li-ion batteries due to their interesting structure[105–108]. The jarosite family belongs to the rhombohedral space group $R\bar{3}m$ and has a general chemical formula of $AM_3(SO_4)_2(OH)_6$ where A is typically a monovalent ion such as K^+, Na^+, Ag^+, NH_4^+ and H_3O^+, and M is a trivalent cation **(Fig. 3.1A)**[109]. The trivalent ions adopt a slightly distorted octahedral geometry in the jarosite framework[110] and these octahedral layers are well separated by layers of sulfate, hydroxide, and A cations along the *c*-axis (**Fig. 3.1B**). Jarosite can also be classified as a layered mineral with Kagomé layers[110]. The triangular subunit of the Kagomé lattice is composed of a sulfate anion, which caps three vanadium-oxygen octahedra that form a layered corner-sharing triangular network, and this basic building block is not perturbed by the alkali ion[102]. Jarosites can be considered tunnel structures as well, since channels containing the A cations can be observed along the [-1-21] direction (**Fig. 3.1C**). The open channel structure may allow for effective Li^+ diffusion when using jarosite materials as electrodes in Li-ion batteries.

So far, most of the investigations have focused on the electrochemical properties of $KFe_3(OH)_6(SO_4)_2$, which demonstrated reversible capacities of 117 mAh/g at 0.2 C when used as an insertion-type cathode (cycling between 1.6 – 4.0 V vs. Li/Li^+)[106], and capacities >

1300 mAh/g when used as a conversion-type anode (cycling between 0.005 – 3 V vs. Li/Li^+)[108] when prepared in a 2D nanosheet morphology. These studies demonstrate the potential that jarosite-based electrodes have as high performance electrodes for Li-ion batteries. However, a systematic study of the effect of composition (i.e. the choice of A, M^{3+}, and also presence of intercalated H_3O^+ or H_2O molecules) on the electrochemical properties has yet to be performed. As the jarosite structure can accommodate many different ions, it may be also a good starting point for developing cathodes for the storage of larger cations, such as Na^+.

Here we report the synthesis of several jarosite compounds using microwave-assisted hydrothermal methods for the first time, in order to control the particle size and shorten the reaction time compared to conventional hydrothermal reaction. Besides $NaFe_3(SO_4)_2(OH)_6$ (Na,Fe-jarosite) and $KFe_3(SO_4)_2(OH)_6$ (K,Fe-jarosite), we also investigated the V^{3+} analogues $NaV_3(SO_4)_2(OH)_6$ (Na,V-jarosite) and $KV_3(SO_4)_2(OH)_6$ (K,V-jarosite) to further study the effects of the trivalent and alkali metals on the observed electrochemical properties for Li^+ insertion. To our knowledge, this is the first time the electrochemical properties of the vanadium jarosites have been studied. Na,Fe-jarosite was also evaluated in half-cells with Na metal counter electrodes to determine if electrochemical desodiation/sodiation could be possible. Ex-situ X-ray diffraction (XRD) and scanning electron microscopy (SEM) were performed in order to characterize the structure and

identify changes occurring during the electrochemical reactions. The fundamental science gained from this study will add to the existing knowledge base related to iron and vanadium-based electrodes for lithium-ion batteries and can be applied to obtain better understanding of the electrochemical properties other mixed anion materials.

3.2 Experimental Methods

3.2.1 Synthesis of Jarosite

Jarosite particles were prepared in a microwave hydrothermal reactor (CEM Discover SP) using CEM 35 mL quartz vessels containing Teflon PFA liners, with vigorous magnetic stirring during the reaction. Iron (III) chloride, vanadium (III) chloride, potassium sulfate, sodium sulfate, and sulfuric acid were obtained from Sigma-Aldrich and used as received. After the reaction, the precipitates were separated using vacuum filtration and dried at 100 ^{o}C. Afterwards, the powder was collected, washed with ethanol and water several times and dried at 60 ^{o}C overnight.

3.2.1.1 $NaFe_3(SO_4)_2(OH)_6$

A mixture was prepared containing 5 mL of a 0.3 M $FeCl_3$ solution and 5 mL of a 0.6 M Na_2SO_4 solution. The pH of the mixture was adjusted to 1.6 by adding H_2SO_4 and then transferred to the reaction vessel. The suspension was heated to 100 °C within 10 min in the microwave reactor and held for 10 min. The obtained precipitate was yellow in color.

3.2.1.2 $KFe_3(SO_4)_2(OH)_6$

Identical procedures were performed as for Na,Fe-jarosite except the precursor consisted of 5 mL of 0.6 M K_2SO_4 added to 5 mL of 0.3 M $FeCl_3$ solution. The obtained precipitate was yellow in color.

3.2.1.3 $NaV_3(SO_4)_2(OH)_6$

The precursor mixture contained 5 mL of a 0.3 M VCl_3 solution and 5 mL of a 0.6 M Na_2SO_4 solution, which was heated to 150 ℃ within 10 min and held for 5 min. The obtained precipitate was brown in color.

3.2.1.4 $KV_3(SO_4)_2(OH)_6$

Identical procedures were performed as for Na,V-jarosite except the precursor consisted of 5 mL of 0.6 M K_2SO_4 added to 5 mL of 0.3 M VCl_3 solution. The obtained precipitate was brown in color.

3.2.2 Materials Characterization

3.2.2.1 X-ray Diffraction

XRD was used to perform structural characterization on the prepared jarosite powders. XRD data was collected using a Panalytical X'pert Pro with CuKα radiation operated at 40 kV/40 mA. Electrodes characterized after electrochemical tests were rinsed several times with ethanol and dried at 60 ^oC overnight prior to XRD measurements. Rietveld refinement was performed using HighScore Plus. Reference XRD patterns were obtained from the International Centre for Diffraction Data (ICDD) database or calculated from CIF files using Diamond 3.2. The following reference patterns were used: $NaFe_3(SO_4)_2(OH)_6$ (PDF 00-036-0425), $K_{0.81}(H_3O)_{0.19}Fe_{2.88}(OH_2)_{0.36}(OH)_{5.64}(SO_4)_2$ (pattern calculated in Diamond

using the structure from ref.[111] and referred to as $(K,H_3O)Fe_3(SO_4)_2(OH)_6$ for convenience), $KFe_3(SO_4)_2(OH)_6$ (PDF 01-076-0629), $NaV_3(SO_4)_2(OH)_6$ (pattern calculated in Diamond using the structure from ref.[112]), and $KV_3(SO_4)_2(OH)_6$ (PDF 00-056-0863).

3.2.2.2 Scanning Electron Microscopy

SEM studies were performed using a XL 30 ESEM-FEG. Powder samples were dispersed into ethanol with ultrasonication for 5 minutes and then dropped onto a Si wafer for SEM imaging. To mitigate charging, the jarosite samples were sputter coated with a thin layer of Au prior to SEM observation.

3.2.3 Electrochemical Measurement

Jarosite composite electrodes were prepared by mixing the jarosite active material with polyvinylidene difluoride (PVDF) binder (Kynar) and SuperP Li carbon black (TimCal) with a ratio of 80:10:10 by weight. N-methyl-2-pyrrolidone was added dropwise and the slurry was then stirred overnight to form a homogenous free-flowing paste. This slurry was then coated onto a piece of Al foil using an automated film coater equipped with a Meyer rod and dried in an oven at 120 ^oC for 3 h. The foil was then punched into disks and weighed prior to electrochemical testing.

Pouch cells were assembled in an argon-filed glove box using lithium metal foil as the counter electrode, Celgard 2500 as separator, and 1 M $LiPF_6$ (EC:DMC:DEC, 4:2:4 in volume, LBC 3051C, MTI) as electrolyte. Galvanostatic or potentiodynamic measurements were performed on a BioLogic VMP3. For galvanostatic measurements, C-

rates were determined using a theoretical capacity of 160.54 mAh/g according to the 1 electron reduction for each of the 3 Fe (insertion of 3 Li^+) per $KFe_3(OH)_6(SO_4)_2$ formula unit. The current density corresponding to a C/20 rate is 8 mA/g. As the theoretical capacities of the four types of jarosite were all around 160 -170 mAh/g, 8 mA/g was used as the current density for the galvanostatic measurements of all four jarosites. For potentiodynamic measurements, a 5 mV voltage step was used with a threshold current density of 8 mA/g of jarosite.

The Na,V-jarosite was also evaluated in Na-half cells using Na metal as the anode, Celgard 2500 as separator, and 1 M $NaClO_4$ in propylene carbonate (PC) as electrolyte. Galvanostatic measurements were performed on a BioLogic VMP3 between 1 – 4 V vs. Na/Na^+ and current density of 8 mA/g.

3.3 Results and Discussion

3.3.1 Structural Characterization of Synthesized Jarosites

Synthetic jarosite is typically prepared using precipitation in acid solutions[104,113,114]. The iron jarosites can be prepared by adding ferric ion into acidic sulfate solutions as shown in Equation (1)[102]:

$$3M^{3+} + A^+ + 2SO_4^{2-} + 6H_2O \rightarrow AM_3(SO_4)_2(OH)_6 + 6H^+ \quad (1)$$

with A = Na, K, Rb, NH_4, Ag, H_3O, etc. Although ionic size considerations[115] suggest that the end-member lithium jarosite, i.e. $LiM_3(SO_4)_2(OH)_6$, does not exist, some solid solubility of lithium may occur in other jarosite species. For instance, trace amounts of lithium (~0.2 wt%) were observed incorporated into $KFe_3(SO_4)_2(OH)_6$[116].

Previous synthetic methods to prepare jarosites required long reaction times and the morphology of the resulting particles was hard to control. Bigham *et al.* used a thermal gradient incubator over a temperature span of 2 to 40 ^oC and reaction time of 10 days; the K,Fe-jarosite particles formed mostly aggregates composed of smooth, rounded particles with diameters on the order of 2-5 μm that were overlaid with a H_3O,Fe-jarosite crust[113]. Sandré and Gaunand used semi-batch reactors to precipitate Na,Fe-jarosite and obtained "cauliflower-like" materials about 30 μm in size after about 23 h[114]. To synthesize the vanadium analogues of the jarosite-group minerals, Dutrizac and Chen heated the reactants to 100 ^oC for 24 h and obtained precipitates as spheroidal or cauliflower-like aggregates of individual crystals about 3 μm[103].

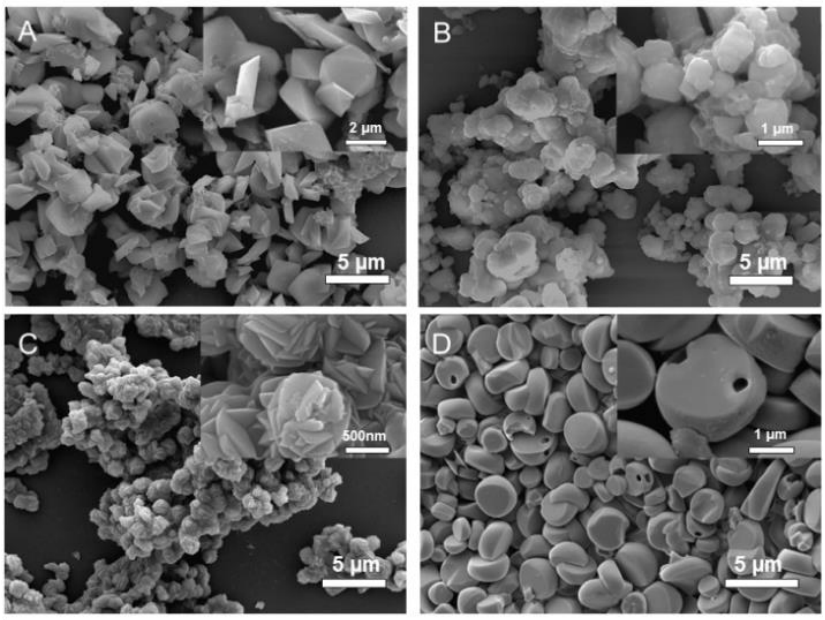

Figure 3. 2 SEM images of jarosite made using microwave-assisted hydrothermal method (A) Na,Fe-jarosite, (B) K,Fe-jarosite, (C) Na,V-jarosite, (D) K,V-jarosite.

Here, we used microwave-assisted hydrothermal synthesis to obtain jarosite with more uniform morphology using a shorter reaction time. SEM images showed that the Na,Fe-jarosite powders (**Fig. 3.2A**) were faceted polyhedra with smooth surfaces and diameters around 2-3 µm. Some of the particles were observed in aggregates. When changing the alkali metal from Na^+ to K^+, the morphology was quite different. The obtained K,Fe-jarosite particles (**Fig. 3.2B**) were found mostly as aggregates composed of smooth, rounded particles with diameters smaller than 2 µm. Similarly, the morphologies of Na,V-jarosite and K,V-jarosite (**Fig. 3.2C and Fig. 3.2D**) were quite different. The Na,V-jarosite powder consisted of rose-like aggregates with diameters of about 2 µm, while the K,V-

powders were rounded and pill-shaped with smooth surfaces. From these results, we can see that the composition plays an important role in the morphological variation of the jarosite samples. However, the morphology within each type of jarosite was fairly uniform using microwave hydrothermal reaction.

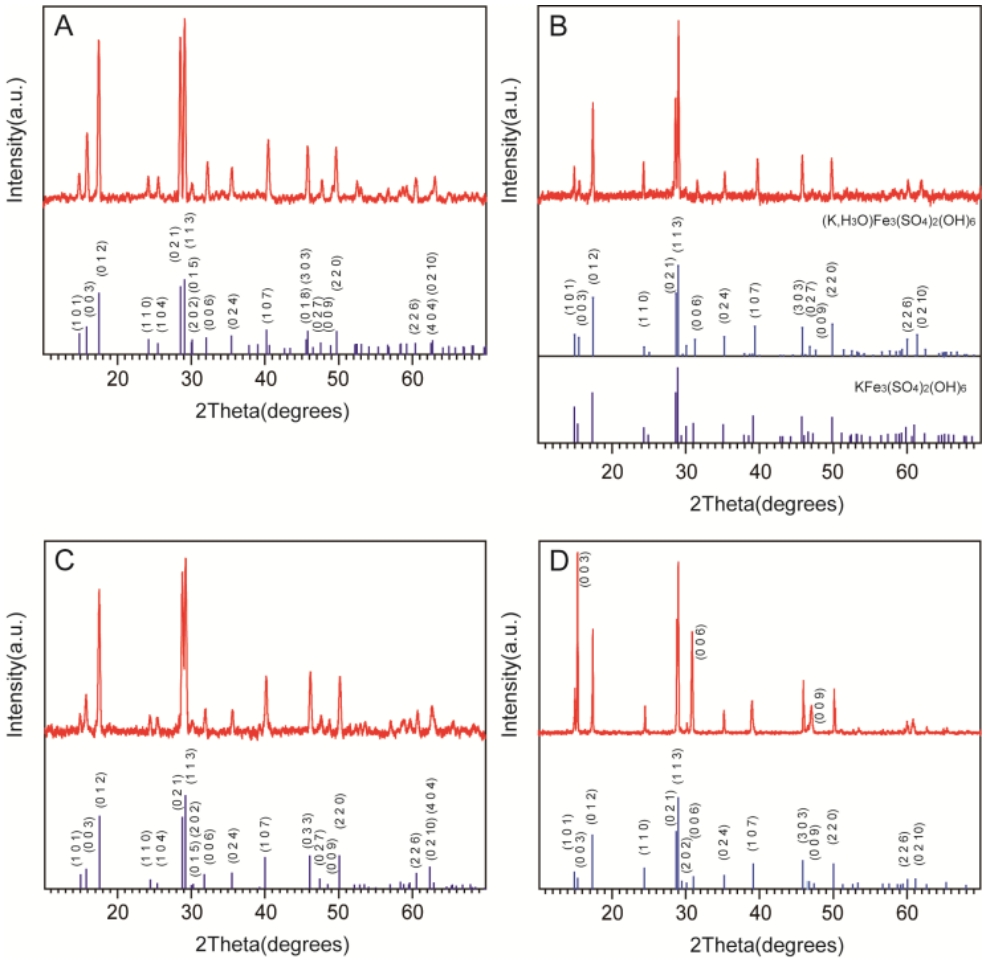

Figure 3. 3 XRD pattern of synthesized materials, brackets indicate composition from corresponding reference pattern(s). (A) Na,Fe-jarosite [$NaFe_3(SO_4)_2(OH)_6$]; (B) K,Fe-jarosite [$(K,H_3O)Fe_3(SO_4)_2(OH)_6$] and [$KFe_3(SO_4)_2(OH)_6$]; (C) Na,V-jarosite [$NaV_3(SO_4)_2(OH)_6$]; (D) K,V-jarosite [$KV_3(SO_4)_2(OH)_6$].

To identify the crystal structures of the synthesized samples, XRD was performed. **Figure 3.3** shows the XRD patterns with the reference patterns described in the Experimental Section shown for comparison. The powder XRD analysis showed that the jarosite mineral was the dominant phase in all compositions, with no other impurity phases observed. As shown in **Figure 3.3A** and **Figure 3.3C**, the reflections from the Na-containing powders showed good agreement to the peak positions and intensities in the reference patterns[112,117]. **Figure 3.3B** shows the XRD pattern of the as-synthesized K,Fe-jarosite powder. By comparing with the reference patterns for $(K,H_3O)Fe_3(SO_4)_2(OH)_6$[117] and $KFe_3(SO_4)_2(OH)_6$[118], we found that instead of pure K,Fe-jarosite, some K^+ was substituted by H_3O^+ in the as-synthesized sample, as indicated by the greater peak separation between the (101) and (003) peaks and confirmed by performing the refinement (**Table 3.1**). The XRD pattern of the K,V-jarosite (**Fig. 3.3D**) showed a good match in the peak positions to $KV_3(SO_4)_2(OH)_6$[103] with enhanced intensity in the (003), (006), and (009) reflections compared to the reference pattern. The strong (00*l*) reflections indicate a preferred orientation and suggest that the *c*-axis is along the thickness direction of the pill structures, which tend to lay flat on the substrate (**Fig. 3.2D**).

Table 3. 1 Refined site occupancy and lattice constants for jarosites.

	Na,Fe-jarosite		K,Fe-jarosite		Na,V-jarosite		K,V-jarosite	
Wyckoff Position	*a* = b = 7.337 *c* = 16.638		*a* = b = 7.320 *c* = 16.989		*a* = b = 7.306 *c* = 16.881		*a* = b = 7.273 *c* = 17.387	
	Element	Occupancy	Element	Occupancy	Element	Occupancy	Element	Occupancy
3a	Na	0.815	K	0.762	Na	0.866	K	0.847
3a	H_3O	0.185	H_3O	0.238	H_3O	0.134	H_3O	0.153
9d	Fe	0.977	Fe	0.811	V	0.909	V	1
6c	S	1	S	1	S	1	S	1
6c	O1	1	O1	1	O1	1	O1	1
18h	O2	1	O2	1	O2	1	O2	1
18h	O3	1	O3	1	O3	1	O3	1
18h	H	1	H	1	H	1	H	1

The lattice parameters and *c*/*a* values for the reference and synthesized jarosites are listed in **Table 3.2**, with the values for the synthesized powders obtained from the Rietveld refinement allowing for the possibility of H_3O^+ insertion in the structure (**Table 3.1**).

Table 3. 2 Lattice parameters *a*, *c* and *c*/*a* values from references and as-made Na,Fe-jarosite, (K,H_3O),Fe-jarosite, Na,V-jarosite and K,V-jarosite.

Jarosite	Reference (Å)			Synthesized (Å)		
	a	*c*	*c/a*	*a*	*c*	*c/a*
Na,Fe	7.32	16.59	2.27	7.34	16.64	2.27
K,Fe	7.33	17.14	2.34	7.32	16.99	2.32
Na,V	7.28	16.89	2.32	7.31	16.88	2.31
K,V	7.27	17.40	2.39	7.27	17.39	2.39

The compositions obtained from the refinement results are shown in **Table 3.3**. According to the results, both sodium compounds had a small amount of Na^+ and M^{3+} deficiency, with the iron compound showing more Na^+ deficiency but the vanadium one showing more M^{3+} deficiency.

Table 3. 3 Compositions of jarosite compounds derived from refinement results

Jarosite	Composition
Na,Fe	$Na_{0.815}(H_3O)_{0.185}Fe_{2.931}(OH_2)_{0.207}(OH)_{5.793}(SO_4)_2$
K,Fe	$K_{0.762}(H_3O)_{0.238}Fe_{2.432}(OH_2)_{1.704}(OH)_{4.296}(SO_4)_2$
Na,V	$Na_{0.866}(H_3O)_{0.134}V_{2.728}(OH_2)_{0.815}(OH)_{5.185}(SO_4)_2$
K,V	$K_{0.847}(H_3O)_{0.153}V_3(OH)_6(SO_4)_2$

The composition of the jarosites can deviate from the stoichiometric $AM_3(SO_4)_2(OH)_6$ formula due to deficiencies in A^+ and/or M^{3+}. The hydronium ion (H_3O^+) can substitute for the interlayer A^+ cation, as shown in Equation (2)[102]:

$$AM_3(OH)_6(SO_4)_2 + x\ H_3O^+ \rightarrow A_{1-x}(H_3O)_xM_3(OH)_6(SO_4)_2 \qquad (2)$$

For jarosites with M^{3+} deficiencies, H_2O can form from protonation of an intralayer hydroxyl group to maintain charge neutrality of the compound, as shown in Equation (3)[102]:

$$AM_3(OH)_6(SO_4)_2 + 3x\ H^+ \rightarrow AM_{3-x}(OH_2)_{3x}(OH)_{6-3x}(SO_4)_2 \qquad (3)$$

For the K,Fe-jarosite, 0.238 H_3O^+ was substituted for the interlayer K^+ per unit formula according to the Rietveld refinement. For (K,H_3O),Fe-jarosite, when 0.19 K^+ ions were substituted by H_3O^+, c/a = 2.3492[111], whereas for (K,H_3O),Fe-jarosite with 0.49 K^+ substituted by H_3O^+, c/a = 2.3192[119]. Due to the difference in ionic radii (K^+ is 138 pm while H_3O^+ is 99 pm)[120], the bigger K^+ increases the *c* value of the unit cell. Accordingly, the increase in *a* and decrease in *c* (and the ratio *c/a*) in this system reflects the replacement of K^+ by H_3O^+. The ratio of c/a = 2.3208 and composition obtained for the synthesized K,Fe-jarosite is consistent with these trends from the literature[113].

According to **Figure 3.1**, the *c*-axis is along the layer-stacking direction for the trivalent ion octahedra. From **Table 3.2**, the *c/a* value of the synthesized K,V-jarosite is the highest. This could reflect a slower growth rate in the *c*-direction due to the larger interlayer spacing, which may be why the K,V-jarosite forms the pill morphology with preferred orientation but the other compounds do not.

3.3.2 Electrochemical Characterization

To evaluate the electrochemical properties of the different jarosite samples, galvanostatic testing using a C/20 C-rate and potential limitation was performed on the composite electrodes.

3.3.2.1 Na,Fe Jarosite

The electrochemical properties of Na,Fe-jarosite in Li cells were previously investigated in materials prepared using conventional precipitation[105] and with nanosheet morphology[106]. In the samples prepared using the conventional precipitation method, a sloped voltage discharge (lithiation) profile with capacity ~110 mAh/g was observed between 4 – 2.0 V vs. Li/Li^+; in the nanosheets case, ~130 mAh/g was observed between 4 – 1.6 V vs. Li/Li^+ attributed to the insertion of < 3 Li^+ per formula unit, corresponding to the 1 electron reduction of each Fe^{3+}. As shown in the voltage profile and differential charge (dQ) plot (**Fig. 3.4A**), the Na,Fe-jarosites synthesized using microwave hydrothermal reaction also displayed similar characteristics in the first discharge. Ding et al. showed that the morphology of jarosite influence the electrochemical performance dramatically, the capacity of bulk jarosite is 4-13 times lower than the jarosite nanosheet[106].

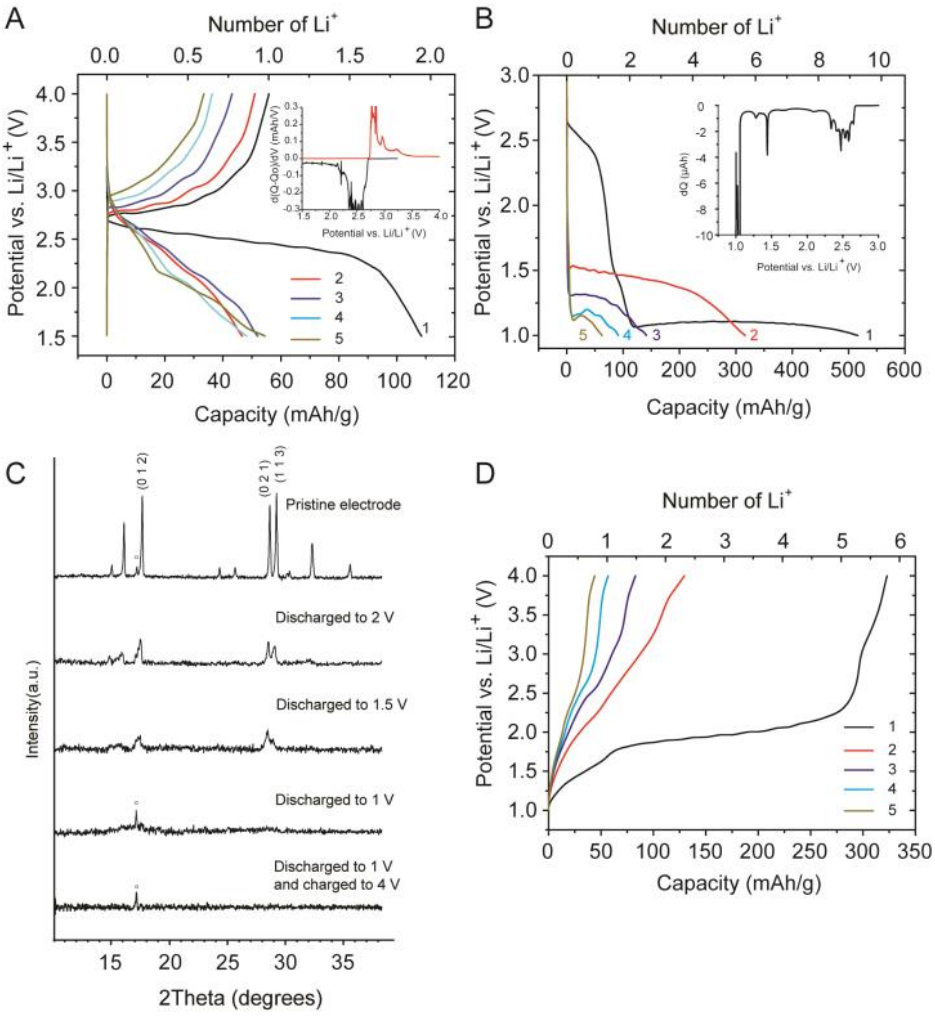

Figure 3. 4 Na,Fe-jarosite voltage profiles when (A) discharged to 1.5 and (B) 1.0 V vs. Li/Li^+; inset shows differential plot for first discharge; (C) XRD patterns of pristine Na,Fe-jarosite pristine electrode, after lithiation to different voltages, and after one full discharge/charge cycle. Peaks labelled with ○ are from the Al substrate. (D) Charge profiles after discharge to 1 V vs. Li/Li^+.

The capacity retention over many cycles (**Fig. 3.5A**) was not as good as those previously reported, likely because of the lower fraction of conducting carbon black used

in our composites (10 wt% rather than 20 wt% in the other studies[105,106]) as well as the large particle sizes. Detailed XRD and transmission electron microscopy (TEM) studies showed that lithiation of Na,Fe-jarosite caused a transformation to a disordered, amorphous structure after discharge to 2 V vs. Li/Li^+ [105]. As a result of this phase transformation, the active material could become disconnected and less electronically conducting, explaining the lower capacities after the first cycle. The slightly more sloped voltage curves starting from the second cycle are also consistent with previous observations[105]. Ex-situ XRD examination of our electrodes after discharge to 2 and 1.5 V (**Fig. 3.4C**) showed a large decrease in peak intensity, consistent with the amorphization of the Na,Fe-jarosite.

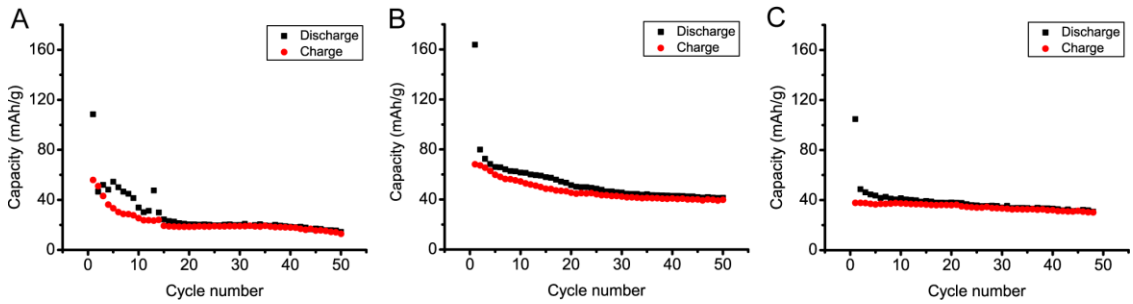

Figure 3. 5 Capacity retention of (A) Na,Fe-jarosite at 1.5 V- 4 V; (B) Na,V-jarosite at 1 V- 4 V; (C) K,V-jarosite at 1 V- 4 V.

The previous studies did not investigate the characteristics of Na,Fe-jarosite when lithiated to lower potentials. When decreasing the discharge cutoff to 1 V, the voltage curve became more sloped and the dQ plot showed new peaks centered at 1.5 and 1.2 V vs. Li/Li^+

(**Fig. 3.4B**). A flat plateau was then observed at 1.17 V. The total capacity for the first discharge was 516 mAh/g, which is slightly higher than the theoretical capacity of 498 mAh/g corresponding to insertion of 9 Li^+ per jarosite formula unit, i.e. the 3 electron reduction of Fe^{3+} to Fe^0. This suggests that Li may be first intercalated into the Na,Fe-jarosite structure at high potentials, followed by the conversion reaction at lower voltages. The observed overcapacity may be from side reactions related to the formation of a solid electrolyte interface (SEI) layer during the lithiation, which was also observed in FeF_x electrodes during discharge within the conversion reaction step between 1.7 and 1.0 V[121]. The XRD pattern of the Na,Fe-jarosite discharged to 1 V did not have reflections from jarosite or the conversion reaction products, indicating that they were amorphous. After lithiation to 1 V, the first charge capacity was 323 mAh/g, corresponding to removal of 5.84 Li^+ per jarosite (**Fig. 3.4D**). The XRD pattern of the electrode after discharge to 1 V and charging to 4 V showed the material remained amorphous (**Fig. 3.4C**).

In the second cycle when using the 1 V cutoff voltage (**Fig. 3.4B**), the sloped region > 2.0 V corresponding to the Li intercalation reaction disappeared, and instead a sloped plateau at 1.5 V was observed. The different features in the first and second cycles suggest a structural change in the first discharge that is not reversible. Presumably, the conversion reaction in the first discharge occurs at 1.1 V, while in the second cycle it increases to 1.5 V. This increase in discharge potential is also observed in Fe_2O_3 conversion electrodes.

The potential difference is as small as 0.05 V in nanostructured morphologies[122–124], but is more pronounced in micron-sized powders[125], consistent with our observations. As a result of the inductive effect caused by the more ionic sulfate and hydroxyl groups[63,64] in jarosite, the observed discharge voltages are higher than those observed in Fe_2O_3, where the plateau associated with formation of Fe^0 is usually around 0.7 V[122–126]. However, the smaller number of sulfate anions in the jarosites results in a lower discharge voltage than that observed in $Fe_2(SO_4)_3$, which is around 3.5 V[127]. Subsequent discharges were also characterized by flat plateaus, but at progressively lower potentials compared to the 2nd cycle (**Fig. 3.4B**). The capacities were observed to decrease quite rapidly, dropping quickly to 20 mAh/g after 20 cycles, which is only 4% of the first discharge capacity. This indicates a poor reversibility, likely due to the low electronic conductivity of the ionic conversion products formed. Studies on failure mechanisms in conversion electrodes also showed that the metal nanodomains formed during discharge can catalyze the formation of a SEI layer after cycling, and the SEI growth exacerbated the capacity loss[51,52,128].

3.3.2.2 K,Fe Jarosite

The electrochemical properties of K,Fe-jarosite were previously investigated by Ding *et al.* in materials prepared in a nanosheet morphology with thickness of ~13 nm[106,108] and as nanoplates grown on reduced graphene oxide[107]. In the nanosheets, redox peaks at 2.42 and 1.85 V vs. Li/Li^+ during lithiation and 2.09 and 2.97 V during delithiation were

observed during cyclic voltammetry. Galvanostatic cycling at 0.2 C revealed linear voltage curves and capacity of 117 mAh/g when cycled between 1.6 – 4.0 V vs. Li/Li^+ at a 0.2C rate, which was 13X higher than the capacities observed in the bulk sample. In the work by Ding *et al*., both the nanosheets and the bulk sample (prepared by precipitation) showed insertion-type behavior during lithiation between 2.5 – 1.5 V, followed by conversion-type behavior at lower potentials[108]. As shown in **Figure 3.6A**, the K,Fe-jarosite synthesized here displayed negligible capacity at potentials > 1.5 V, but a plateau at 1.03 V and capacity of 477 mAh/g were observed when decreasing the potential limit to 1 V vs. Li/Li^+. Compared with the jarosite nanosheet[16], the capacity retention and the performance were not as good as the nanostructured jarosite, likely because of the lower fraction of conducting carbon black used in our composites (10 wt% rather than 20 wt%) as well as the large particle sizes.

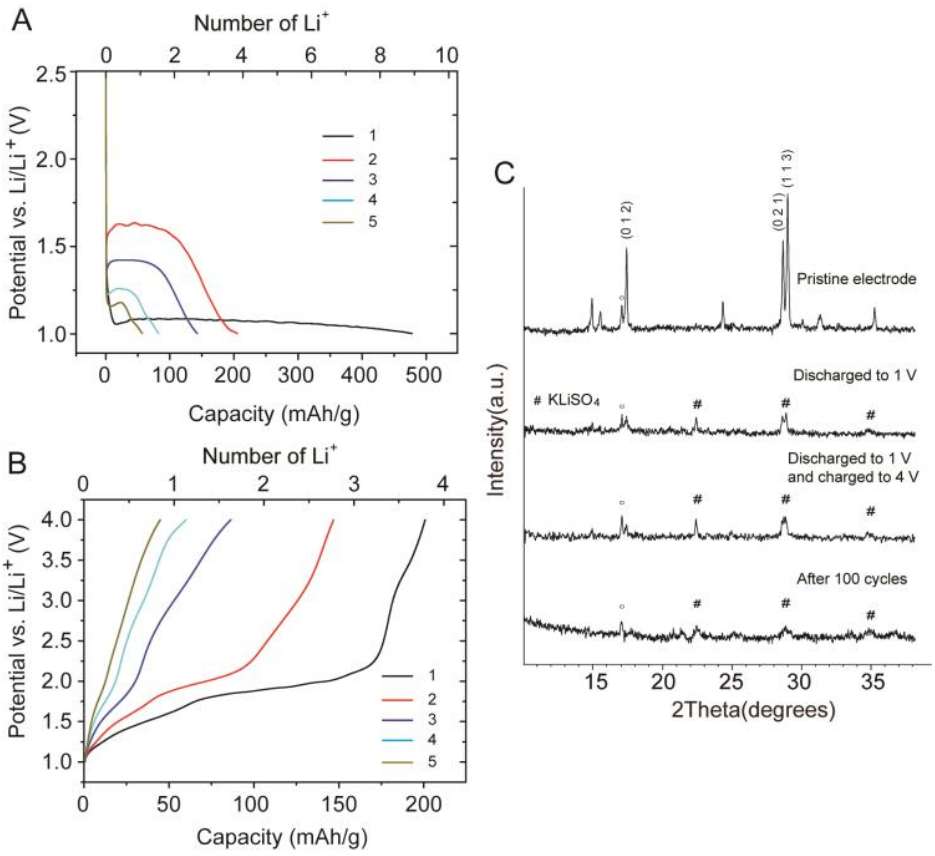

Figure 3. 6 Voltage profiles of K,Fe-jarosite (A) discharged to 1 V, (B) charged to 4 V vs. Li/Li^+. (C) XRD patterns of K,Fe-jarosite pristine electrode, after lithiation to 1 V, after one full discharge/charge cycle, and after 100 cycles. Peaks labelled with ○ are from the Al substrate and peaks labelled with # are from $KLiSO_4$.

This plateau is similar to the one observed in the previous work and is slightly lower than the theoretical capacity of 482 mAh/g corresponding to the 3 electron reduction of Fe^{3+} in $KFe_3(SO_4)_2(OH)_6$. The high discharge capacity observed in the K,Fe-jarosite despite the considerable presence of H_3O^+ and H_2O is interesting; moreover the plateau corresponding to the Fe^0 formation is at almost the same voltage as the one observed in the

Na,Fe-jarosite. The absence of the sloped profile that was observed in the Na,Fe-jarosite as well as in the K,Fe-jarosite nanosheets suggests that the K,Fe-jarosite synthesized here underwent the conversion reaction directly, without the Li^+ insertion reaction first. The *c*-lattice parameter of our synthesized K,Fe-jarosite was 16.99 Å (**Table 3.2**), smaller than that found in the nanosheets (17.224 Å), which had a reported composition of $K_{1.06}Fe_3(SO_4)_{2.11}(OH)_{5.84}$[106]. Since our Na,Fe-jarosite showed similar electrochemical characteristics as the Na,Fe-jarosite nanosheets despite the micron-sized particles, the K,Fe-jarosite data suggest that the Li^+ insertion reaction is more dependent on the jarosite composition. It is possible that the replacement of K^+ by H_3O^+ and decreased *c*-axis spacing in our K,Fe-jarosite materials prevented the Li^+ insertion reaction from occurring in the higher potential range.

Other than the first discharge, the electrochemical properties of K,Fe-jarosite were very similar to those observed in Na,Fe-jarosite. The second discharge potential was also higher at about 1.42 V, but progressively decreased in the third, fourth, and fifth discharge to 1.33, 1.16, and 1.12 V, respectively. The charge profiles (**Fig 3.6B**) also looked similar to those observed in Na,Fe-jarosite (**Fig. 3.4D**).

To study the structural changes, ex-situ XRD was performed on the fresh, lithiated and lithiated/delithiated K,Fe-jarosite electrodes. **Figure 3.6C** shows that after lithiation, all of the reflections from K,Fe-jarosite disappeared, suggesting the crystal structure

completely collapsed and became amorphous. Reflections around 2θ = 22.4, 28.7 and 34.8 were also observed during the lithiation, which is attributed to the formation of $KLiSO_4$ as a conversion reaction production.

3.3.2.3 Na,V Jarostie

To our knowledge, the electrochemical properties of the vanadium-jarosite analogs have not been previously studied. The slightly larger *c*-axis spacing in the V-jarosites, along with the decreased tendency for vanadium compounds to undergo conversion reactions compared to iron compounds, make their electrochemical investigation worthwhile. Figure 6 shows the results for the first 5 cycles for Na,V-jarosite. The first discharge capacity was 164 mAh/g, corresponding to insertion of 2.88 Li^+ per jarosite unit for formation of $Li_{2.88}NaV_3(SO_4)_2(OH)_6$, slightly lower than the theoretical value of 171 mAh/g corresponding to the insertion of 3 Li and reduction of V^{3+} to V^{2+}, as shown in Equation (5).

$$NaV_3^{3+}(SO_4)_2(OH)_6 + 3Li^+ + 3e^- \rightarrow Li_3NaV_3^{2+}(SO_4)_2(OH)_6 \quad (5)$$

The first charge capacity was 68 mAh/g, corresponding to removal of 1.19 Li^+ per jarosite unit, and resulting in the formation of $Li_{1.69}NaV_3(SO_4)_2(OH)_6$. Subsequent discharges showed reversible insertion of about 1.1 Li^+ per jarosite with a sloped voltage profile between 1.0 – 1.5 V vs Li/Li^+. The capacity decreased gradually with cycling, reaching about 40 mAh/g after 30 cycles (**Fig. 3.5B**).

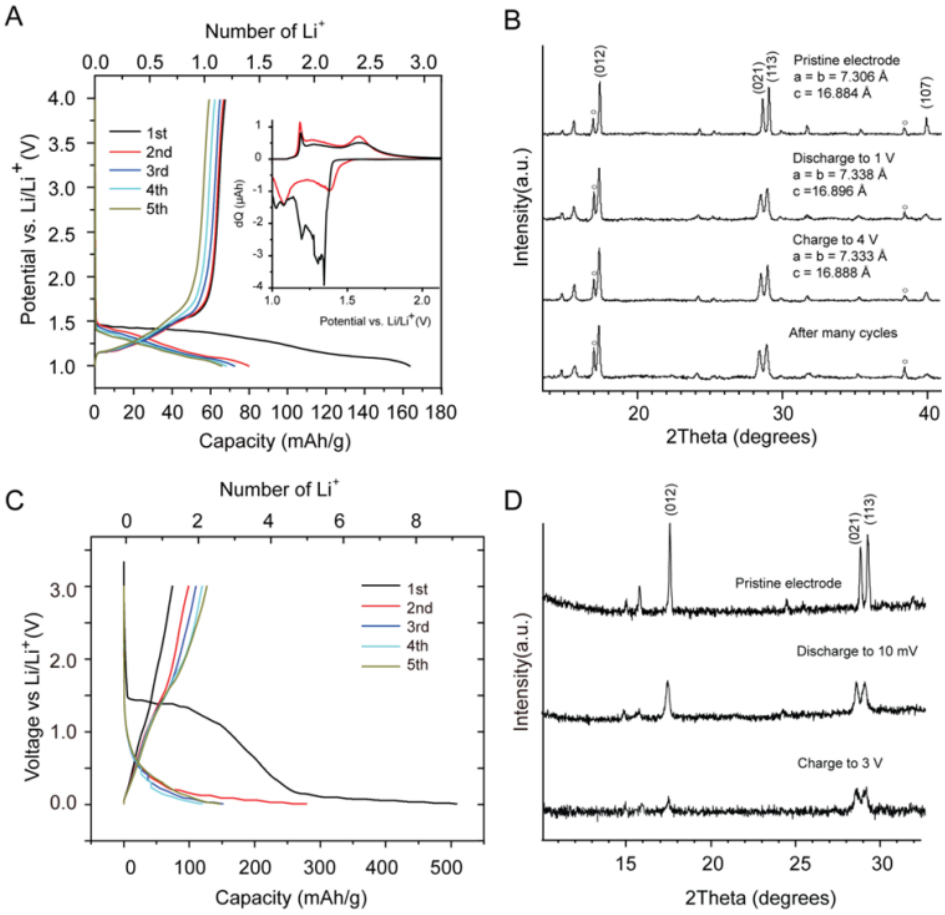

Figure 3. 7 Na.V-jarosite (A) voltage profile with differential charge plot for first 2 cycles in inset and (B) XRD after cycling between 1 – 4 V vs. Li/Li^+; (C) voltage profile and (D) XRD after cycling between 10 mV – 3 V vs. Li/Li^+.

The reduction peaks in the dQ plot of the first discharge (**Fig. 3.7A, inset**) may include contributions from the formation of SEI layer, and the dQ plots of the following cycles show two broad peaks at about 1.4 and 1.1 V, which are attributed to the reversible insertion of Li^+. This may be similar to the Li^+ insertion process associated with the V^{3+}/V^{2+} couple in $Li_xV_2(PO_4)_3$, which shows two reduction peaks at 1.74 and 1.66 V due to the presence

of a phase transition[129]. The potentials in the Na,V-jarosite are lower due to the presence of hydroxide groups, which decrease the voltage due to the induction effect. During charging, there is a sharp peak in the dQ plot at around 1.2 V during charging, which may be from Li^+ insertion into the Na vacancies first, followed by the two broad peaks at 1.3 and 1.6 V corresponding to Li^+ extraction.

The ex-situ XRD patterns (**Fig. 3.7B**) showed the Na,V-jarosite structure remained stable during discharging and charging, even after many cycles. Compared with the pristine electrode, the peaks in the lithiated jarosite were broader, but the positions were quite similar, indicating little volume change after Li^+ insertion. According to the Wyckoff positions in the $R\bar{3}m$ space group (#166), there are two empty positions, the 9*e* and 3*d* sites, which could potentially be occupied by Li^+ ions (**Fig. 3.8**). As shown in **Figure 3.8B**, the 9*e* sites are found in the empty spaces between the V-O octahedra layers, in the same layer as the Na^+, while the 3*d* sites are found in the same layer as the V-O octahedra (**Fig. 3.8D**). According to ref.[105], Li^+ intercalation into jarosite compounds tend to separate the octahedra layers, so the 9*e* sites are the more likely sites for Li^+ insertion, even though the 3*d* sites seem to along the empty tunnels seen when viewing along the [210] direction (**Fig. 3.8C**). When comparing the calculated diffraction patterns for pristine Na,V-jarosite with that for Na,V-jarosite containing 3 Li^+ per formula unit in the 9*e* position (**Fig. 3.9**), the main difference is that the ratios of peak intensities (012)/(003), (012)/(021), (012)/(113),

and (012)/(107) all increase in the lithiated material (**Table 3.4**), a trend we also observed in our experimental patterns.

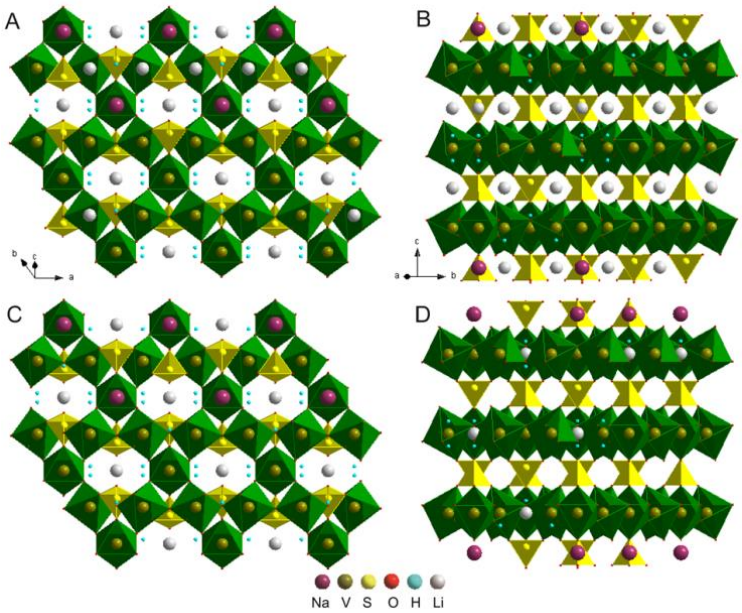

Figure 3. 8 Crystal structure image of Na,V-jarosite with Li^+ in 9*e* sites viewing (A) along the [-1-21] direction and (B) along the [210] direction; Li^+ in 3*d* sites (C) along the [-1-21] direction and (D) along the [210] direction.

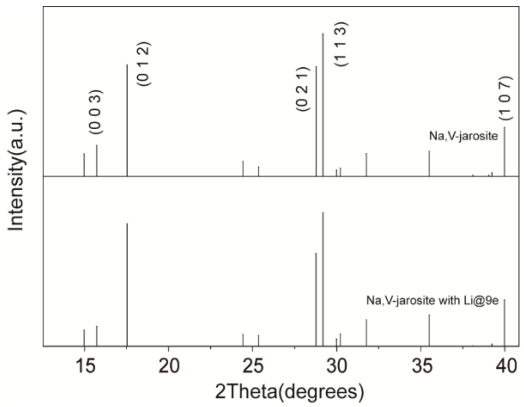

Figure 3. 9 Comparison of XRD patterns for Na,V-jarosite and Na,V-jarosite containing 3 Li in the 9*e* sites calculated in Diamond.

Table 3. 4 Comparison of peak intensities in calculated XRD patterns for Na,V-jarosite and Na,V jarosite containing 3 Li in the 9*e* sites

hkl	Peaks ratio (012)/(hkl) in jarosite	Peaks ratio (012)/(hkl) in jarosite with Li in 9e sites	Change
003	3.63	6.17	increase
012	1.00	1.00	
021	1.01	1.32	increase
113	0.78	0.92	increase
107	2.28	2.64	increase

After charging to 4 V, the aforementioned peak intensity ratios decreased, indicating the removal of Li^+ from the 9*e* position. However, the diffraction intensities of the delithiated Na,V-jarosite were not as strong as in the pristine electrode, suggesting that not all of the inserted Li^+ were removed. From the voltage profile (**Fig. 3.7A**), 2.88 Li^+ were inserted per formula unit, but only about 1 Li^+ was removed, consistent with the XRD pattern analysis. When looking along the [-1-21] direction, one-third of the Li^+ sit in empty channels, while the rest reside in between the vanadium octahedra (**Fig. 3.8A**); these Li^+ may be harder to remove during the charge, which can explain the higher capacity of the first discharge capacity compared to the first charge capacity. Hence, the reversible cycling of ca. 1 Li^+ after the first discharge may be facilitated by the 9*e* sites in the open channels. Rietveld refinement was performed on the lithiated and delithiated electrodes and the lattice

parameters are shown in **Figure 3.7B**. After discharge to 1 V, both *a* and *c* lattice parameters increased, but then decreased after charging to 4 V. This suggests that Li^+ insertion leads to an expansion of the unit cell and extraction of the Li^+ causes the volume to decrease back.

Similar to the Na,Fe-jarosite, when discharging Na,V-jarosite to lower potentials, the reaction changed to a conversion mechanism. **Figure 3.7C** shows the voltage profiles for Na,V-jarosite cycled between 10 mV – 3 V. The first discharge capacity reached 508 mAh/g corresponding to insertion of 8.9 Li^+, but dropped in subsequent cycles. XRD analysis after cycling showed that the peak intensities greatly decreased (**Fig. 3.7D**), suggesting amorphization, although some Na,V-jarosite peaks were still present after the first charge to 3 V. This is likely due to the presence of unreacted material.

3.3.2.4 K,V Jarosite

The voltage profiles for K,V-jarosite cycled between 1 – 4 V vs. Li/Li^+ were similar to those observed in Na,V-jarosite (**Fig. 3.10**). The first discharge capacity was 105 mAh/g, corresponding to insertion of 1.90 Li^+ per jarosite for formation of $Li_{1.9}KV_3(OH)_6(SO_4)_2$. The first charge was 38 mAh/g, corresponding to removal of 0.68 Li^+ per formula unit. Subsequent discharges showed reversible insertion of about 0.7 Li^+ per jarosite with a sloped voltage profile between 1.0 – 1.5 V vs Li/Li^+. Similar to Na,V-jarosite, the XRD

patterns of the lithiated and delithiated electrodes showed no large structural changes, which is consistent with an insertion reaction.

Again, just as in the other jarosites, K,V-jarosite underwent a conversion reaction when discharged < 1 V. Figure 8C shows the voltage profiles for K,V-jarosite cycled between 10 mV – 3 V. The first discharge capacity reached 508 mAh/g corresponding to insertion of 8.9 Li^+, but dropped in subsequent cycles. The discharge capacity of the second cycle was only 184 mAh/g, less than half of the first discharge capacity. XRD analysis after cycling showed that the peak intensities greatly decreased (**Fig. 3.10D**), suggesting amorphization, and some reflections due to the presence of unreacted material were still present.

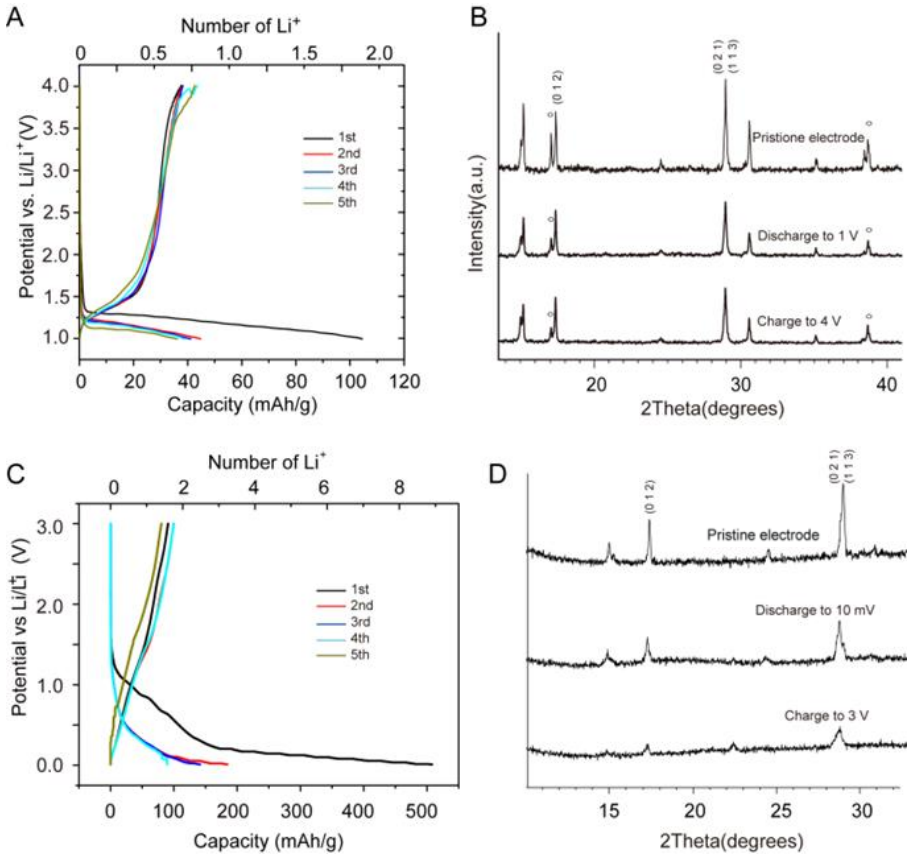

Figure 3. 10 K,V-jarosite (A) voltage profiles and (B) XRD after cycling between 1- 4 V vs. Li/Li^+; (C) voltage profiles and (D) XRD after cycling between 10 mV- 3 V vs. Li/Li^+.

3.3.2.5 Na Intercalation

As the open framework structure in the jarosite may be able to facilitate the diffusion of larger cations, we chose Na,V-jarosite to further study the electrochemical properties in Na-cells. Galvanostatic testing using a C/20 C-rate and potential limitation between 1 – 4 V vs. Na/Na^+ was performed. **Figure 3.11A** shows the voltage profiles and the number of Na^+ per unit formula for the first 5 cycles. In the first charge, the capacity observed at

around 3.1 V was equivalent to about 0.74 Na^+ extracted from $Na_{0.866}(H_3O)_{0.134}V_{2.728}(OH_2)_{0.815}(OH)_{5.185}(SO_4)_2$, but only 0.06 Na^+ could be inserted back. After the first cycle, the capacity dropped rapidly, with only about 0.13 Na^+ per formula unit reversibly inserted. Figure 9B shows the XRD patterns of the fresh electrode, sodiated electrode and sodiated/desodiated electrode. The peak positions remained the same, which indicates the structure did not change during the electrochemical process. It is possible that the capacity observed in the first charge is due to the oxidation of electrolyte or other side reactions. Although the Na,V-jarosite showed reversible Li^+ insertion, it may not be suitable as an electrode for Na-ions due to the larger size of Na^+ compared to Li^+.

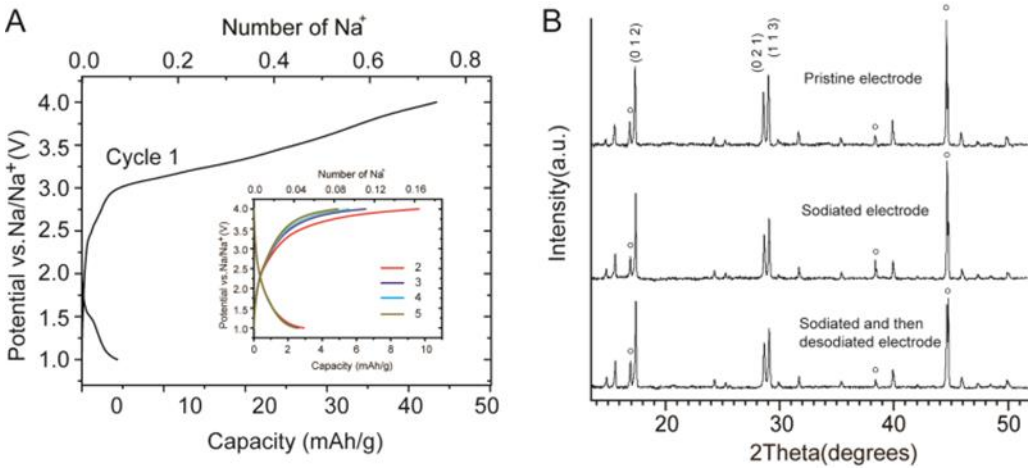

Figure 3. 11 (A) Voltage profiles of Na,V-jarosite discharged/charged in Na-half cells; (B) XRD patterns of the fresh, sodiated and sodiated/desodiated electrodes.

3.4 Conclusion

In conclusion, we found that jarosite compounds can undergo electrochemical reactions with lithium but not with sodium and may be promising candidates as new electrode materials. The work presented here demonstrates the basic voltage dependent behavior of these jarosite compounds as a function of composition and establishes the baseline for future studies that may seek to improve the cyclablity and capacity retention through strategies that have been used for other polyanion materials, such as particle-size reduction, advanced nanostructured architectures, and carbon coating. In general, the trivalent metal played an important role in the reaction mechanism and the alkali metal also influenced the reaction voltage.

A first discharge capacity of 477 mAh/g was observed in K,Fe-jarosite and 516 mAh/g was observed for Na,Fe-jarosite, consistent with the 3 electron reduction of Fe^{3+} and conversion reaction mechanism at low potentials. During the first discharge, Na,Fe-jarosite underwent a Li^+ insertion reaction first at potentials > 1.5 V vs. Li/Li^+, followed by a conversion reaction. This insertion reaction was not observed in K,Fe-jarosite due to the substitution of some K^+ for H_3O^+ during the synthesis, which decreased the interlayer spacing and inhibited Li^+ insertion. XRD characterization suggested that the discharge products after the conversion reaction were amorphous or too small to be detected by X-

rays, small reflections associated with crystalline $KLiSO_4$ were observed in the discharged K,Fe-jarosite.

Na,V and K,V-jarosite demonstrated close to the theoretical discharge capacity based on the 1 electron reduction of V^{3+}, with about one Li^+ and one electron inserted and extracted per unit formula starting from the second cycle. XRD characterization suggested that the structure did not change during the discharge and charge process, which indicated an insertion reaction mechanism. A capacity of 164 mAh/g was observed in the first discharge for Na,V-jarosite and 105 mAh/g for K,V-jarosite. Lithiation of the vanadium jarosites to lower potentials also resulted in conversion-type reactions. The capacity in the first charge was 40 mAh/g for Na,V-jarosite in Na half-cells, but subsequent low capacities suggested that very little sodium could be reversibly extracted/inserted. These studies show that the jarosite compounds could be promising candidates for the development of new electrodes for Li-ion batteries. Future work on development of nanostructured jarosites may lead to materials with better capacity retention and rate performance.

4: HTPS AS CATHODE ELECTRODE FOR LITHIUM-ION AND SODIUM-ION BATTERY

4.1 Introduction

Since Na^+ ion transport through the sodium superionic conductor $Na_{1+x}Zr_2P_{3-x}Si_xO_{12}$ (NASICON) was first observed[130,131], compounds with similar rhombohedral structures have been widely studied for applications in fuel cells, gas sensors, and batteries[132–134]. In particular, NASICON-type phosphates with general chemical formula $A_xM_2(PO_4)_3$ (A = Li or Na, M = Ti, V, and Fe) have been investigated as solid electrolytes[135–137], cathodes for Li-ion and Na-ion batteries[138–142] and anodes for aqueous based batteries[143,144]. These compounds contain a three-dimensional (3D) framework of PO_4 tetrahedra that are corner-shared with MO_6 octahedra. Substitutions are possible at various lattice sites and the open 3D crystal structure enables easy diffusion of alkali cations within the channels.

The physicochemical and electrochemical properties of NASICON-type compounds can be tuned through mixing of the tetrahedral oxoanions. For instance, previous reports have shown that the Li^+ conductivity in titanium phosphates could be improved by doping the materials with silicate[145,146], vanadate[147–149], and niobate[147–149]. The lithium/delithiation potential can furthermore be tuned using the induction effect, whereby the redox energies of the transition metal ions are affected by the electronegativity and bond strength with the oxoanions[150–152]. For example, insertion of Li^+ into rhombohedral forms of $Fe_2(SO_4)_3$ and $Li_3Fe_2(PO_4)_3$ showed that the position of the Fe^{3+}/Fe^{2+} redox couple was at 3.6 and 2.8 V

vs. Li^+/Li, respectively; when phosphate was substituted with sulfate, the Fe^{3+}/Fe^{2+} redox couple for rhombohedral $LiFe_2(SO_4)_2(PO_4)$ was observed at 3.3 – 3.4 V vs. Li^+/Li[151].

Recently, new hydrogen titanium phosphate sulfate (HTPS) compounds were synthesized using a peroxide-based sol-gel method[153] with composition $H_{1-x}Ti_2(PO_4)_{3-x}(SO_4)_x$ (x = 0.5 – 1) and structure resembling that of $LiTi_2(PO_4)_3$ (LTP) (**Fig. 4.1**). In LTP (space group $R\bar{3}c$), two Li^+ ions may be intercalated through a two-phase reaction mechanism at 2.5 V vs. Li/Li^+ to form $Li_3Ti_2(PO_4)_3$ (space group $R\bar{3}$). There are two types of cavities in the NASICON-type structure, with the M1 site located between two TiO_6 octahedra along the *c*-axis, and the M2 cavities found surrounding the M1 sites[154] (**Fig. 4.1B**). The Li^+ ions in LTP reside solely within the M1 cavities, while in $Li_3Ti_2(PO_4)_3$ the M1 sites are empty and the Li^+ ions fully occupy the M2 sites[142]. The flat voltage plateau observed during lithiation of LTP is attributed to the filling of the M2 cavity through a mechanism that involves cooperative migration of Li^+ from the M1 to M2 sites[139].

In HTPS, the formation of the alkali-free NASICON-type phase is proposed to be stabilized by incorporation of sulfate ions (present from the $TiOSO_4$ precursor used in the synthesis) to create the mixed polyanion compound[153]. Unlike other reported NASICON-type compounds that contain only phosphate anions, in HTPS the 6*b* sites are filled with protons to maintain charge neutrality due to the presence of the two differently charged tetrahedral oxoanions. Both sulfate and phosphate anions are found in the 18*e* sites with P/S ~ 2.57 (**Fig. 4.1A**).

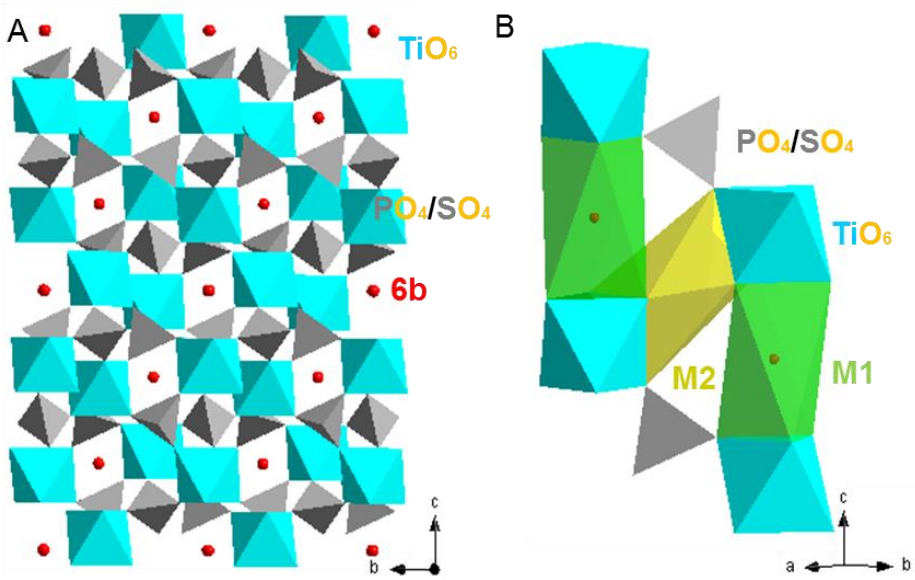

Figure 4. 1 HTPS crystal structure (A) HTPS structure viewed along the *a*-axis to illustrate the ion channels. (B) M1 and M2 sites in the HTPS structure. The PO_4/SO_4 tetrahedra are shown in grey, the TiO_6 octahedra are shown in blue, M1 sites are in green, M2 sites are in yellow, and the 6*b* sites are in red.

Here we report, for the first time, the electrochemical properties of HTPS and a detailed study comparing the lithiation and sodiation reaction mechanisms with those found in other NASICON-type compounds. Four different types of HTPS samples, namely the as-prepared, ball-milled (BM-HTPS), heat treated (500-HTPS), and carbon composite (C-HTPS) materials, were studied and evaluated in Li-ion cells. We find that different from lithiation in LTP, the lithiation mechanism of HTPS is a two-step process, whereby the Li^+ first insert into the M1 sites at ca. 2.8 V vs. Li/Li^+ followed by insertion into the M2 sites at ca. 2.5 V. This makes HTPS more similar to Mn-NASICON compounds such as $Mn_{0.5}Ti_2(PO_4)_3$ than to LTP. The reaction of ambient H_2O with H^+ to form H_3O^+ within the HTPS structure can block Li^+ insertion, but the H_2O can be removed by heating the

electrode prior to electrochemical testing. We find that HTPS also can be used as a sodium battery cathode in a similar two-step sodiation process at ca. 2.9 and 2.2 V vs. Na/Na^+, with a discharge capacity of about 90 mAh g^{-1} remaining after 50 cycles.

4.2 Experimental Methods

4.2.1 Synthesis of HTPS

4.2.1.1 HTPS

5.8 g $TiOSO_4 \cdot 0.18\ H_2SO_4 \cdot 3.11\ H_2O$ (Sigma-Aldrich) was dissolved in 11.3 g of deionized water into which 3.3 g of a 27 wt% H_2O_2 solution (Alfa Aesar) was subsequently added. The solution was stirred until it became homogeneous. To this solution, 3.6 g of 85 wt% H_3PO_4 solution (Alfa Aesar) was added and dissolved with stirring until the solution became homogeneous. This solution was left loosely covered at 60 °C for one day during which it turned opaque and orange colored as to form an orange-white spongy solid. This solid was heated at 650 °C in air for 10 h and formed a white product. This white product was washed with deionized water three times.

4.2.1.2 BM-HTPS

Ball milling was performed on the as-synthesized HTPS and C-HTPS using a SPEX 8000 mill with a hardened steel vial (SPEX 3127) for 1 h to decrease the aggregate particle size.

4.2.1.3 500-HTPS

The as-synthesized HTPS was heated in a tube furnace at 500 °C for 8 h under Ar to remove water.

4.2.1.4 C-HTPS

Carbon composites with HTPS were prepared by incorporating glucose as a carbon precursor into the HTPS synthesis. 3.9 g $TiOSO_4 \cdot 0.18\ H_2SO_4 \cdot 3.11\ H_2O$ (Sigma-Aldrich) was dissolved in 12.0 g of deionized water into which 3.5 g of 27 wt% H_2O_2 solution (Alfa Aesar) was subsequently added. The solution was stirred until it became homogeneous. To this solution, 3.1 g of 85 wt% H_3PO_4 solution (Alfa Aesar) was added and dissolved with stirring until the solution became homogeneous. To this solution, 1.9 g of *d*-glucose (Sigma) was added and dissolved with stirring until the solution became homogeneous. This solution was left at 70 °C for one day, which resulted in a black, semi-liquid paste. The product was heated at 650 °C under Ar for 10 h in a tube furnace to form a black product.

4.2.2 Materials Characterization

4.2.2.1 Elemental Analysis

Elemental analysis of the as-prepared HTPS was performed using a Thermo iCAP6300 inductively coupled plasma optical emission spectrometer (ICP-OES) to determine the amount of Ti, P, and S in samples acid digested with microwave-assistance.

4.2.2.2 Thermogravimetric Analysis

Thermogravimetric analysis (TGA) was performed using a Mettler-Toledo TGA/DSC 1 STARe system. The analysis was carried out by heating from 25 to 1000 °C at a rate of 20 °C/min, holding for 0.5 – 2 h, and then cooling to room temperature. During the analysis,

the furnace was purged with air at 50 mL/minute. The amount of carbon in the HTPS carbon composites was determined from the weight loss between 450 and 600°C, which is below the temperature at which HTPS decomposes[153].

4.2.2.3 Nitrogen Adsorption

Nitrogen sorption isotherms were collected on a Micromeritics ASAP 2020 surface area and porosity analyzer at 77 K. Samples were degassed under vacuum at 200 °C for 8 h. To calculate the surface areas, the Brunauer-Emmett-Teller (BET) model was applied to the partial pressure range of 0.05 – 0.2 of the adsorption branch of the isotherm. The desorption branch was analyzed by applying the Barrett-Joyner-Halenda (BJH) model using the Halsey thickness curve, heterogeneous surfaces, and Faass correction to account for multilayer desorption in estimating the thickness of the adsorbed nitrogen to calculate pore-size distribution[155]. The total quantity of gas adsorbed at the data point closest to P/P_0 = 0.98 on the desorption branch was used to approximate the total pore volume.

4.2.2.4 X-ray Diffraction

Powder X-ray diffraction (PXRD), scanning electron microscopy (SEM), and X-ray photoelectron spectroscopy (XPS) were used to perform structural and chemical characterization of the prepared HTPS powders and composite electrodes before and after electrochemical cycling. For PXRD and XPS, the electrodes were rinsed several times with ethanol and dried at 50 °C overnight. PXRD data were collected using a Panalytical X'pert Pro diffractometer with CuKα radiation operating at 40 kV/40 mA.

4.2.2.5 Electron Microscopy

Scanning electron microscopy (SEM) imaging was performed using an XL 30 ESEM-FEG microscope and a 20 kV electron beam. For mounting the samples, the powder sample was dusted onto carbon tape on an SEM stub, whereas electrodes were imaged directly, and after rinsing in the case of used electrodes. Transmission electron microscopy (TEM) observation was carried out on a JEOL 2010F microscope using 200 kV. For TEM, the HTPS particles were dispersed into ethanol with ultrasonication for five minutes. Then, a copper and lacy carbon TEM grid was dipped into the dispersion and the ethanol was allowed to evaporate.

4.2.2.6 X-ray Photoelectron Spectroscopy

XPS was performed on a VG ESCALAB 220i-XL with Al Kα anode (1486.6 eV) operating at 60 W and 12 kV. The X-ray takeoff angle was 45° and the data were acquired from the region within ~500 μm of the outer surface of the sample. Charge compensation was used because HTPS is an insulator. A pass energy of 20 eV was used for high-resolution spectra (energy resolution 0.7 eV). The spectra were calibrated to the hydrocarbon peak at 284.5 eV. Peak fitting was performed using CasaXPS processing software.

4.2.3 Electrochemical Characterization

Composite electrodes were prepared by mixing the HTPS active material with polyvinylidene difluoride (PVDF) binder (Kynar) and SuperP Li carbon black (TimCal) with a ratio of 80:10:10 by weight. N-methyl-2-pyrrolidone was added dropwise and the slurry was then stirred overnight. This slurry was then coated onto a piece of Al foil with

doctor blading. The slurry-coated Al foil was dried in an oven at 120 ºC for about 5 h to remove any residual solvent. The foil was then punched into disks using a compact precision disc cutter (MSK T07) and weighed prior to electrochemical testing. Coin cells (CR2032) were assembled in an Ar-filled glove box using lithium metal foil as the anode, Celgard 2500 as separator, and 1 *M* $LiPF_6$ in EC: DMC (1:1 by vol, MTI) as electrolyte. HTPS was also evaluated in Na half-cells using Na metal as the anode, glass microfiber filter (Whatman GF/F) as separator, and 1 M $NaClO_4$ in propylene carbonate (PC) as electrolyte (BASF). Galvanostatic measurements were performed between 2 – 3.4 V vs. Na^+/Na with a current density of 7 mA g^{-1}.

4.2.3.1 Galvanostatic/Potentiodynamic Measurements

Galvanostatic or potentiodynamic measurements were performed on a BioLogic VMP3 between 2 – 3.4 V vs. Li^+/Li unless otherwise noted. For galvanostatic measurements, C-rates were determined using a theoretical capacity of 140 mAh/g, according to the insertion of 2 Li^+ per HTPS formula unit. The current densities corresponding to the C-rates are as follows: C/20 (7 mA/g), C/10 (14 mA/g), C/5 (28 mA/g), C/2 (70 mA/g), 1C (140 mA/g). For potentiodynamic measurements, a 5 mV voltage step was used with a threshold current density of 7 mA/g.

4.2.3.2 Galvanostatic Intermittent Titration

Galvanostatic intermittent titration (GITT) measurements were performed with the amount of charge passed in each step limited to 7 mAh/g, followed by relaxation at open circuit for 3 h or until the open circuit drift over time decreased to 1 mV/h. The chemical diffusion coefficient of the Li^+ (Na^+) ion was calculated using Equation (1): [59]

$$D = \frac{4}{\pi}\left(\frac{mV_M}{M_w S}\right)^2 \left(\frac{\Delta E_s}{\tau^{dE/dt^{1/2}}}\right)^2, \qquad t \ll L^2/D \tag{1}$$

where D (cm^2/s) is the chemical diffusion coefficient, m is the mass of the HTPS, V_M is the molar volume of $H_{0.39}Ti_2(PO_4)_{2.39}(SO_4)_{0.61}$ (135.12 cm^3/mol), M_w is the molecular weight (381.73 g/mol), S is the active surface area of the electrode, τ was the time duration of the applied current (60 min), ΔE_s is the change in the steady-state voltage over the titration step, E is the voltage, t is the time and L is the thickness of the electrode. In our calculations, we assumed that V_M remained a constant with the discharge and charge in the cathode, the active surface area of the electrode was the geometric surface area. If E vs. $t^{1/2}$ shows linear behavior over the entire period of applied current, then equation (1) can be simplified to the form shown in equation (2), with ΔE_t representing the change in cell voltage during the current pulse, neglecting the IR drop [59]:

$$D = \frac{4}{\pi\tau}\left(\frac{mV_M}{M_w S}\right)^2 \left(\frac{\Delta E_s}{\Delta E_t}\right)^2, \qquad t \ll L^2/D \tag{2}$$

4.2.3.3 Electrochemical Impedance Spectroscopy

Electrochemical impedance spectroscopy (EIS) was performed on fully charged electrodes in the frequency range of 10 mHz – 1 MHz.

4.3 Results and Discussion

4.3.1 Structural Characterization of Synthesized HTPS

4.3.3.1 Morphology

SEM imaging showed that the as-made HTPS particles were formed as loose aggregates (**Fig. 4.2A**), which were revealed using TEM observation to be composed of nanoparticles smaller than 50 nm (**Fig. 4.2B**). Nitrogen sorption isotherms and BJH pore size distributions revealed that the BET surface area of the as-made HTPS was 78 m^2/g and that the pore volume was 0.22 cm^3/g (**Fig. 4.3**). The average pore width was 11 nm, which confirmed the presence of textural meso- and macropores in the material[153]. Since some of the aggregates were very large, approaching 500 μm in size, ball-milling was performed to decrease the aggregate particle size. SEM imaging showed that the size of the ball-milled HTPS (BM-HTPS) aggregates was decreased to about 2 μm (**Fig. 4.2C**).

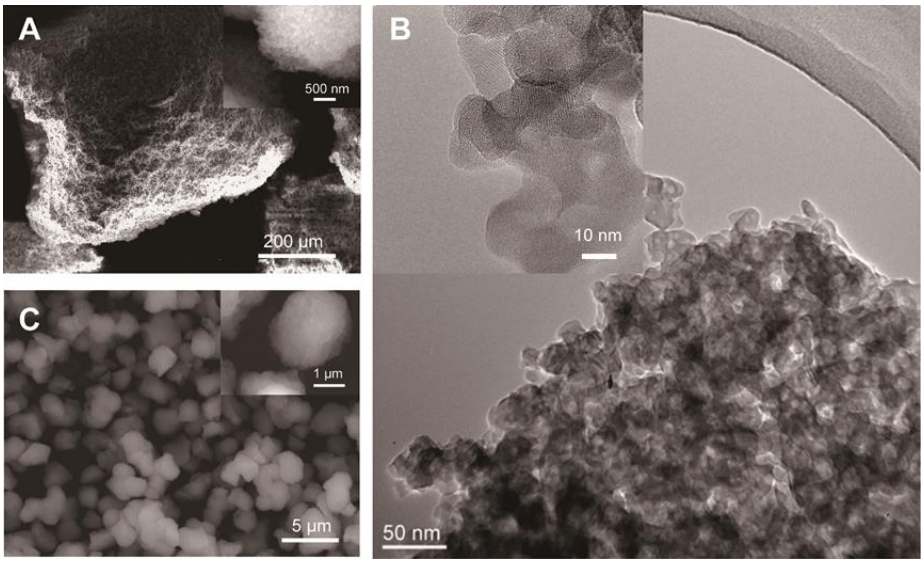

Figure 4. 2 (A) SEM and (B) TEM images of as-made HTPS; (C) SEM images of HTPS after ball milling (BM-HTPS)

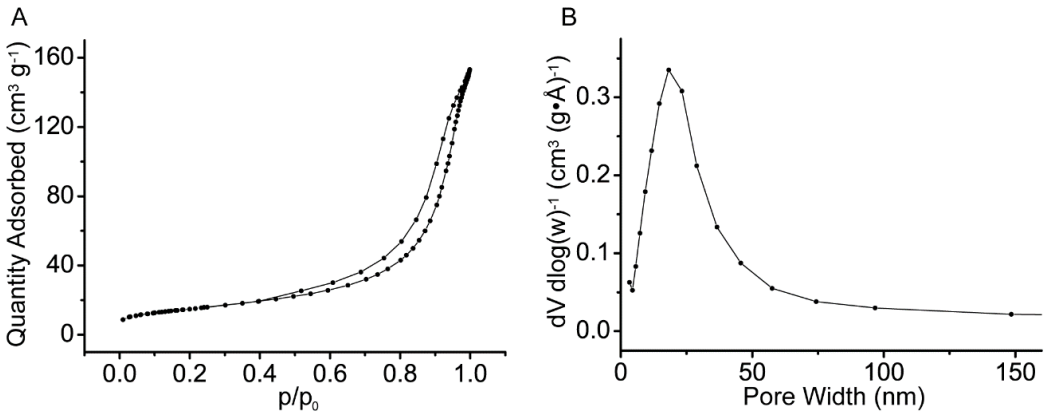

Figure 4. 3 Nitrogen sorption isotherms and BJH pore size distributions of as-made HTPS.

4.3.3.2 X-ray Diffraction

PXRD was performed on the as-made HTPS, BM-HTPS, and C-HTPS samples to elucidate the crystal structure (**Fig. 4.4**). The obtained patterns matched the simulated PXRD pattern of a hypothetical $HTi_2(PO_4)_3$ compound (space group: $R\bar{3}c$; a = 8.467 Å; c = 21.69 Å) which was derived by replacing the Li^+ in the M1 sites of the $LiTi_2(PO_4)_3$ structure with protons[153]. The crystallite size determined using the Scherrer equation on the PXRD pattern of the as-made HTPS was 22.7 nm, consistent with TEM observations. No diffraction peaks from impurities were observed and neither the ball-milling nor carbon composite processing appeared to affect the crystallite size or the lattice constants of the HTPS.

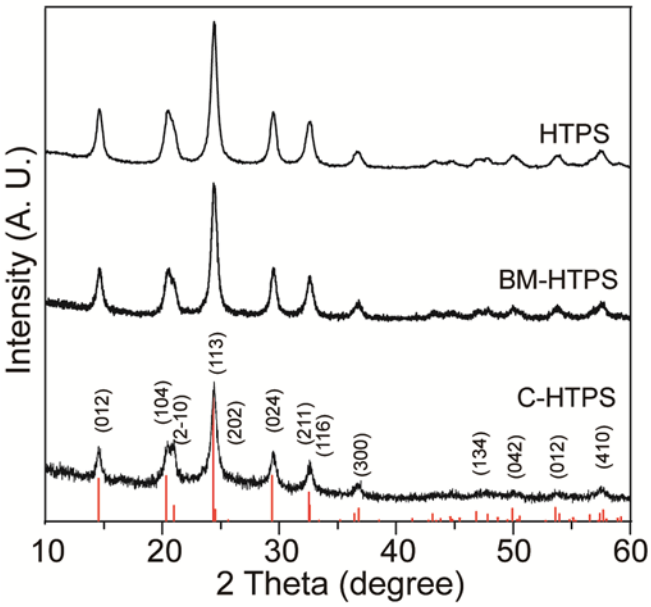

Figure 4. 4 PXRD patterns of as-made HTPS, BM-HTPS and C-HTPS. The red vertical lines represent the simulated powder pattern of $HTi_2(PO_4)_3$ based on a NASCION structure with protons in the M1 sites.

4.3.3.3 Elemental Analysis

To obtain the composition of HTPS, ICP-OES elemental analysis was performed on digested samples using the assumption that the stoichiometry can be written as $H_{1-x}Ti_2(PO_4)_{3-x}(SO_4)_x$ to maintain charge neutrality[153]. According to the ICP-OES result, x = 0.61, resulting in a formula of $H_{0.39}Ti_2(PO_4)_{2.39}(SO_4)_{0.61}$. Due to the presence of two Ti^{4+} species per formula unit (f.u.) in HTPS, a theoretical capacity of 140.4 mAh/g corresponding to formation of $(Li_{0.6}H_{0.4})Li_{1.4}Ti_2(PO_4)_{2.4}(SO_4)_{0.6}$ is expected. Due to the partial occupancy of the M1 sites by protons, it is expected that the Li^+ ions can be shared between the M1 (0.6 occupancy) and M2 (1.4 occupancy) sites.

4.3.2 Electrochemical Characterization

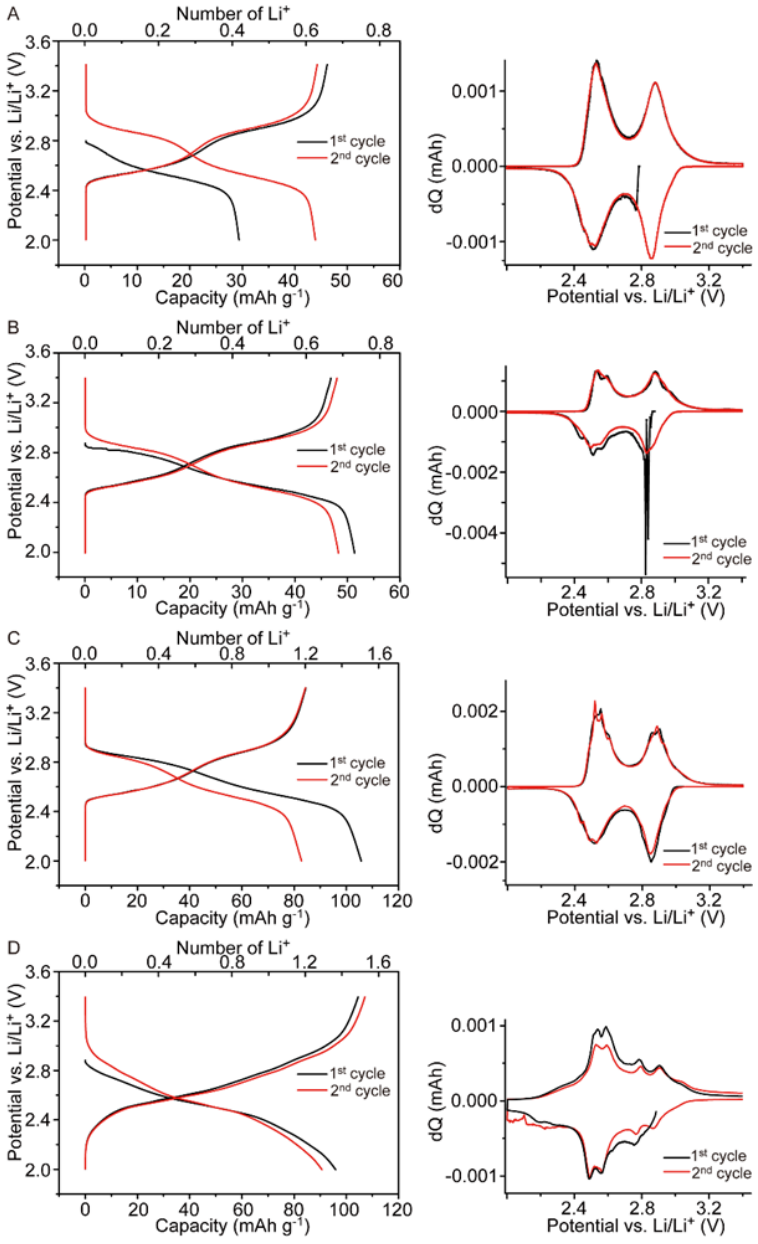

Figure 4. 5 Potentiodynamic cycling results of first two cycles in Li-cell. Voltage profiles (left) and differential charge plots (right) for (A) as-made HTPS, (B) 500-HTPS, (C) BM-HTPS, and (D) C-HTPS.

4.3.2.1 HTPS

To evaluate the potential-dependent redox behavior of HTPS, potentiodynamic cycling was performed on the composite electrodes in Li half-cells. The voltage profile of the as-synthesized HTPS showed an open circuit of 2.78 V vs. Li^+/Li and a capacity of 29 mAh/g in the first discharge (**Fig. 4.5A, left**), which corresponds to insertion of 0.41 Li^+ per HTPS f.u. The first charge capacity was 46 mAh g^{-1} and all subsequent discharge and charge capacities were around 45 mAh/g, corresponding to reversible cycling of 0.65 Li^+ into the structure.

The differential charge (dQ) plot (**Fig. 4.5A, right**) showed a reduction peak at 2.52 V vs. Li/Li^+ in the first cycle, and two oxidation peaks at 2.53 V and 2.88 V. In the second cycle, two distinct redox processes, appearing as two peaks at 2.5 V and 2.85 V, were clearly distinguished on both reduction and oxidation. These two redox processes are roughly correlated to the two sloped regions observed in the voltage profiles from 3.4 – 2.7 and 2.7 – 2.0 V and are attributed to Li^+ occupation in the M1 and M2 sites, respectively.

According to studies on hydrogen substituted zirconium phosphate NASICON-type compounds, H_3O^+ can occupy the 6*b* sites[156,157], which are the same sites occupied by Li^+ in LTP[154]. Hence, the presence of water inside the as-prepared HTPS may account for the low discharge capacity observed in the first cycle. If the H_3O^+ ions blocked the Li^+ insertion pathways into the M1 sites, this could explain why only one reduction peak corresponding to Li^+ insertion into the M2 sites (at 2.5 V) was observed in the first discharge. During charging, however, the H_3O^+ and Li^+ could both be removed and lead to the first charge capacity being higher than the discharge (**Fig. 4.5A**). To confirm this, charging was first

performed on the HTPS electrode followed by characterization with XRD (**Fig. 4.6A**). The first charge capacity was about 10 mAh g^{-1}, corresponding to removal of 0.145 H_3O^+ per f.u. and the oxidation peak was observed at about 2.9 V in the differential charge plot (**Fig. 4.6B**), which suggests the involvement of the M1 sites. The XRD patterns of the as-made HTPS and charged HTPS looked very similar, indicating that the structure did not change after charging to 3.4 V (**Fig. 4.6C**).

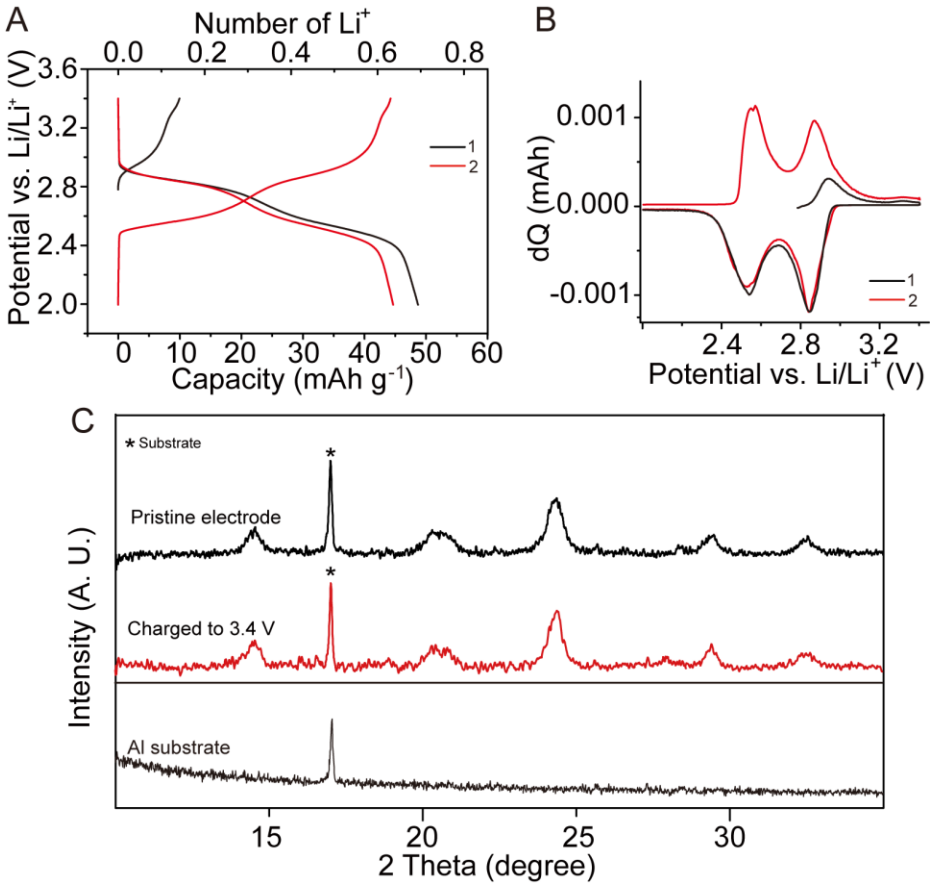

Figure 4. 6 Potentiodynamic cycling results of as-made HTPS in Li-cell, showing first two cycles when the electrode was charged (oxidized) first; (A) Voltage profiles, (B) differential charge plots . (C) PXRD patterns of as-made HTPS pristine electrode, after

as-made HTPS was charged to 3.4 V and the diffractions of the Al substrate, marked with * in the HTPS patterns.

4.3.2.2 500-HTPS

TGA studies on HTPS showed that significant weight loss did not occur until >800 ^{o}C (**Fig. 4.7A**). Our previous studies showed that HTPS calcined at 400 - 700 ^{o}C all displayed PXRD reflections that could be assigned to the rhombohedral NASICON-type structure without any secondary phases; after calcination at 750 ^{o}C, small reflections attributed to TiP_2O_7 and $Ti_5P_4O_{20}$ phases appeared but the sample was still predominately HTPS[153]. The TGA measurements also showed that the mass of as-prepared HTPS gradually increased after exposure to air. **Figure 4.7B** shows that after the HTPS was calcined at 500 ^{o}C, a small increase in weight was observed while the sample was cooling to room temperature, which is attributed to moisture being incorporated into the structure through exposure to the ambient environment. Thus the sample referred to as 500-HTPS was prepared by calcining the HTPS at 500 °C for 8 h under Ar to remove all of the moisture, then quickly transferring it to the glovebox for assembly into the Li half-cells.

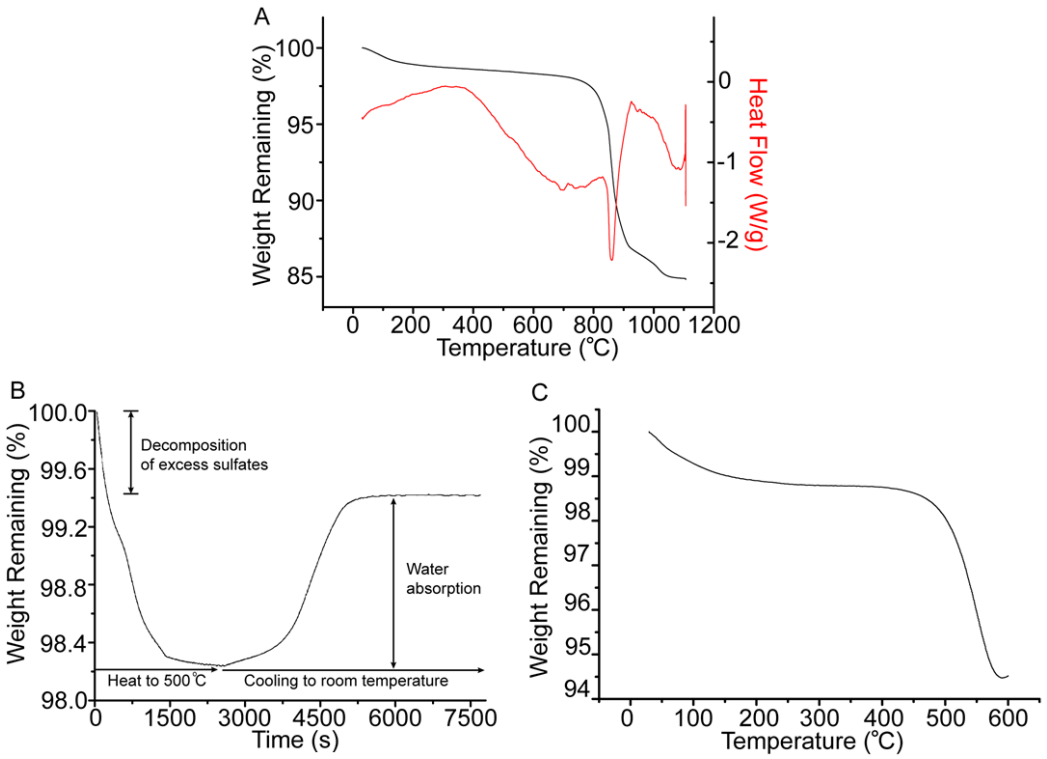

Figure 4. 7 TGA of HTPS (A) weight change of as-prepared HTPS during heating, (B) weight change of as-prepared HTPS during heating to 500°C and exposure to ambient atmosphere, (C) weight change of as-prepared C-HTPS during heating.

For 500-HTPS electrodes, the open circuit voltage increased to 2.85 V (**Fig. 4.5B**), and the capacity of the first discharge increased to 51 mAh/g, corresponding to 0.72 Li^+ inserted per formula unit. The capacity between 2.78 – 2.85 V was about 12 mAh/g, which indicates that the increase in the first discharge capacity of 500-HTPS after calcination was partially due to the higher open circuit voltage and recovery of Li^+ insertion at the higher potential redox process, as verified by the dQ plot (**Fig. 4.5B**). Based on these results, it is highly likely that water was present in the structure as H_3O^+ in the ion channel (**Fig. 4.1B**) and blocked the Li^+ diffusion pathways to the M1 sites. Hence, the capacity in the higher

cell voltage region associated with the insertion of Li^+ into the M1 sites was not observed during the first discharge. However, for the calcined 500-HTPS, the water was removed leaving the M1-M2-M1 channels empty and enabling insertion of Li^+ at around 2.83 V.

Notably, the observed features for HTPS in the dQ plots are different from those observed in LTP, despite the structural similarities of the compounds. First, the two different redox peaks in the dQ plots representing the high and low voltage Li^+ insertion processes are similar to the two separate lithiation processes that occur in Mn-NASICON compounds, where Mn^{2+} partially occupies the M1 site[140,158]. For example, the insertion of Li^+ into the initially half empty M1 sites in $Mn_{0.5}Ti_2(PO_4)_3$ was attributed to a potential plateau at 2.8 – 3.0 V; when the $Li_{0.5}Mn_{0.5}Ti_2(PO_4)_3$ composition was exceeded, the additional Li^+ were intercalated into the M2 cavity in the voltage range of 2.5 – 2.2 V. This supports the assumption that the protons in HTPS occupy the M1 site, and that Li^+ insertion into HTPS is due to subsequent filling of M1 and M2 sites[140], not a cooperative migration of Li^+ from the M1 to M2 sites through a two-phase reaction as for LTP[154]. In other words, the redox peak at ~ 2.8 V in HTPS is due to Li^+ insertion into the M1 sites, and the process at ~ 2.5 V is from lithiation of the M2 cavity. Secondly, the potentials for HTPS are higher than those observed for LTP, where the average potential is located around 2.4 – 2.5 V vs. Li^+/Li[159]; this could be due to the presence of the sulfate groups, which can increase the reaction potential due to the induction effect[151].

4.3.2.3 BM-HTPS

Since the observed capacities in the potentiodynamic cycling data for the as-prepared HTPS and 500-HTPS were much lower compared to the theoretical capacity for HTPS (which could be a result of the low electronic conductivity within the as-prepared HTPS

electrode and need for long relaxation time for the Li^+ diffusion processes) the particle size of the as-made HTPS was decreased using ball milling (BM-HTPS). **Figure 4.5C** showed that BM-HTPS had an even higher open circuit voltage around 3.15 V, and the capacity of the first discharge was 106 mAh/g, corresponding to insertion of 1.51 Li^+ per f.u. The dQ plot showed similar reduction and oxidation peaks as those observed in the as-made HTPS.

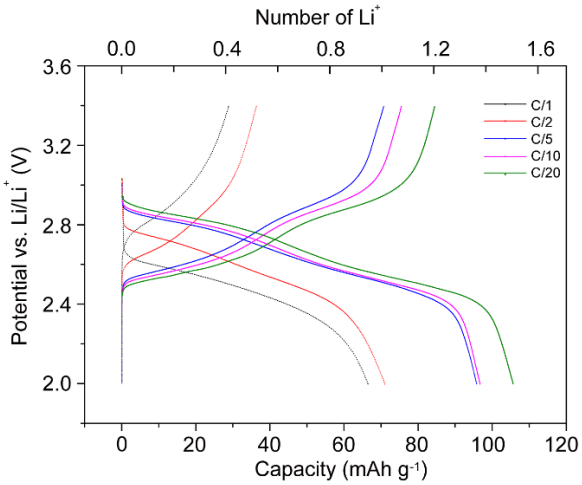

Figure 4. 8 Voltage profiles for the first discharge and charge cycles of BM-HTPS obtained under different C-rates.

4.3.2.4 C-HTPS

Although ball-milling was effective for increasing the specific capacity of HTPS, galvanostatic cycling at increasingly higher rates to 1C showed a decrease in capacity to as low as 30 mAh/g (**Fig. 4.8**), indicating that there were still significant kinetic limitations in BM-HTPS. To improve the electronic conductivity of HTPS, the particles were prepared as composites with conducting carbon (C-HTPS) using an *in-situ* synthesis method that entailed the addition of *d*-glucose to the reagents during the synthesis, and pyrolyzing the

resulting solid under Ar at 650 °C to promote carbonization. According to the TGA performed on the obtained C-HTPS (**Fig. 4.7C**), the carbon content in the synthesized composite was about 4 wt%. A first discharge capacity of 96 mAh/g was observed for C-HTPS (**Fig. 4.5D**), which is almost twice the discharge capacity observed for calcined 500-HTPS; a higher charge capacity of 105 mAh/g was also observed. The first charge capacity of C-HTPS was also larger than the discharge capacity; this observation may due to the existence of O-C=O functional groups in the carbon, as confirmed by XPS (**Fig. 4.9**), which can become oxidized during charging and create additional capacity.

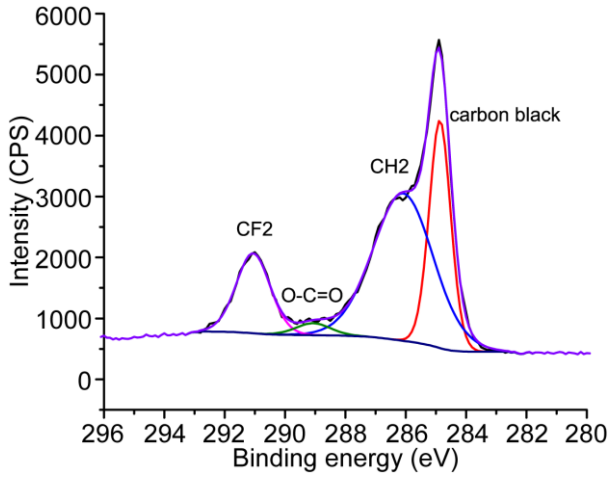

Figure 4. 9 High resolution XPS spectrum for C 1s peak from C-HTPS pristine electrode. The CF_2 and CH_2 are from the PVDF binder.

4.3.2.5 Electrochemical Impedance Spectroscopy

The improved electronic conductivity of C-HTPS was confirmed by analyzing the Nyquist plots obtained from EIS measurements (**Fig. 4.10**). Compared to BM-HTPS, the contact resistance/SEI resistance and charge transfer resistance[160,161] were smaller,

confirming that the *in-situ* carbon composite method was effective for improving the electronic properties of the HTPS electrodes.

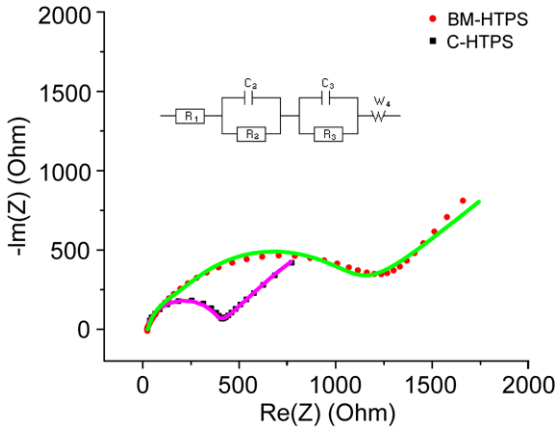

Sample	R_1 (Ω)	R_2 (Ω)	R_3 (Ω)
BM-HTPS	26.14	155	767.8
C-HTPS	27.22	141.4	341.7

Figure 4. 10 Measured Nyquist plots of BM-HTPS and C-HTPS under fully charged conditions and the calculated values (shown by the line) with the equivalent circuit shown in the figure. The impedance parameters derived using this model are shown in the table with R1 attributed to the Ohmic resistance, R2 attributed to the contact resistance including the Li^+ migration resistance through the SEI film formed on the cathode surface, the R3 represents the charge-transfer reaction resistance in the cathode-electrolyte interface.

4.3.2.6 Galvanostatic Intermittent Titration

Further galvanostatic measurements were performed on the BM-HTPS and C-HTPS samples. GITT measurements for BM-HTPS are shown in **Figure 4.11A**. The results show insertion of a total of 2 Li^+ between 3 – 1.7 V vs. Li/Li^+ corresponding to the theoretical capacity, with approximately 0.6 Li^+ inserted in the high voltage sloped region between 3.0 – 2.6 V. During charging, only 1.5 Li^+ were extracted, indicating some irreversibility. Galvanostatic cycling using a C/20 rate showed a first discharge capacity of 148 mAh/g

and charge capacity of 105 mAh/g (Coulombic efficiency of 71%) over the voltage rage of 1.5 – 3.5 V (**Fig. 4.11B**). However, the capacity retention was not well maintained. When the lower voltage cutoff was increased to 2 V (**Fig. 4.11C**), the capacity remained around 100 mAh/g with improved retention and Coulombic efficiency during cycling (**Fig. 4.11D**). The capacity retention of C-HTPS under galvanostatic cycling (**Fig. 4.12**) was not greatly improved, not even with ball-milling (**Fig. 4.12).** The large polarization observed in the GITT data, particularly below 2.2 V, is also observed in other NASICON materials[140,158] at high degrees of lithiation and may be due to intrinsic kinetic limitations in Li^+ diffusion into the structure. These results suggest that ball-milling or *in-situ* carbon composite formation can lead to only limited improvements, and other strategies such as careful morphology-control and nanostructure design may be beneficial for obtaining better capacity retention in HTPS.

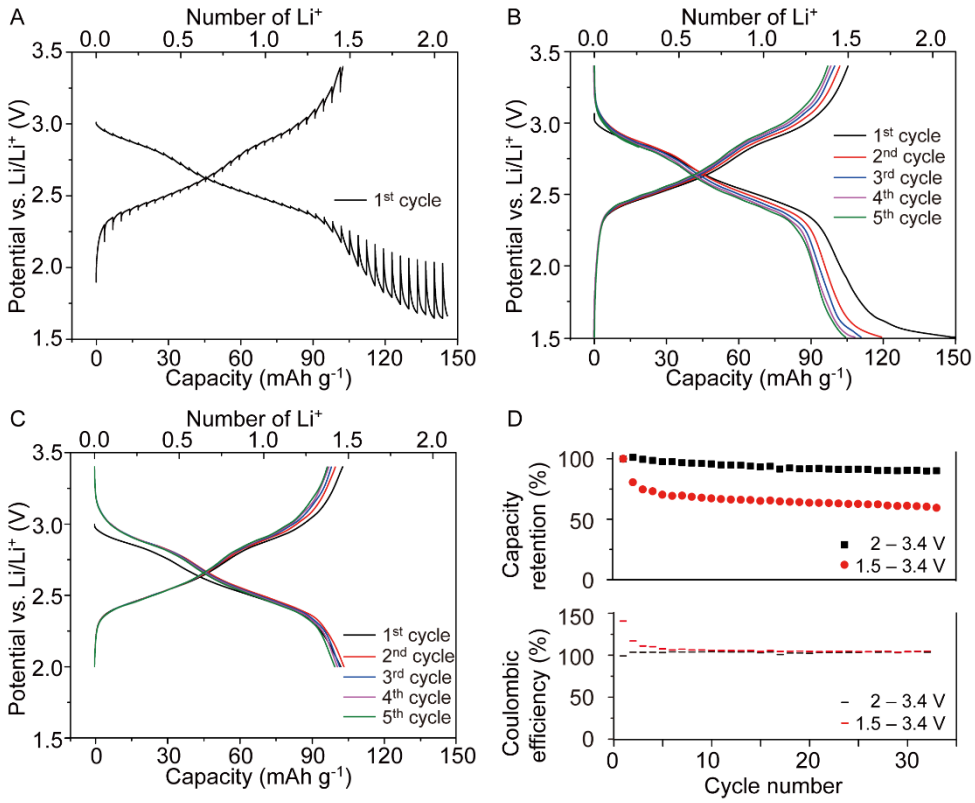

Figure 4. 11 Galvanostatic cycling results for ball-milled HTPS in Li-cell (A) GITT between 1.5 – 3.4 V for the first cycle; Voltage profiles of first 5 cycles at C/20 rate between (B) 1.5 – 3.4 V and (C) 2 – 3.4 V; (D) Capacity vs. cycle life for both potential ranges.

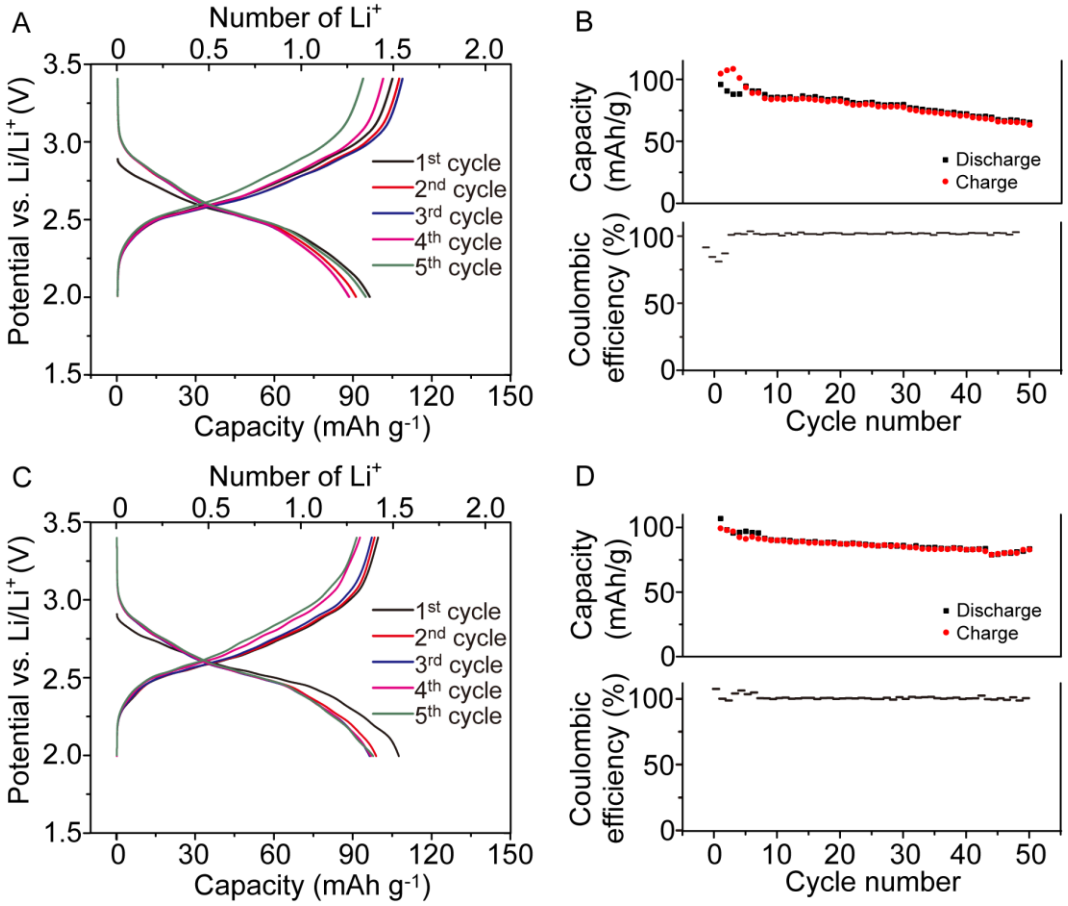

Figure 4. 12 Galvanostatic cycling results between 2 – 3.4 V for (A),(B) C-HTPS and (C),(D) ball-milled C-HTPS.

4.3.3 Structural Characterization during Electrochemical Reaction

To further understand the lithiation mechanism into HTPS, characterization was performed using SEM, PXRD, and XPS after different stages of lithiation/delithiation.

4.3.3.1 Scanning Electron Microscopy

The SEM images of the electrodes after lithiation and delithiation were quite similar (**Fig. 4.13**), indicating there was no morphology change during the electrochemical process.

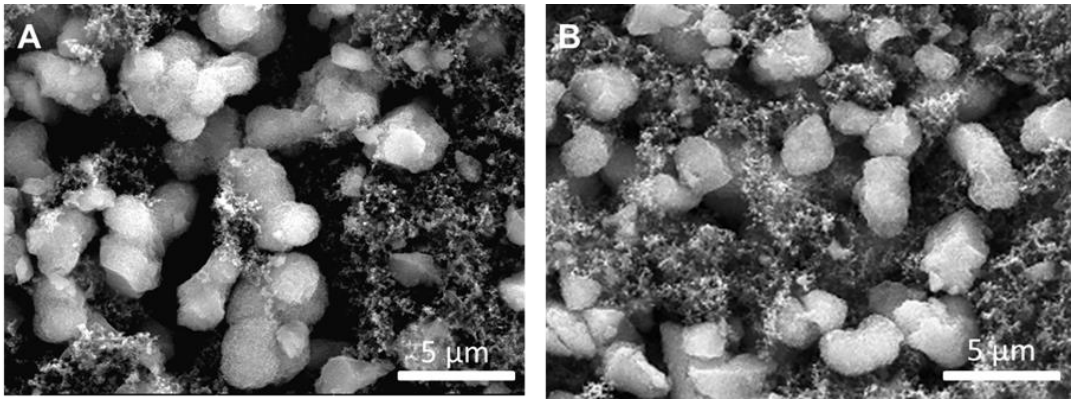

Figure 4. 13 SEM image of BM-HTPS (A) pristine electrode and (B) after lithiation/delithiation

4.3.3.2 X-ray Diffraction

To further investigate the structural changes upon electrochemical reaction, PXRD was performed on the BM-HTPS electrodes at different states of discharge and charge (**Fig. 4.14**). The peak from the Al substrate (marked with the asterisk) was used as the internal reference (**Fig. 4.6**). The PXRD pattern for the pristine electrode showed several differences after discharging to 2 V. The peak at $2\theta \sim 20.5°$ is made up of reflections from the (104) planes at 20.36° and the $(2\bar{1}0)$ planes at 20.90° (**Fig. 4.14B**). After discharge to 2 V, the intensity of the (104) peak decreased and the $(2\bar{1}0)$ peak increased (**Fig. 4.14C**); when charged back to 3.4 V, the reverse occurred (**Fig. 4.14E**).

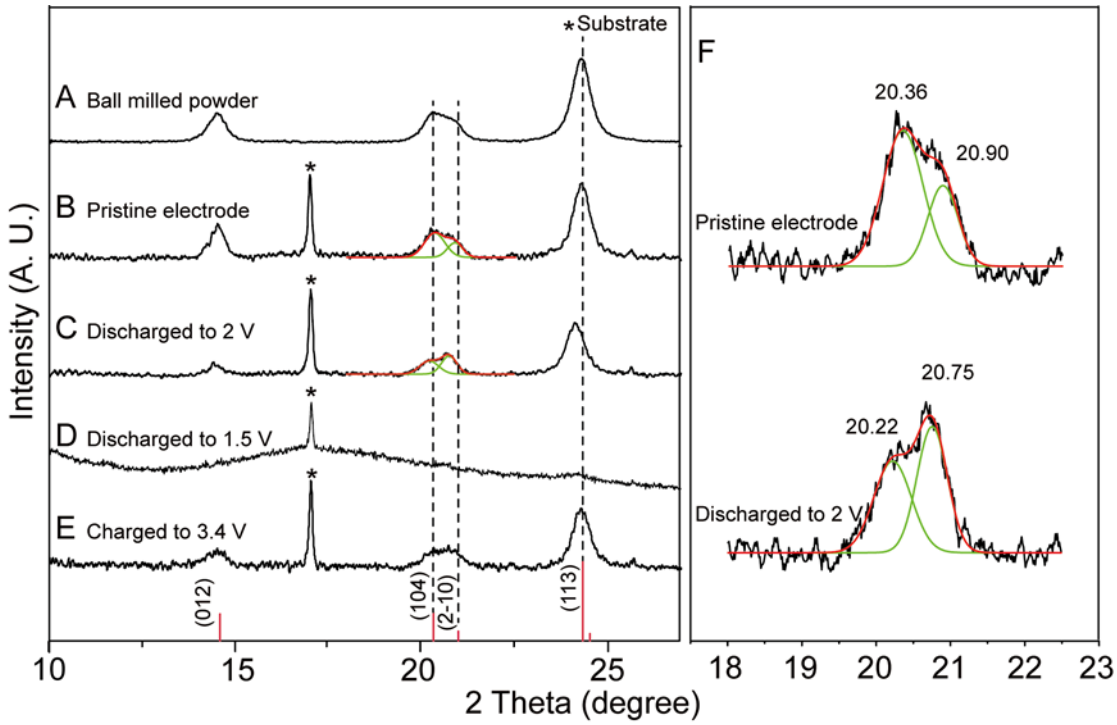

Figure 4. 14 PXRD pattern of (A) BM-HTPS powder, (B) pristine electrode prepared from BM-HTPS, (C) HTPS electrode discharged to 2 V, (D) discharged to 1.5 V, and (E) HTPS electrode discharged to 2 V and then charged to 3.4 V. The red vertical lines on the bottom are the simulated diffraction pattern of HTPS, the black dotted lines indicate the diffractions of (104) $(2\bar{1}0)$ and (113) planes of HTPS. (F) Zoom-in view on the (104) and $(2\bar{1}0)$ reflections from the pristine and lithiated electrodes.

According to our proposed lithiation mechanism, the Li^+ will first insert into the M1 sites of HTPS at 2.82 V and then into the M2 sites at around 2.5 V. When the PXRD pattern was simulated with the Li^+ ions replacing H^+ in the 6*b* sites, the intensity of the (104) reflection decreased and the $(2\bar{1}0)$ reflection increased relative to the structure with protons in the 6*b* sites, which is same with our experimental observations. Also, when comparing the PXRD patterns of the pristine and lithiated electrodes, almost all of the peaks shifted to

lower angles (**Fig. 4.14B and C**) indicating the enlargement of the unit cell, which is the same as what was observed in the Mn-NASICON compounds $Li_{0.5}Mn_{0.5}Ti_2(PO_4)_3$ and $Li_{0.5}Mn_{0.5}Ti_{1.5}Cr_{0.5}(PO_4)_3$ during lithiation[140,158]. Hence, the PXRD data support the aforementioned two-step Li^+ mechanism into HTPS.

The PXRD data also provided an explanation for why the cycling performance of HTPS was worse when the discharge voltage was decreased 1.5 V. The intensity of the crystalline peaks was strongly decreased for the sample discharged to 1.5 V (**Fig. 4.14D**), suggesting an amorphization reaction at the lower voltage and collapse of the structure, which can explain the bad capacity retention observed in the first few cycles of the cell cycled from 1.5 – 3.4 V (**Fig. 4.11B**).

4.3.3.3 X-ray Photoelectron Spectroscopy

To further analyze the electrochemical mechanism of HTPS lithiation, we performed XPS on the BM-HTPS electrodes at different states of charge. **Figure 4.15** shows the high resolution scans of the Ti 2*p* region. In the XPS spectrum for the pristine HTPS electrode **(Figure 4.15A)**, two peaks were observed at 460.2 and 466.0 eV corresponding to the Ti^{4+} binding energies for Ti $2p_{3/2}$ and $2p_{1/2}$, respectively. These peaks are shifted to higher binding energies compared to those found in TiO_2 at 458.3 and 464.0 eV[162], which is consistent with the electron withdrawing properties of the polyanions. For instance, the Ti $2p_{3/2}$ binding energies were reported at 458.4 and 459.1 eV in phosphate and sulfate-modified titania[163] and 459.8 eV in titanium pyrophosphate[164]. Since HTPS contains both phosphate and sulfate groups, the binding energy of Ti 2*p* should be even higher than these other materials, which is consistent with our observations.

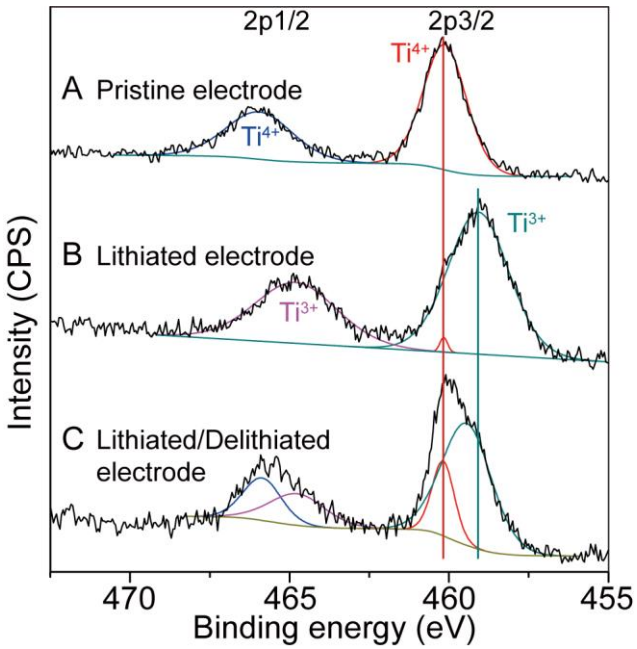

Figure 4. 15 XPS patterns of BM-HTPS (A) pristine electrode, (B) after discharge to 2 V, and (C) after discharge to 2 V and charge to 3.4 V vs. Li/Li^+. The Ti^{4+} $2p_{3/2}$ peak (red line) is at 460.2 eV and the Ti^{3+} $2p_{3/2}$ peak (green line) is at 459.1 eV.

After the electrode was lithiated to a capacity of 115 mAh/g (corresponding to insertion of 0.82 Li^+/Ti), the Ti $2p_{3/2}$ and $2p_{1/2}$ peaks shifted to lower binding energies to 459.1 and 464.8 eV, respectively (**Fig. 4.15B**), which are 1.1 and 1.2 eV lower than the binding energy for Ti^{4+}, consistent with the formation of Ti^{3+}[20,165]. Deconvolution of the Ti $2p_{3/2}$ peak revealed peaks at 460.2 eV and 459.1 eV, the former of which is attributed to unreacted Ti^{4+} since the HTPS was not fully reduced (only 82% of the theoretical capacity was observed in this sample). **Figure 4.15C** shows the XPS spectrum for an electrode that underwent a full lithiation/delithiation cycle, with the discharge capacity of 107 mAh/g (insertion of 0.76 Li^+/Ti) and charge capacity of 83 mAh/g (extraction of 0.59 Li^+/Ti). The presence of both Ti^{4+} and Ti^{3+} in the spectrum is consistent with the measured capacities

and Coulombic efficiency of only 78%. These XPS measurements confirm that the Ti^{4+}/Ti^{3+} redox couple is electrochemically active and is correlated with the lithiation/delithiation processes.

4.3.4 Na Intercalation

The electrochemical properties of HTPS in Na-cells were also evaluated, using BM-HTPS because this sample displayed the best performance in the Li-cells.

4.3.4.1 Galvanostatic/Potentiodynamic Measurements

Similar to Li^+ insertion, Na^+ insertion was observed to occur over two potential regions, between 3.1 – 2.7 V and 2.7 – 1.8 V vs. Na/Na^+ (**Fig.4.16A**). The reaction in the lower potential region is attributed to Na^+ insertion in the M2 cavities, which is similar to what has been observed in $NaTi_2(PO_4)_3$[166,167], while the reaction at the higher potentials is likely due to Na^+ insertion into the M1 sites. However, as verified by the dQ plot (**Fig. 4.16B**), the amount of charge associated with Na^+ insertion in the higher potential region was much lower than what was observed for Li^+ insertion. This is likely due to the larger size of the Na^+ compared to Li^+ with respect to the size of the M1 cavity. Long-term cycling of HTPS in the Na-cell showed stable discharge capacities around 90 mAh/g (**Fig. 4.17A**), but the charge capacities were higher than expected, particularly in the first cycle.

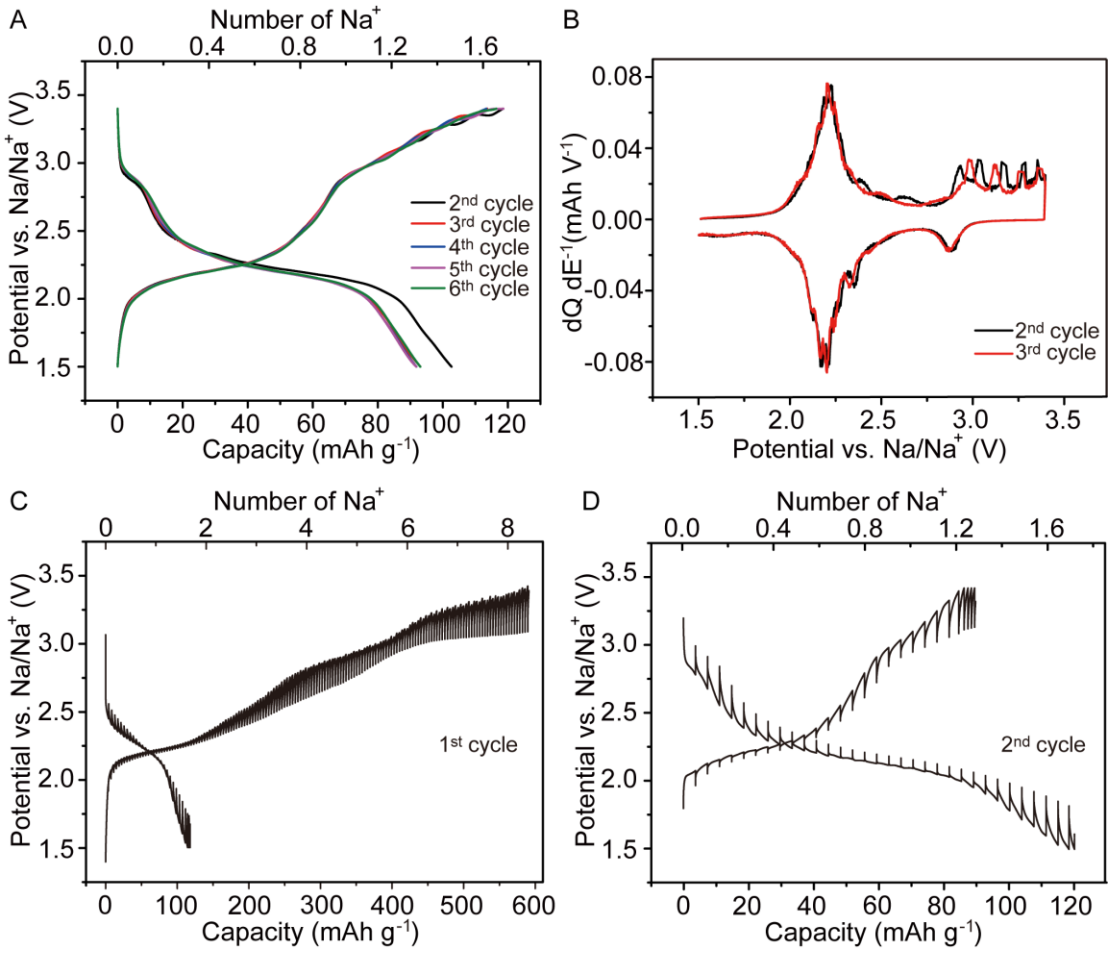

Figure 4. 16 Galvanostatic cycling results for ball-milled HTPS in Na-cell (A) Voltage profile from 1.5 – 3.4 V using C/20 rate; (B) differential charge plot; (C) First and (D) second cycle from GITT measurement.

The first galvanostatic cycle showed a higher charge capacity compared to the discharge, which is attributed to a side reaction observed during charging above 3 V vs. Na/Na^+ (**Fig. 4.17B**). This additional charge capacity was also observed in subsequent cycles, as shown in **Figure 4.16**. Control tests on electrodes only containing carbon black (90 wt%) and binder showed similar charge features above 3 V (**Fig. 4.17C**), suggesting that the extra capacity was due to side reactions with the carbon. The capacity associated

with these side reactions decreased as the cycle number continued, with only ca. 50.9 mAh/g capacity observed at the 5th (**Fig. 4.17C, inset**), suggesting that the carbon becomes passivated or that the reaction is not reversible, the Coulombic efficiency was shown in **Figure 4.17D**, the value for the first cycle was below 1%, but increased by 58 times after 10 cycles. For the HTPS electrode, however, the Coulombic efficiency (**Fig. 4.17A**) was rather low until the 30th cycle, indicating that the passivation of the carbon is less complete when the side reaction occurs in parallel with the HTPS de-sodiation.

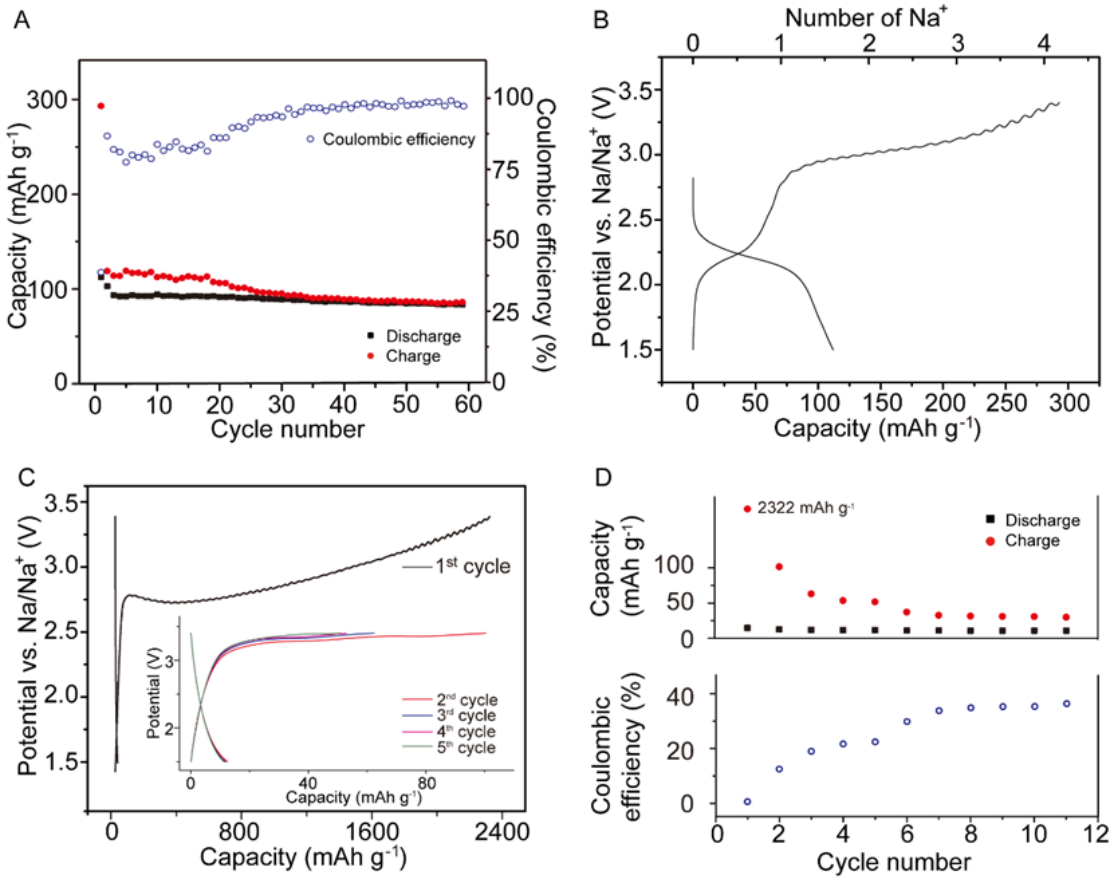

Figure 4. 17 Na-ion cell data (A) Capacity vs. cycle number and coulombic efficiency of HTPS for cycle 1 -60. (B) Galvanostatic first discharge/charge profiles of HTPS over the

voltage range of 1.5 – 3.4; (C) Galvanaostatic first discharge/charge voltage profile of electrode without HTPS (90% carbon black with 10% PVDF), inserted is the voltage profile of cycle . (D) Capacity vs. cycle number and coulombic efficiency without HTPS, showing cycles 1 - 11. All data were obtained using a current density of 7 mA/g.

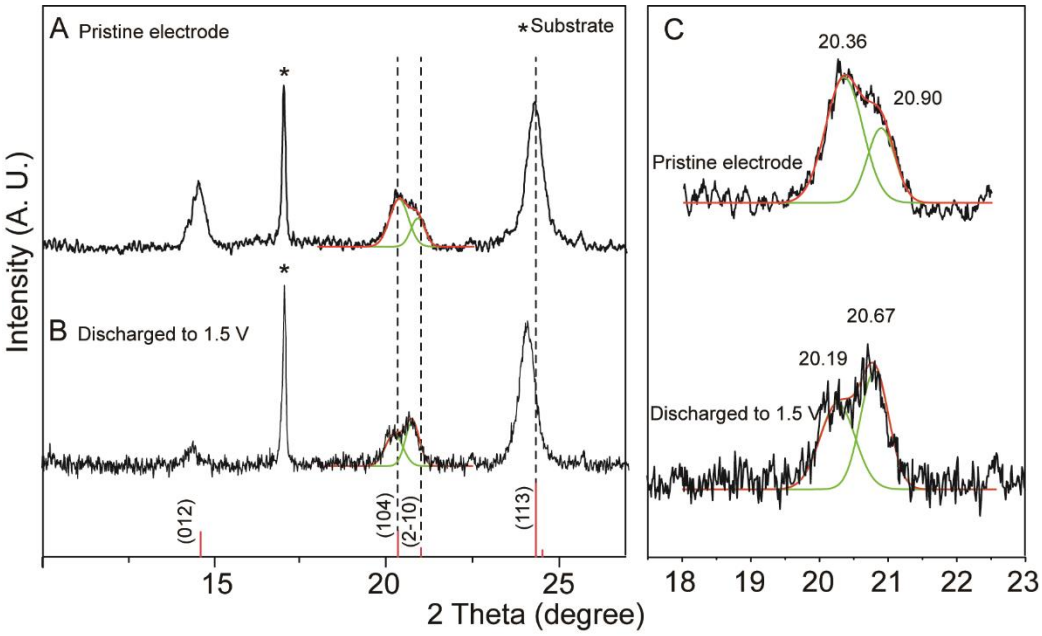

Figure 4. 18 PXRD pattern of (A) pristine electrode prepared from BM-HTPS, (B) HTPS electrode discharged to 1.5 V in a Na cell, the red vertical lines on the bottom are the simulated diffraction pattern of HTPS, the black dotted lines indicate the diffractions of (104) $(2\bar{1}0)$ and (113) planes. (C) Zoom-in view on the (104) and $(2\bar{1}0)$ reflections from the pristine and sodiated electrodes.

The PXRD patterns for the pristine and sodiated electrodes (**Fig. 4.18A, B**) showed similar trends with the electrodes in Li cells. After discharging to 1.5 V, the intensity of the (104) peak decreased and the $(2\bar{1}0)$ peak increased (**Fig. 4.18C**), indicating that the Na^+

inserted into the M1 sites. Also, when comparing the PXRD patterns of the pristine and sodiated electrodes, almost all of the peaks shifted to lower angles (**Fig. 4.18A and B**) indicating the enlargement of the unit cell, which is the same as what was observed in the Li cell. Note that, the shifts of the (104) and $(2\bar{1}0)$ reflections in the sodiated electrode (0.17 and 0.23 degrees) were bigger than those in the lithiated electrode (0.14 and 0.15 degrees), which is reasonable as the Na ions are larger than Li ions. Hence, the PXRD data of the sodiated electrode also support the aforementioned two-step reaction mechanism.

4.3.4.2 Galvanostatic Intermittent Titration

Similar to the case in the Li-cell, higher degrees of sodiation in HTPS could be observed in the GITT measurements. The GITT results also showed a very large capacity of 580 mAh/g in the first charge attributed to the side reaction (**Fig. 4.16C**) that was not a large contribution of the GITT profile in the second cycle, which displayed a charge capacity of about 90 mAh/g (**Fig. 4.16D**). The second discharge capacity of HTPS in the Na-cell was about 120 mAh/g, corresponding to 1.71 Na^+ inserted per f.u.(**Fig.4.16D**), which is higher than the discharge capacity observed for the second galvanostatic cycle of 103 mAh/g (**Fig. 4.16A**) due to kinetic limitations.

To study the difference in kinetics for the lithiation and sodiation reactions in HTPS, the GITT data were further analyzed to determine the kinetic parameters of mixed conductors [59]. **Figure 4.18A** shows an example potential vs. time (*E* vs. *t*) profile for a single titration, illustrating how the parameters required for the diffusion calculation were determined from the plot. The *E* vs. $t^{1/2}$ plots for both Li and Na-cells were linear behavior over the entire period of applied current (**Fig. 4.18B**), so equation (2) was used to calculate the diffusion coefficient as a function of guest species inserted/extracted per f.u. of HTPS

(**Figure 4.18C,D**). During discharging, the values of D_{Li} in HTPS were in the range of 1.04×10^{-11} to 8.01×10^{-10} cm^2 s^{-1}, while the D_{Na} ranged from 1.27×10^{-11} to 2.98×10^{-10} cm^2 s^{-1}. During charging, D_{Li} ranged from 4.86×10^{-11} to 6.26×10^{-10} cm^2 s^{-1} and D_{Na} from 1.27×10^{-12} to 4.54×10^{-10} cm^2 s^{-1}. During both lithiation and delithiation, the D_{Li} values dropped to ~10^{-11} cm^2 s^{-1} when more than 1.5 Li^+ were inside the HTPS, which is attributed to the difference in the M1 and M2 site reactions. In comparison, the values of D_{Li} in LTP varied over a wide range, from 8.46×10^{-14} cm^2 s^{-1} to 2.15×10^{-9} cm^2 s^{-1}, with the minimum value occurring at the middle of the two-phase transition of LTP [168]. The diffusion coefficients for HTPS did not vary as much as those for LTP during the lithiation (sodiation)/delithation (desodiation) processes, which is attributed to the different mechanism of ion insertion in HTPS vs. LTP. The D_{Li} values for HTPS are comparable to intercalation electrode materials such as $Li(Ni_{1/3}Co_{1/3}Mn_{1/3})O_2$ (~3×10^{-10} cm^2 s^{-1})[169] and higher than those in $LiFePO_4$ (1.8×10^{-14} cm^2 s^{-1})[170].

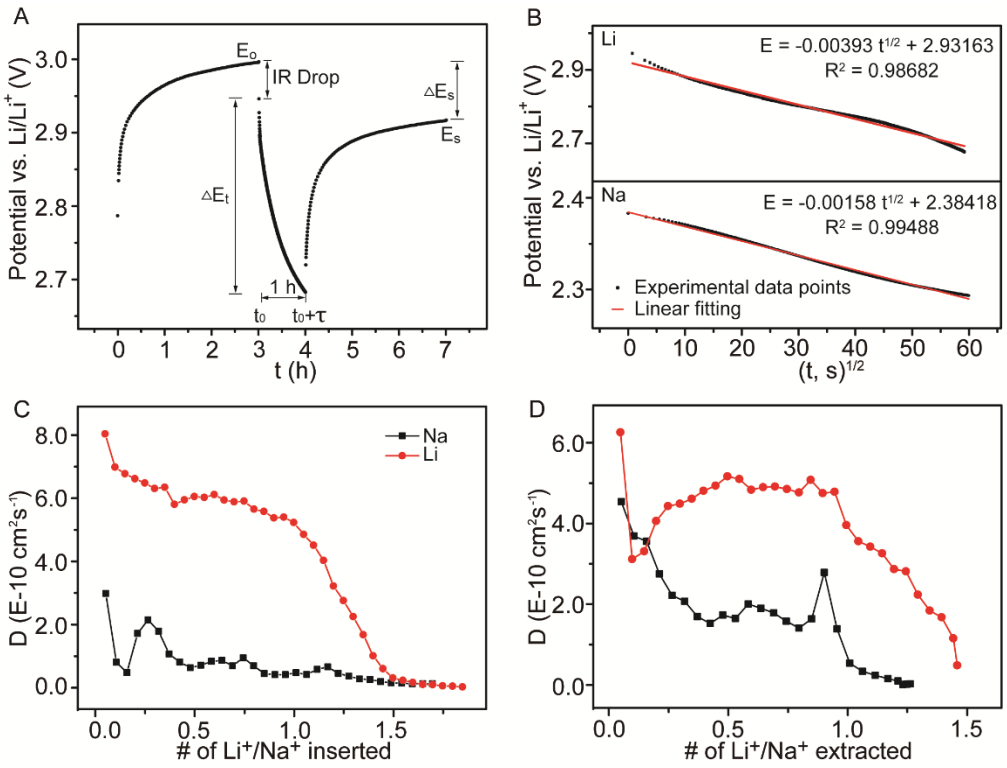

Figure 4. 19 (A) Potential vs. time plot of ball-milled HTPS electrode in Na-cell for a single GITT titration during discharge, E0 is the steady-state voltage of previous titration, Es is the steady-state voltage of this step, ΔE_s is the change in the steady-state voltage over the titration step and ΔE_t is the voltage change for a current flux for the time τ, neglecting the IR drop; (B) linear behavior of the E vs. $t^{1/2}$ relationship of Li cell and Na cell; (C)-(D) Chemical diffusion coefficient of Li^+ and Na^+ ions in HTPS as fuction of guest species inserted per HTPS formula unit, vs. the number of guest species (C) inserted during discharging (D) extracted during charging after a fully discharge per formula unit.

4.4 Conclusion

Herein we establish the properties of hydrogen titanium phosphate sulfate, $H_{0.4}Ti_2(PO_4)_{2.4}(SO_4)_{0.6}$ (HTPS), for electrochemical Li^+ and Na^+ insertion. Ball-milling and preparation with carbon composites using an *in-situ* reaction with glucose were also performed to decrease the particle size and increase the conductivity, respectively. A capacity of 148 mAh/g was observed in the ball-milled HTPS in the Li half-cell and 103 mAh/g in the Na half-cell. The insertion of cations occurred in two voltage ranges, at 2.83 and 2.53 V vs. Li/Li^+ and at 2.87 and 2.20 vs. Na/Na^+, corresponding to the filling of the M1 and M2 sites, respectively. Future work on the synthesis of pre-lithiated and pre-sodiated materials, decreasing the particle size, and optimizing the carbon composites to improve the electronic conductivity of the composite would be advantageous for further development of HTPS as a cathode for Li- and Na-ion batteries.

5: ELECTROCHEMICAL PROPERTIES OF SILICON CLATHRATE

5.1 Introduction

Clathrates [171] are known for their unique structures and potential as superconducting [172–180], thermoelectric[181–187], magnetic[188,189], hydrogen storage[190,191], and hard materials[192]. Type I clathrates of the form M_xSi_{46} (where M is the guest ion, e.g. Ba), are made from two pentagonal dodecahedra (Si_{20}) plus six tetrakaidecahedra (Si_{24}) per unit cell (**Fig. 5.1**). Framework substitution, whereby some of the Si atoms are substituted with another element, is also common in clathrates. Example type I ternary clathrates that have been studied are of the form $Ba_8X_\delta Si_{46-\delta}$ where X = Al, Ga, Zn, Cu, Ni, etc.[193–195] Such substituents stabilize the clathrate structure by fulfilling the Zintl concept and modifying the density of states at the Fermi level, which can affect the transport properties[195]. The Zintl condition is obtained when the more electropositive 'guest' atoms donate valence electrons to the more electronegative host or cage and each element achieves a closed shell state[196], for instance, in $Ba_8Al_{16}Si_{30}$.

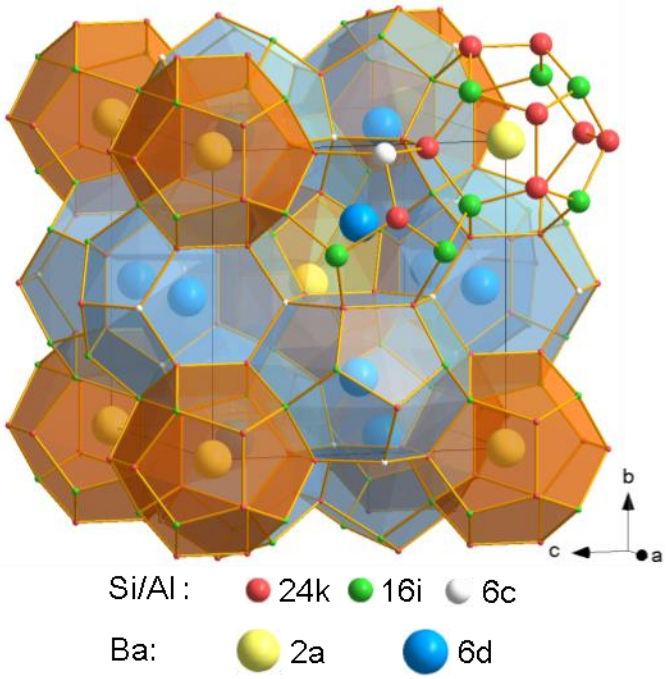

Figure 5. 1 Combined Ball and stick/polyhedral illustration of type I $Ba_8Al_{16}Si_{30}$ clathrate.

Recently, there has been much interest in the electrochemical properties of clathrates and their potential for applications in batteries[197]. Considering the possible sites that Li could occupy inside the clathrate structure, the insides of the Si_{20} and Si_{24} cavities are potential candidates, in addition to vacancy sites on the Si framework. Previous first principles density functional theory studies (DFT) showed that Li insertion into Si framework vacancies or Ba guest atom vacancies in the Si_{20} cages could stabilize the clathrate structure, and that multiple Li atoms can fit inside the Si_{24} cages[198,199]. Moreover, it is suggested that clathrates can form stable structures containing framework vacancies in order to meet the Zintl condition (e.g., $Ba_8Al_xSi_{42-(3/4)x}\square_{4-(1/4)x}$, $Ba_8Ge_{43}\square_3$ and $Cs_8Sn_{44}\square_2$, where $\square$ = vacancy)[183,184,191,200–202].

In our group's previous work[197], ternary type I clathrates based on $Ba_8Al_\delta Si_{46-\delta}$ (δ=8，10，12) were found to display voltage-dependent redox characteristics distinct from those observed in diamond cubic Si, amorphous Si, and other SiO. Moreover, no discernable changes in the local bonding and crystalline structure of the type I clathrates were observed by nuclear magnetic resonance (NMR) or X-ray diffraction (XRD) after lithiation. The as-prepared clathrates investigated in this previous study were off-stoichiometric and also contained some unreacted precursors and side products such as Si and $BaSi_2$. In order to remove these non-clathrate species, ball-milling followed by acid and base etching was employed. However, it is not known what role, if any, these processing steps played in the formation of additional defects in the clathrate structure, or the observed electrochemical properties of the clathrate electrodes.

Here, we performed a systematic investigation of silicon clathrates with higher Al content, $Ba_8Al_{16}Si_{30}$. This would enable the evaluation of the electrochemical properties of silicon clathrates with minimum defects such as framework vacancies. $Ba_8Al_{16}Si_{30}$ clathrate was prepared using arc melting or hot-pressing. Then, different processing steps (such as ball-milling, acid/base etching) were incrementally introduced and studied with X-ray diffraction (XRD), X-ray photoelectron spectroscopy (XPS), Raman spectroscopy, and electrochemical analysis to understand their role on the electrochemical behavior and other physicochemical features.

We find that very few Li can be electrochemically inserted into the as-made clathrate. The introduction of disorder through ball-milling resulted in higher observed specific capacities, not solely from the reduction of the particle size, but from the formation of an amorphous surface layer. The acid/base etching, while not affecting the crystallinity of the

clathrate, caused the formation of Si-O bonds on the surface and led to lower lithiation capacities. Additionally, further ball-milling can achieve high capacity again by regenerating the amorphous layer. These results show that for clathrate with high Al content and small amount of vacancies, Li insertion in the structure is unfavorable unless amorphous surface layer is introduced.

5.2 Experimental Methods

5.2.1 Synthesis of Silicon Clathrate by Arc-melting

The clathrate samples prepared by arc-melting are named with the prefix "AM". In the arc-melting preparation, metals of Ba, Si and Al were weighed with a total weight of ca. 600 mg to achieve a composition of $Ba_8Al_{16}Si_{30}$. The arc melting chamber was evacuated to vacuum for 20 min and filled with high purity argon. The metals Ba, Al and Si were melted into an ingot, which was then taken out and turned over. The melting process was repeated three times to obtain good homogeneity.

5.2.1.1 AM-1

AM-1 refers to the sample obtained after the as-made, arc-melted ingot was ground by hand using a mortar and pestle

5.2.1.2 AM-2

AM-1 refers to the sample which ball-milled for 40 min (SPEX 8000, stainless steel grinding set)

5.2.1.3 AM-3

AM-2 was suspended in de-ionized water and treated with 3 M HCl for 12 hours to remove the $BaSi_2$. After the acid treatment, the powder was recovered using vacuum filtration and washed with de-ionized water. Then, the powder was treated with 1 M NaOH for 12 hours to remove amorphous or cubic Si, then recovered using vacuum filtration and washed with de-ionized water and dried to yield AM-3.

5.2.1.4 AM-4

AM-4 was obtained by ball-milling AM-3 for 40 minutes.

5.2.1.5 AM-5

AM-5 was obtained by ball-milling AM-3 for 120 minutes.

5.2.2 Materials Characterization

Wavelength dispersive X-ray spectroscopy (WDS) was used to determine the composition. Powdered X-ray diffraction (XRD), scanning electron microscopy (SEM), X-ray photoelectron spectroscopy (XPS) and Raman spectroscopy were used to perform structural and chemical characterization of the prepared Si clathrate powders and composite electrodes before and after electrochemical cycling.

5.2.2.1 Wavelength Dispersive Spectroscopy

Wavelength dispersive X-ray spectrometer (WDS, JEOL JXA-8530Ff equipped with five wavelength-dispersive spectrometers) was used to determine the composition of the silicon clathrates. The clathrate powder was mixed with epoxy and cured for two days at room temperature in chemical hood. Then the sample was grinded and polished to a flat

surface for subsequent analysis. 10 nA current with a 20 keV accelerating potential was used for analysis, Net elemental intensities for Al and Si were determined with respect to pure elemental Si and Al calibration standards, as well as barite was used as standard to determine the net elemental intensities for Ba. Seven different locations were randomly chosen and the average analyzed for each sample.

5.2.2.2 X-ray Diffraction

For XRD, the electrodes were rinsed several times with propylene carbonate and dried in an Argon-filled glovebox overnight. XRD data were collected using a Panalytical X'pert Pro diffractometer with CuKα radiation operating at 40 kV/40 mA.

5.2.2.3 Electron Microscopy

Scanning electron microscopy (SEM) imaging was performed using an XL 30 ESEM-FEG microscope and a 12 kV electron beam. For mounting the samples, the powder samples were dispersed into ethanol with ultrasonication for five minutes and dropped to a clean Si wafer surface, the Si wafers were pasted on the SEM stubs using carbon tapes.

Transmission electron microscopy was performed using a Philips CM-200 operated at 200 kV. Powdered samples were dispersed into ethanol with ultrasonication for 5 minutes and then dropped onto a Ted Pella copper TEM grid with lacey carbon support. After all the ethanol was evaporated, the grid was loaded onto a single-tilt sample holder and taken into the microscope for examination, The samples were not covered with any conductive coatings. Images were recorded using a CCD camera and a Gatan Acquisition System.

5.2.2.4 X-ray Photoelectron Spectroscopy

XPS was performed on a VG ESCALAB 220i-XL with Al Kα anode (1486.6 eV) operating at 63 W and 12 kV. The X-ray takeoff angle was 45° and the data were acquired from the region about ~400 μm of the surface of the sample. Charge compensation was used. A pass energy of 20 eV was used for high-resolution spectra (energy resolution 0.7 eV). The spectra were calibrated to the hydrocarbon peak at 284.5 eV. Peak fitting was performed using CasaXPS processing software.

5.2.2.5 Raman Spectroscopy

The powder samples were dispersed into ethanol with ultrasonication for five minutes and dropped to a clean copper foil substrate for the Raman spectroscopy measurements. The Raman spectroscopy data were collected using a custom built Raman spectrometer in a 180 ° geometry. The sample was excited using a 150 mW Coherent Sapphire SF laser with a 532 nm laser wavelength. The laser power was controlled using a neutral density filters wheel and an initial laser power of 100 mW, and ranged from 1.3 mW to 24 mW depending on sample sensitivity. The laser was focused onto the sample using a 50X super long working distance plan APO Mitutoyo objective with a numerical aperture of 0.42. The signal was discriminated from the laser excitation using a Kaiser laser band pass filter followed by an Ondax® SureBlock™ ultra narrow-band notch filter and a Semrock edge filter. The data were collected using an Acton 300i spectrograph and a back thinned Princeton Instruments liquid nitrogen cooled CCD detector.

5.2.3 Electrochemical Measurement

The clathrate powder was prepared into slurries by mixing the clathrate sample with 10 wt% carbon black (to serve as conducting additive) and 10 wt% polyvinylidene difluoride (PVDF) (to serve as binder) in N-methyl pyrrolidone (NMP) as solvent. The slurries were stirred overnight and coated onto Cu foil current collectors using a Meyer rod, and then heated at 120 ^{o}C to remove the solvent. Pouch cells were assembled using Li metal as the counter electrode, Celgard 2500 as separator, and 1 M $LiPF_6$ (EC:DMC:DEC, 4:2:4 in volume, LBC 3051C, MTI) as electrolyte in the glovebox.

5.2.3.1 Galvanostatic Measurements

Electrochemical testing was performed using a Biologic VMP3. Galvanostatic measurements were performed from 0.01 – 2.5 V vs. Li/Li^+ range using a current density of 25 mA/g.

5.2.3.2 Galvanostatic Intermittent Titration

Galvanostatic intermittent titration (GITT) measurements were performed by charging/discharging the cells at a constant current (5 mAh g^{-1} for AM-3 and HP, 25 $mAhg^{-1}$ for AM-5) for an interval of 10 minutes followed by an open circuit stand for 40 minutes to allow the cell voltage to relax to its quasi-equilibrium state.

5.3 Results and Discussion

5.3.1 Structural Characterization

5.3.1.1 X-ray Diffraction

The XRD pattern of AM-1 matched the reflections associated with $Ba_8Al_{16}Si_{30}$ (**Fig. 5.2A**). The reference pattern used for the clathrate was $Ba_8Al_{16}Si_{30}$ PDF 00-055-0373 [193]. Additionally, some weak reflections that were not associated with the clathrate structure were observed at 2θ = 22.2, 28.4, 28.7, 29.9, and 33.3° (**Fig. 5.2B**). The reflection at 28.4 ° is likely from the (111) reflections of cubic Si, as this is commonly seen in clathrate syntheses indicating some unreacted precursor [183,203,204]. The other reflections are close to the positions of the (102), (211), (103) and (301) diffracting planes of $BaSi_2$, but the most intense reflection for the (112) planes expected at 27.3 ° was not observed in AM-1; hence it is uncertain if $BaSi_2$ is present in the sample. These other reflections could be from a compound with $BaAl_4$-type structure, as suggested in previous studies [183]. $BaAl_2Si_2$ was also identified in previous studies on $Ba_8Al_ySi_{46-y}$ clathrate [205183]; the peak at 2θ = 28.7 ° could be from the (211) plane of $BaAl_2Si_2$, but this assignment is also not unambiguous. Anno *et al* have suggested the existence of $BaAl_2O_4$ as an impurity phase [205]; the peak at 28.4 ° may be suggested to have contribution from (202) plane of that structure.. However, given how elemental Ba was stored and handled, the introduction of such a large amount of oxygen during the process is highly unlikely. We note that while the identity of the impurity phase(s) is not clear, the very weak intensity of the reflections is indicative of clathrate samples with phase purity of over 95% wt.

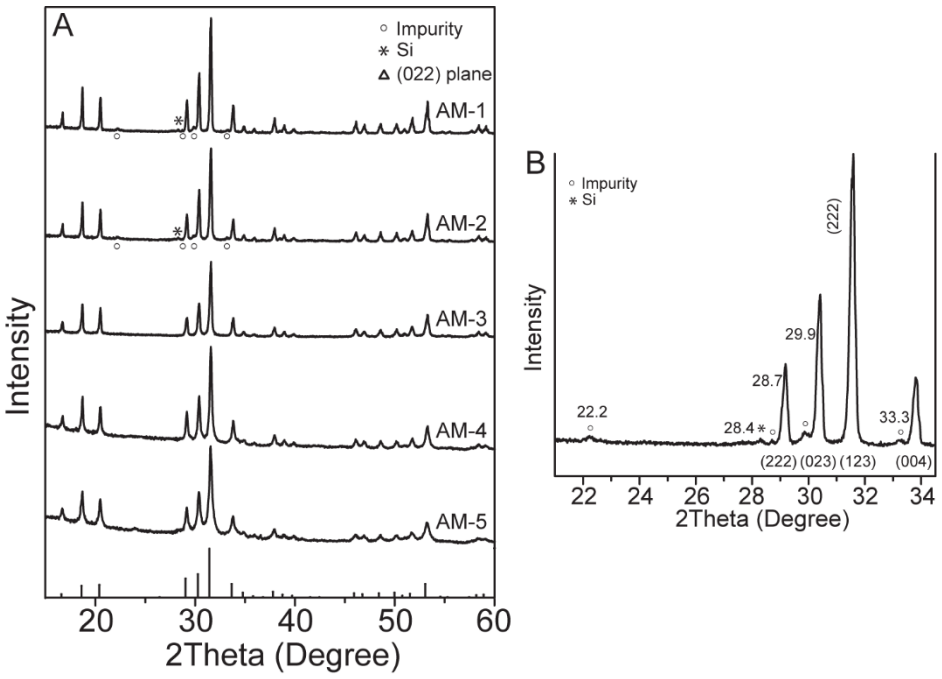

Figure 5. 2 XRD of $Ba_8Al_{16}Si_{30}$ samples prepared by (A) arc-melting, and (B) Zoomed in view from 2θ = 21 - 34.5º of the XRD pattern for AM-1. The reference pattern for $Ba_8Al_{16}Si_{30}$ (PDF 00-055-0373) is shown on the bottom for comparison.

After ball-milling of AM-1, the peak positions remained the same, but the intensities were slightly altered – weakened and broadened to a certain degree, which indicates a smaller particle size in AM-2 compared to AM-1. After acid and base treatment, the small impurity peaks disappeared, confirming the removal of these phases. The XRD pattern of AM-4, which was ball-milled for 40 minutes, had broader diffraction peaks due to the decrease in the particle size. After ball-milling for 2 hours, the peaks were even broader, and a small peak at 2θ = 24.0 º was observed, which corresponds to the (022) plane of Si clathrate.

Least-squares refinement determined that the cell parameter of the clathrate samples from AM-1 to AM-5 were 10.5888 Å, 10.5914 Å, 10.5908 Å, 10.5915 Å and 10.5935 Å (**Table 5.1**). The refinement results showed there was not a large difference in the lattice parameters of the samples, which suggests that the clathrates had a similar composition. Previous studies showed changes in lattice parameter of 0.048 Å when the Al content changed from 12.0 to 14.9 [206]. Shifts in the (2 3 1) reflection were also shown to be characteristic of differences in Al content [206], but we did not observe this in our samples, as shown in **Figure 5.3**. This is consistent the microprobe analysis results that did not show a large difference in the composition between the samples (**Table 5.1**).

Table 5. 1 Cell parameters for clathrates according to the XRD refinement and the atomic ratio of Ba, Al and Si according to microprobe analysis.

Sample	Lattice constant	Ba	Al	Si
AM-1	10.589	7.79	13.68	32.32
AM-2	10.591	8.54	13.54	32.46
AM-3	10.591	8.45	13.34	32.66
AM-4	10.592	8.46	13.43	32.57
AM-5	10.594	8.56	13.41	32.59

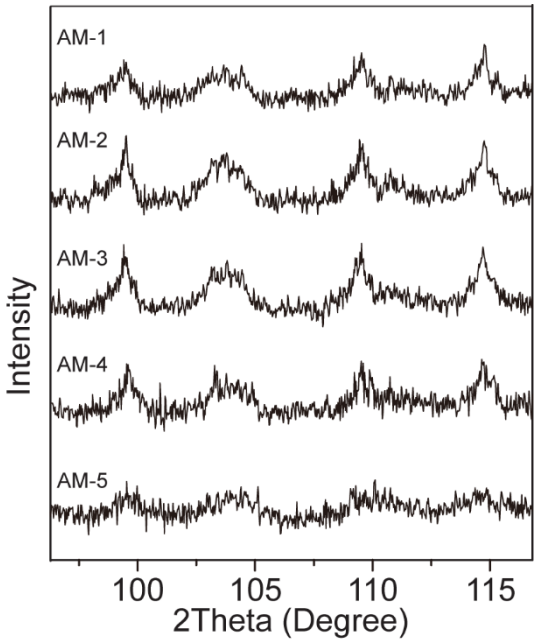

Figure 5. 3 XRD patterns for clathrates at high degree near (2 3 1) peak.

5.3.1.2 Electron Microscopy

Scanning electron microscopy (SEM) imaging was employed to determine the particle sizes of the clathrates. The SEM images of AM-1 showed particle sizes of about 1-40 μm (**Fig. 5.4A**). Some of the particles were around 2 μm in size, but the majority of the sample consisted of particles larger than 20 μm. After ball-milling for 40 minutes to form AM-2 (**Fig. 5.4B**), the particle size was reduced to less than 5 μm. When the ball-milling was followed by the acid and base treatment to make AM-3, the morphology was more uniform, with the size controlled under 2 μm (**Fig. 5.4C**). Further ball-milling for 40 minutes did not result in a large effect in changing the particles sizes (AM-4, **Fig. 5.4D**), but when the ball-milling time was increased to 120 minutes, the particle size decreased to about 1 μm (AM-5, **Fig. 5.4E**).

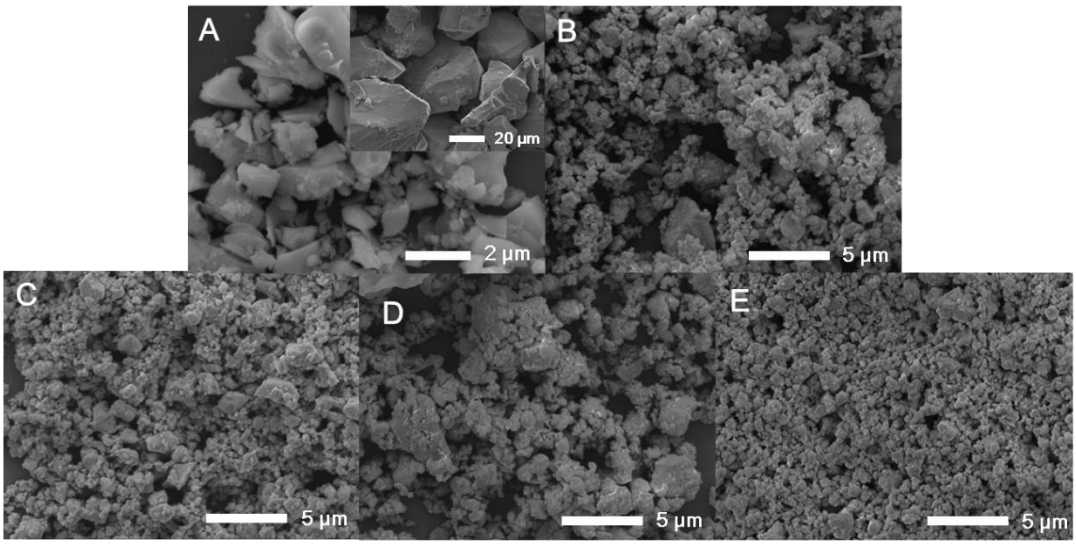

Figure 5. 4 SEM images of different prepared $Ba_8Al_{16}Si_{30}$ samples (A) AM-1; (B) AM-2; (C) AM-3; (D) AM-4; (E) AM-5.

To better understand the surface structure of different clathrate samples, transmission electron microscopy (TEM) characterization was performed (**Fig. 5.5**). Selected-area electron diffraction (SAED) was also performed assess the crystallinity of the particles. The samples were stable under the electron beam and no visible changes to the microstructure of the samples were observed during imaging. A thin amorphous layer less than 5 nm thick was observed in AM-1(**Fig. 5.5A**), and the SAED pattern showed distinct spots with little amorphous halo, indicating that the majority of the particles were crystalline. After ball-milling, the amorphous surface layer became thicker in AM-2, in some cases more than 10 nm thick (**Fig. 5.5B**). This shows that ball-milling can cause the surface of the clathrate particles to become amorphous. The TEM analysis of the sample after ball-milling and acid/base treatment, AM-3, displayed a non-uniform amorphous layer, which was in some cases only 5 nm thick (**Fig. 5.5C**). This suggests that the acid/base

treatment could have partially etched away the amorphous layer. The TEM images of AM-4 and AM-5 showed that further ball-milling introduced more amorphous surfaces. The AM-4 sample, which was ball-milled for 40 minutes, displayed an amorphous layer about 10 nm (**Fig. 5.5D**), while the sample ball-milled for 120 minutes, AM-5, showed an even thicker layer of 10-20 nm (**Fig. 5.5E**). However, the crystalline lattice fringes and electron diffraction patterns showed that the particle interiors were still crystalline, consistent with the XRD results (**Fig. 5.2**).

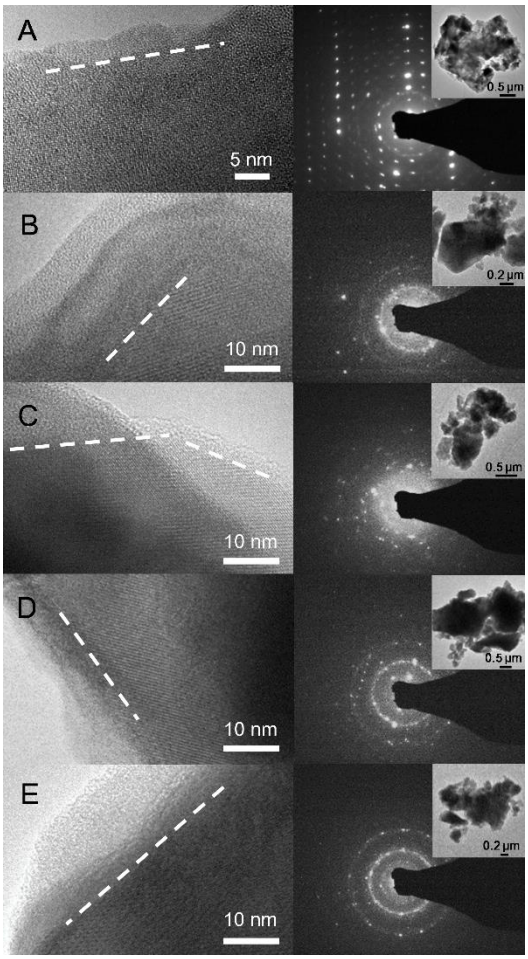

Figure 5. 5 High-magnification TEM images and selected-area electron diffraction patterns of (A) AM-1. (B) AM-2. (C) AM-3. (D) AM-4. (E) AM-5, inserted are the low-magnification TEM images. The dashed line shows the amorphous-crystalline interface.

5.3.1.3 X-ray Photoelectron Spectroscopy

XPS studies were performed to better understand the differences in chemical surface states between the different clathrate samples. As shown in **Figure 5.6**, the Ba $4d^{3/2}$ and Ba $4d^{5/2}$ peaks were observed at binding energies of 93.0 and 90.3 eV, respectively, while the Si 2*p* peak corresponding to the Si in the clathrate framework was found at 98.6 eV. Due to the interaction of the Si with Ba and Al, the binding energy of Si in the clathrate shifted

to the lower energy level compared that observed in diamond cubic Si [207]. The signal attributed to surface Si bound to oxygen was centered at approximately 102.5 eV, suggesting the presence of a notable native oxide in the as-prepared AM-1 (**Fig. 5.6A**). This is consistent with previous studies identifying a native oxide on silicon clathrate surfaces [197,208]. Comparing the spectra for AM-1 (**Fig. 5.6A**) and AM-2 (**Fig. 5.6B**), the amount of Si-O and Si-Si signals are the same, 76 % Si-O and 24 % Si-Si (**Table 5.2**), indicating that ball-milling did not affect this oxide layer. After the acid/base treatment, however, the Si-O peak intensity became stronger (**Fig. 5.6C**), 94 % of Si-O and 6% of Si-Si (**Table 5.2**). This indicates that almost all of the surface Si atoms were bonded with O, suggesting that the acid/base treatment oxidized the AM-3 clathrate surface. Additional ball-milling after the acid/base treatment resulted in an increase in the Si-Si peak intensity in AM-4 and AM-5, the Si-Si peaks increased to 17 % and 19 % (**Table 5.2**), respectively, which could be due to the exposure of fresh surfaces as the particle sizes were reduced.

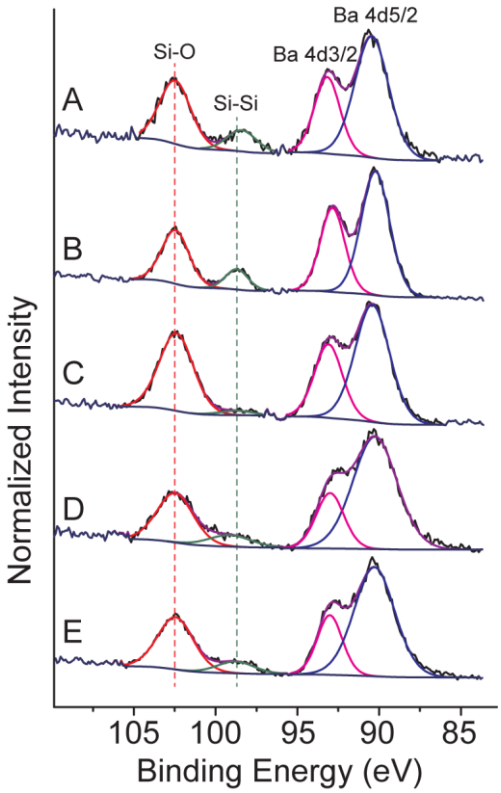

Figure 5. 6 High resolution XPS spectra of $Ba_8Al_{16}Si_{30}$ samples (A) AM-1; (B) AM-2; (C) AM-3; (D) AM-4; (E) AM-5. The green dashed line is 98.6 eV and red line is 102.5 eV.

Table 5. 2 The contribution of Si-O and Si-Si in percentage (obtained by XPS).

Sample	Si-O (%)	Si-Si (%)
AM-1	76	24
AM-2	76	24
AM-3	94	6
AM-4	83	17
AM-5	81	19

5.3.1.4 Raman

To better characterize the structure of the clathrates, Raman spectroscopy was performed. Previous studies have demonstrated that the Raman spectrum of silicon clathrates is characterized by: 1) low-frequency vibration bands associated with the rattling guest atoms, 2) a low frequency framework band, and 3) a high frequency framework band that describes how strongly the guest atoms are interacting with the framework. The high frequency framework band was observed between 430 – 461 cm^{-1} in non-framework substituted clathrates [178,209,210], e.g. at 438 cm^{-1} in Ba_8Si_{46} [178]. When Al-substitution is used, the band redshifts due to the reduced mass when replacing Al with Si. For example, this framework band was observed at 517 and 508 cm^{-1} in $Ba_{7.5}Al_{13}Si_{29}$ and $Eu_{0.27}Ba_{7.22}Al_{13}Si_{29}$, respectively [211].

The highest-frequency framework mode in our AM-1 and AM-2 samples was observed at 495 cm^{-1} (**Fig. 5.7A-B**), which is higher than the mode in the non-substituted clathrates from previous studies. This mode redshifted to 510.5 cm^{-1} in AM-3 after etching (**Fig. 5.7C**), but shifted back after further ball-milling, e.g. for AM-5 (**Fig. 5.7D**), the same trend was also found in the lowest-frequency framework vibrations around 300 cm^{-1}. From XPS analysis, the amount of Si-O bonding increased after etching, so the redshift observed in AM-3 is likely due to the formation of the oxide layer.

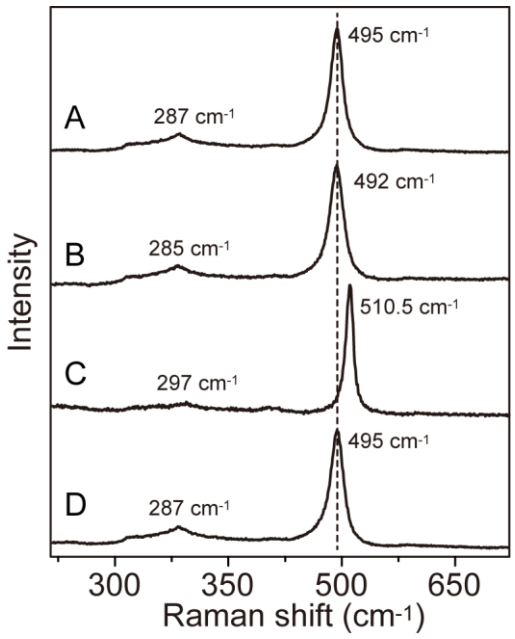

Figure 5. 7 Raman spectra of (A) AM-1, (B) AM-2, (C) AM-3, and (D) AM-5. The dashed line represents a Raman shift of 495 cm^{-1}.

5.3.2 Electrochemical Characterization

5.3.2.1 Galvanostatic Measurements

The voltage curves obtained from galvanostatic cycling of samples are shown in **Figure 5.8**. AM-1 exhibited a first charge (lithiation) capacity of 85 mAh/g and a first discharge (delithiation) capacity of 46 mAh/g, which decreased in subsequent cycles (**Fig. 5.8A**). Because of the large particles sizes in AM-1, the lithium diffusion distances were very long, and the carbon black additive may not have been sufficient to ensure good electronic conductivity through the composite electrode. As shown in **Figure 5.8B**, ball-milling resulted in a large increase in capacity, with a 472 mAh/g charge and 276 mAh/g discharge capacities observed in the first cycle of AM-2. These capacities correspond to ca. 20 Li^+ reversibly inserted per clathrate formula unit in AM-2, compared to around 3 Li^+ for

AM-1. Also notably, whereas the shape of the charge/discharge curves was rather linear in AM-1, in AM-2 a plateau feature was observed < 0.2 V vs. Li/Li^+. This increase in capacity after the sample was ball-milling can be explained by the decrease in particle size, as seen in the SEM imaging (**Fig. 5.8B**), but may also be due to additional capacity due to the electrochemical reaction of Li with the amorphous surface face.

To better understand this, the capacities of the other samples were also studied. After the acid/base treatments were applied, AM-3 showed a 126 mAh/g charge and 64 mAh/g discharge capacities in the first cycle (**Fig. 5.8C**), which is only 23% - 26% of the capacities of AM-2. Since the TEM imaging indicated that the amorphous layer was thinner after the acid/base treatment, the lower capacities in AM-3 compared to AM-2 could be due to removal of this layer of active material. Also, the layer rich in Si-O on the surface of the clathrate may have also played an inhibitory role on the reaction of Li^+ with the clathrate. The AM-4 and AM-5 results further support this hypothesis, as ball-milling of AM-3 resulted in higher capacities. As shown in **Figure 5.8D-E**, the first charge/discharge capacities were increased to 176 mAh/g and 98 mAh/g for AM-4 (40 minutes ball-milling) and 403 mAh/g and 276 mAh/g for AM-5 (120 minutes ball-milling), corresponding to increases in lithiation capacity by 40% and 220%, respectively, relative to AM-3. AM-5 displayed the highest number of Li^+ reversibly inserted in all the samples studied, about 25 Li^+ per formula unit.

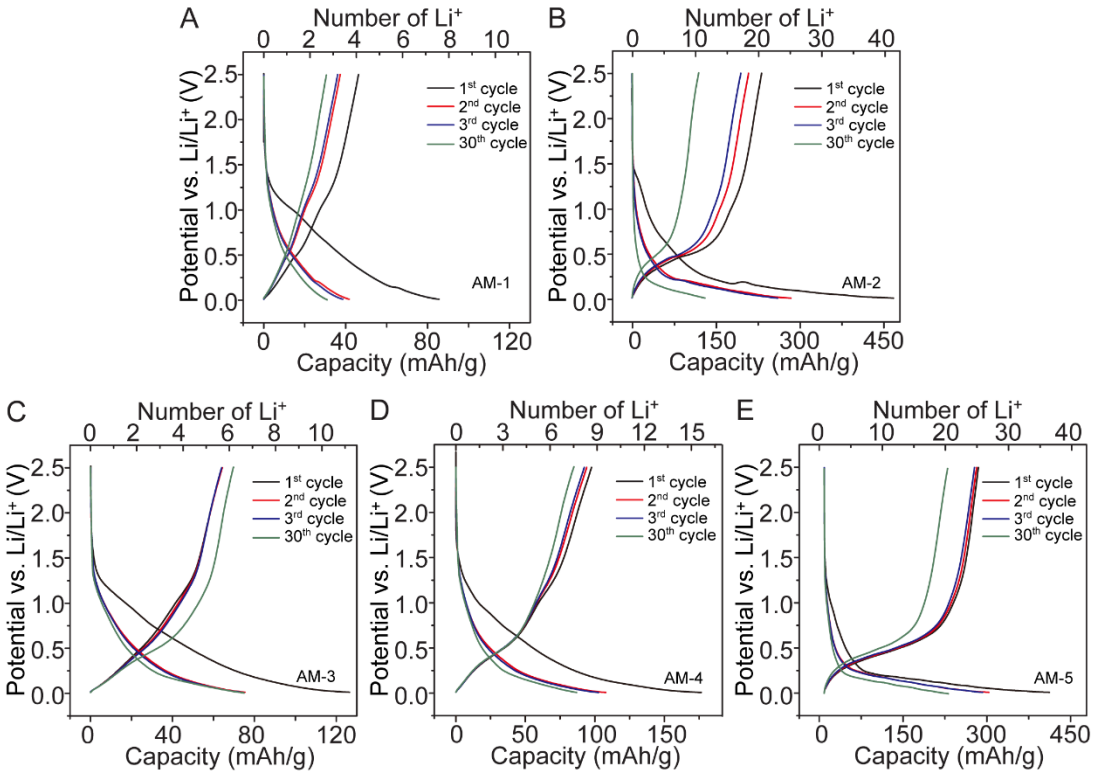

Figure 5. 8 Voltage profile of first three cycles and thirtieth cycle of (A) AM-1; (B) AM-2; (C) AM-3; (D) AM-4 and (E) AM-5.

From the SEM images (**Fig. 5.4D-E**), the longer ball-milling times can help to improve the uniformity of the particle morphology and decrease the particle size, but not dramatically. The XPS (**Fig. 5.6**) and Raman spectroscopy (**Fig. 5.7**) results support the exposure of non-oxide covered surfaces in AM-4 and AM-5, while the TEM analysis showed more amorphous layers were generated with the extended ball-milling time. From these observations, it appears that the formation of this amorphous surface layer on the clathrate particles plays a critical role in the observed electrochemical properties and higher specific capacities.

The long-term galvanostatic cycling performance and structural changes were also studied. As shown in **Figure 5.9,** the capacities of all of the samples decreased in after the first few cycles. The capacity of AM-1stablized at 37 mAh/g after 20 cycles. AM-3 and AM-4 displayed capacities of 78 mAh/g and 95 mAh/g after 100 cycles, respectively (**Fig. 5.9B**). The capacities also slightly increased at the later cycles, which implies some sort of activation process. This could be related to the removal of the silicon oxide surface during the electrochemical reaction, which would lead to more exposure of clathrate surface. This is reasonable for AM-3, which had the strongest Si-O XPS peak intensity. The similar cycling behavior of AM-3 and AM-4 suggests that the 40 minutes of ball-milling was not sufficient to expose all the clathrate surface.

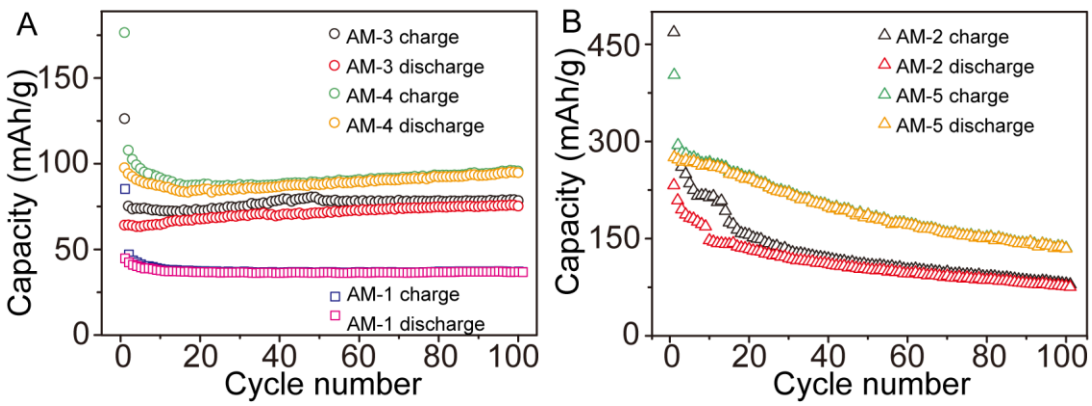

Figure 5. 9 Capacity vs. cycle number of (A) AM-1, AM-3 and AM-4, (b) AM-2 and AM-5.

The ball-milled samples AM-2 and AM-5 showed the worst capacity retention. The capacities of AM-2 and AM-5 dropped significantly from their initial values; a capacity of

79 mAh/g was observed from AM-2 after 100 cycles, and 136 mAh/g from AM-5 after 100 cycles (**Fig. 5.9C**).

5.3.2.2 GITT

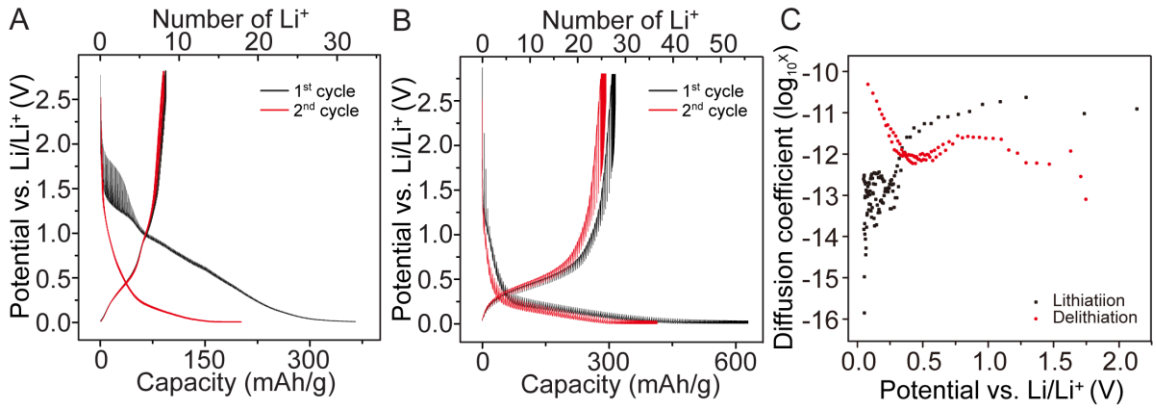

Figure 5. 10 GITT profile of (A) first two cycles of AM-3. (B) First two cycles of AM-5. (C) Diffusion coefficient vs. potential of the first cycle of AM-5.

To better understand some of the redox-dependent behavior, galvanostatic intermittent titration (GITT) and differential charge (dQ) plots were obtained. The polarization between 1 – 2 V vs. Li/Li^+ (**Fig. 5.10**), which corresponds to the peak centered around 1 V observed in the dQ plots (**Fig. 5.11A**) points to a side reaction likely due to reduction of the electrolyte to form a solid electrolyte interphase layer [212]. These features become undiscernible in the following cycle, suggesting that the SEI formation mostly takes place during the first cycle. This polarization was not as obvious in the ball-milled AM samples (**Fig. 5.10B**), which is consistent with the amorphous surface layer in those samples creating a different interface with the electrolyte, which might result in different SEI formation properties. **Figure 5.10C** showed the Li ion diffusion coefficients versus the

cell potential, which is about 10^{-12} to 10^{-16} cm^2s^{-1} for the lithiation below 0.5 V and about 10^{-10} to 10^{-12} cm^2s^{-1} for the delithiation. The diffusion coefficients are similar with the nano Si[213] and Si thin film/Si nanorods[214], which are about 10^{-10} to 10^{-12} cm^2s^{-1} and 10^{-12} to $10^{-15.5}$ cm^2s^{-1}.

5.3.2.3 Differential Plots

The AM-1and AM-3 samples were characterized by linear voltage profiles and dQ plots (**Fig. 5.11A**) that suggested a surface-dominated, capacitive adsorption mechanism [215]. On the other hand, for AM-2 and AM-5, the broad peaks were similar in position to those observed in our previous work on off-stoichiometric clathrates ($Ba_8Al_8Si_{30}$) [197] with reduction starting below ~0.3 V vs. Li/Li^+, and suggest a single-phase, solid solution lithiation mechanism (**Fig. 5.11B**). For both groups of samples, these characteristics were maintained even after 30 cycles (**Fig. 5.11C** and **5.11D**). Similar to our previous observations [197], the voltage-dependent redox characteristics in these samples were distinct from those observed in diamond cubic Si, amorphous Si, and SiO. The dQ plot associated with cubic Si reacting with Li is characterized by a sharp peak at 0.125 V vs. Li/Li^+ associated with a two-phase reaction to form amorphous lithium silicide and a peak near 50 mV which is attributed to the formation of $Li_{15}Si_4$ [100,216]. Lithiation of amorphous Si occurs as two single-phase reactions, which manifest as broad peaks centered at 0.25 and 0.1 V vs. Li/Li^+ in the dQ plots [217]. SiO undergoes a conversion reaction with Li to form lithium silicates and Li_2O, which showed a sharp peak in the differential charge plot at 0.25 V and a broad one at around 0.1 V vs. Li/Li^+ [218].

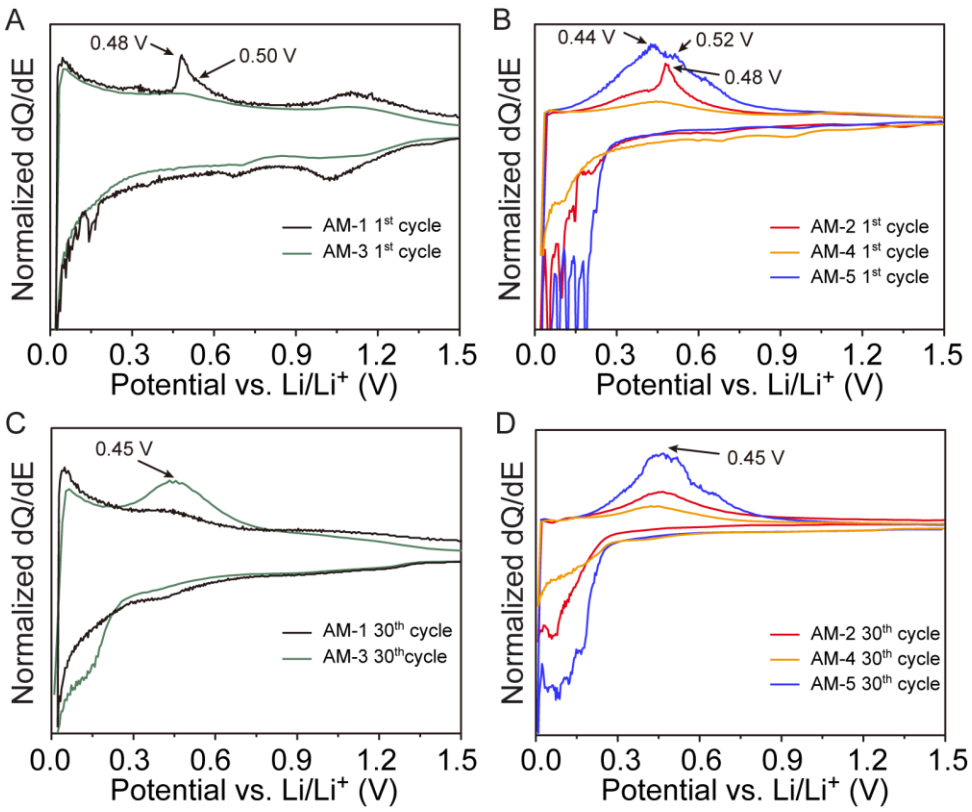

Figure 5. 11 Differential charge plots of AM-1and AM-3 (A) first cycle; (C) thirtieth cycle. Differential charge plots of AM-2 and AM-5 (B) first cycle; (D) thirtieth cycle.

During the delithiation process, broad peaks centered at 0.45 V vs. Li/Li^+ were observed in all of the samples. Compare with the off-stoichiometric clathrates, which exhibited a broad discharge peak at 0.4 V vs. Li/Li^+ in the dQ plots [197], the discharge voltage are higher, which is likely due to the difference of the composition (i.e. Al/Si ratio). Again, the dQ plots during discharge do not match those observed electrodes made of cubic Si, amorphous Si, or SiO. The cubic Si undergoes a two-phase delithiation reaction at about 0.43 V[216], while Li is removed in two single –phase reactions centered at 0.3 V and 0.5 V vs. Li/Li^+ in amorphous Si[217], delithiation of charged SiO shows similar characteristics with the amorphous Si. Small sharp peaks at 0.48 V were found in AM-1 and AM-2,

considering the impurities, those two unique peaks may come from the two-phase delithiation of c-$Li_{15}Si_4$ formed by the unreacted Si during charging. Therefore, the electrochemical properties of the clathrate are distinct and unique from those observed in lithiation of c-Si, a-Si, or SiO.

5.3.3 Structural Characterization during Electrochemical Reaction

XRD analysis of the electrodes after the first lithiation and after 100 cycles did not show a decrease in peak intensity (**Fig. 5.12**), suggesting that amorphization of the clathrate structure is not occurring as a result of the electrochemical lithium insertion reaction, and that amorphization is also not responsible for the decreasing capacities observed in the ball-milled samples AM-2 and AM-5. Rather, based on the TEM observations showing that ball-milling could introduce amorphous surface layers on the clathrate particles, it is likely that AM-2 and AM-5 have the highest capacities due to the electrochemical reaction of Li with these amorphous regions. However, this reaction is not as reversible as the surface-based processes that could be occurring in the other samples, particularly the samples without ball-milling (AM-1) that display the most reversible cycling.

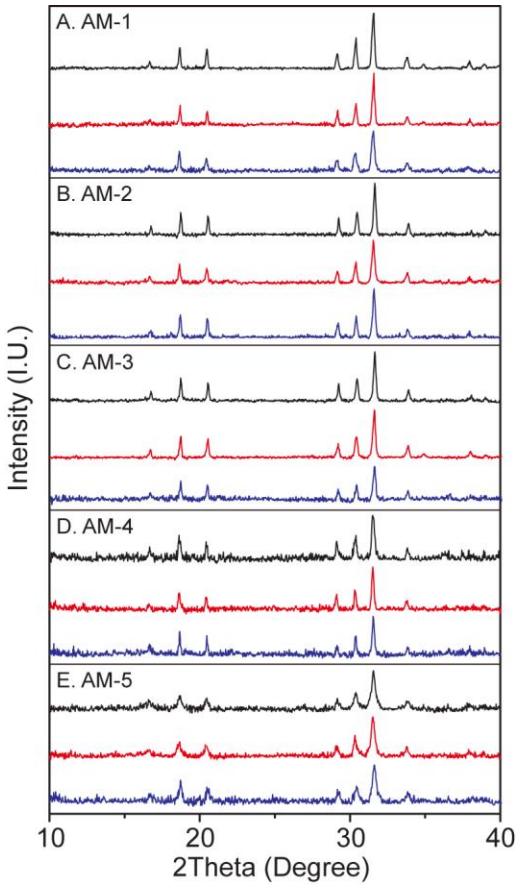

Figure 5. 12 XRD patterns of electrodes of pristine electrodes (black trace), electrodes after the first lithiation (red trace), and electrodes after 100 cycles (blue trace) for (A) AM-1, (B) AM-2, (C) AM-3, (D) AM-4, (E) AM-5.

5.4 Electrochemical Performance of other Silicon Clathrates

5.4.1 Synthesis of Silicon Clathrate by Arc-melting and Sample Preparation

In the arc-melting preparation, metals of Ba, Cu (or Ni), and Al were weighed in an Ar-filled glovebox with a total weight of ca. 600 mg to achieve a nominal composition of $Ba_8Cu_4Si_{42}$, $Ba_8Ni_4Si_{42}$, and $Ba_8Ni_2Al_8Si_{36}$. The metals were quickly transferred to the arc

melting chamber which was evacuated to ca. 10^{-4} Torr and backfilled with high purity argon. The formed ingot was then taken out and turned over. The melting process was repeated three times to ensure good homogeneity

After hand grinding the initial ingots, ball-milling was performed (SPEX 8000, stainless steel grinding set) for 40 minutes to decrease the particle size. The powder was suspended in de-ionized water and treated with 3 M HCl for 12 hours to remove the $BaSi_2$. After the acid treatment, the powder was recovered using vacuum filtration and washed with de-ionized water. Then, the powder was treated with 1 M NaOH for 12 hours to remove amorphous or cubic Si, then recovered using vacuum filtration and washed with de-ionized water and dried.

5.4.2 Materials Characterization

To identify the crystal structure of the samples, X-ray diffraction was performed. The data were collected using a Panalytical X'pert Pro diffractometer with CuKα radiation operating at 40 kV/40 mA.

The XRD pattern of Ba-Cu-Si matched the reflections associated with $Ba_8Cu_4Si_{42}$ (**Fig. 5.13A**). The reference pattern used for the clathrate was of $Ba_8Cu_4Si_{42}$ (PDF 00-051-1353)[194]. Additionally, some reflections that were not associated with the clathrate structure were observed at $2\theta = 28.5$. This reflection is likely from the (111) reflections of cubic Si, as this is commonly seen in clathrate syntheses indicating some unreacted precursor [183,203,204], and was removed by acid and base etching (**Fig. 5.13A Etched**).

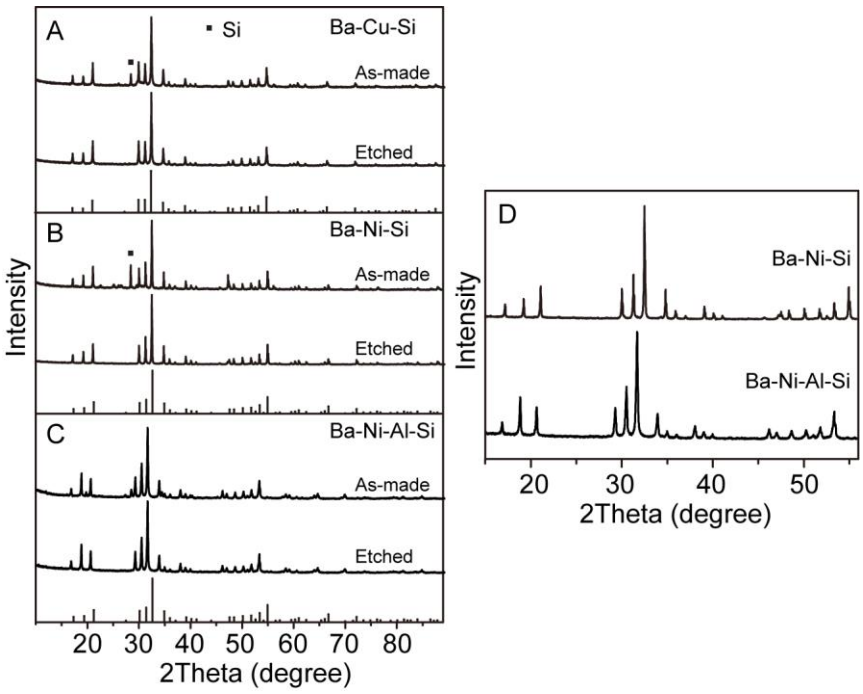

Figure 5. 13 XRD patterns of (A) $Ba_8Cu_4Si_{42}$, with the reference pattern of $Ba_8Cu_4Si_{42}$ (PDF 00-051-1353) (B) $Ba_8Ni_4Si_{42}$, with reference pattern of $Ba_8Ni_2Si_{44}$ (00-055-0390) and (C) $Ba_8Ni_2Al_8Si_{36}$, with the same $Ba_8Ni_2Si_{44}$ reference.

The XRD patterns of the clathrates with Ni were shown in **Figure 5.13B** and **5.13C**, with the reference pattern of $Ba_8Ni_2Si_{44}$ (00-055-0390)[194] as a comparison. Both of the samples contained impurities as Si and other small phases which were removed by acid and base etching (**Fig.5.13B** and **5.13C Etched**). Significant shifts to the lower angles were observed when comparing the sample $Ba_8Ni_2Al_8Si_{36}$ with $Ba_8Ni_4Si_{42}$ (**Fig.5.13D**), indicating an expansion of the unit cell. The covalent radius of Al is larger than Si[206], but smaller than Ni. In the case of Ba-Ni-Si clathrate, the framework contains four Ni atoms and forty two Si atoms, and two of the Ni atoms and six Si atoms were replaced by eight

Al atoms in the Ba-Ni-Al-Si clathrate. Therefore, the enlargement of the unit cell by Al substitution is greater than the contraction caused by the replacement of Ni by Al.

5.4.3 Electrochemical Measurement

The clathrate powder was prepared into slurries by mixing the clathrate sample with 10 wt% carbon black (to serve as conducting additive) and 10 wt% polyvinylidene difluoride (PVDF) (to serve as binder) in N-methyl pyrrolidone (NMP) as solvent. The slurries were stirred overnight and coated onto Cu foil current collectors using a Meyer rod, and then heated at 120 ^{o}C to remove the solvent. Pouch cells were assembled using Li metal as the counter electrode, Celgard 2500 as separator, and 1 M $LiPF_6$ (EC:DMC:DEC, 4:2:4 in volume, LBC 3051C, MTI) as electrolyte in the glovebox.

The voltage curves obtained from galvanostatic cycling of samples are shown in **Figure 5.14A-C**. $Ba_8Cu_4Si_{42}$ exhibited a first charge (lithiation) capacity of 184 mAh/g and a first discharge (delithiation) capacity of 69 mAh/g, which decreased in subsequent cycles to about 50 mAh/g. Similar performances were also found in $Ba_8Ni_2Si_{44}$ and $Ba_8Ni_2Al_8Si_{36}$, with capacities of 139/61 mAh/g (lithiation/delithiation), and 208/71 mAh/g (lithiation/delithiation), respectively, and the capacities of both samples decreased to about 60 mAh/g in the following cycles.

The differential plots are shown in **Figure 5.14D-E**, with the dotted lines for cubic silicon and amorphous silicon as comparisons. The dQ plots for the clathrate samples are quite district with the Si samples, and were characterized by linear voltage profiles and dQ plots that suggested a surface-dominated, capacitive adsorption mechanism [215], which is similar with AM-3. As discussed in chapter 5.3, all the samples are not active, likely due

to the oxidation layer generated by the acid and base etching but this should be confirmed in further studies.

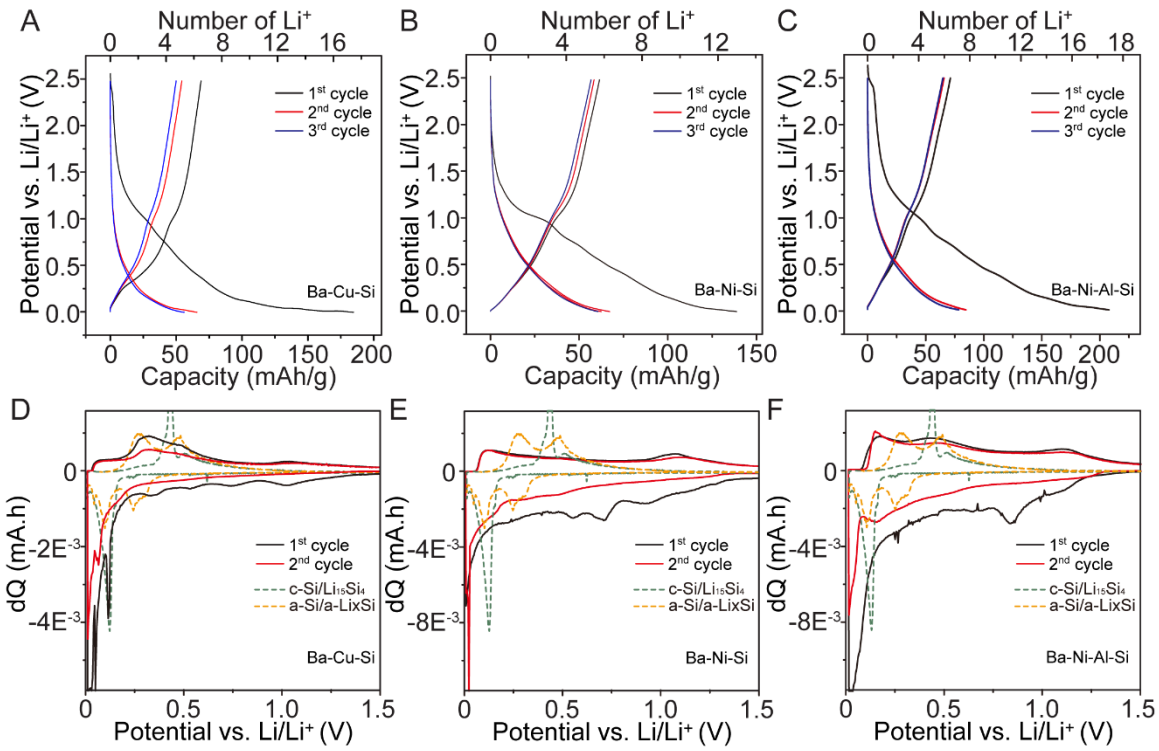

Figure 5. 14 Voltage profile of first three cycles of (A) $Ba_8Cu_4Si_{42}$, (B) $Ba_8Ni_2Si_{44}$ and (C) $Ba_8Ni_2Al_8Si_{36}$; First two differential plots for (D) $Ba_8Cu_4Si_{42}$, (E) $Ba_8Ni_2Si_{44}$ and (F) $Ba_8Ni_2Al_8Si_{36}$.

5.4.4 Structural Characterization

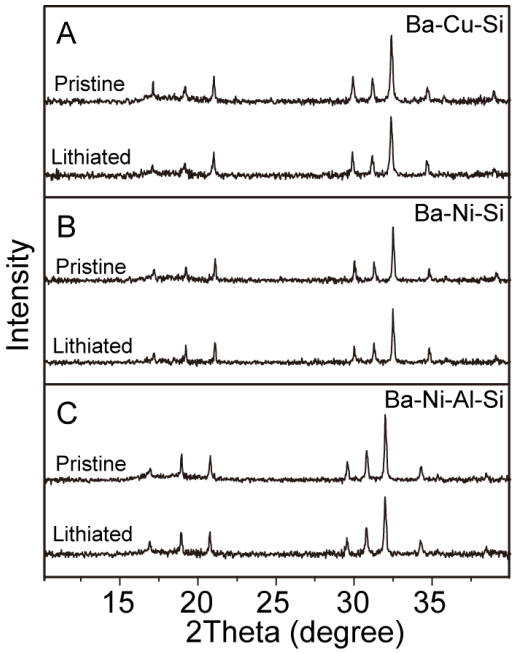

Figure 5. 15 XRD patterns of electrodes of pristine electrodes and electrodes after the first lithiation for (A) $Ba_8Cu_4Si_{42}$, (B) $Ba_8Ni_2Si_{44}$ and (C) $Ba_8Ni_2Al_8Si_{36}$.

XRD analysis of the pristine electrodes and electrodes after the first lithiation did not show a decrease in peak intensity (**Fig. 5.15**), suggesting that amorphization of the clathrate structure is not occurring as a result of the electrochemical lithium insertion reaction. This suggests that the reactions are mainly due to the surface absorption.

5.5 Conclusion

In conclusion, we performed a systematic investigation of the processing steps of silicon clathrate. Transmission electron microscope analysis showed ball-milling generated amorphous layer on the clathrate surface, which is crucial for the reaction with Li. The ball-milling process increased the capacity of hand ground clathrate from 85 mAh/g to 472 mAh/g, while the XPS analysis suggested a new oxide layer was introduced by the acid/base treatment, and confirmed by TEM, the former amorphous layer was partially removed. Thus, the decreased capacity of 126 mAh/g after the acid/base treatment is likely due to the removal of the amorphous layer and the presence of the oxidized surface layer inhibiting the reaction of Li^+ with clathrate. Further ball-milling can expose the clathrate surface again, and capacities of 176 mAh/g and 403 mAh/g were observed in the samples ball-milled for 40 and 120 minutes, respectively. According to the X-ray diffraction (XRD) analysis, all the lithiation/delithiation processes are proposed to occur in single phase reactions as there is no discernible structures change. These results show that for clathrate at the Zintl condition, Li insertion in the structure is unfavorable unless framework vacancies are introduced. The electrochemical performances of $Ba_8Cu_4Si_{42}$, $Ba_8Ni_2Si_{44}$ and $Ba_8Ni_2Al_8Si_{36}$ were also evaluated. All of those samples were ball-milled and acid/base etched. Due to the surface oxidation layer, those samples showed similar performance with the AM-3 sample of $Ba_8Al_{16}Si_{30}$.

6: ELECTROCHEMICAL PROPERTIES OF GERMANIUM CLATHRATE

6.1 Introduction

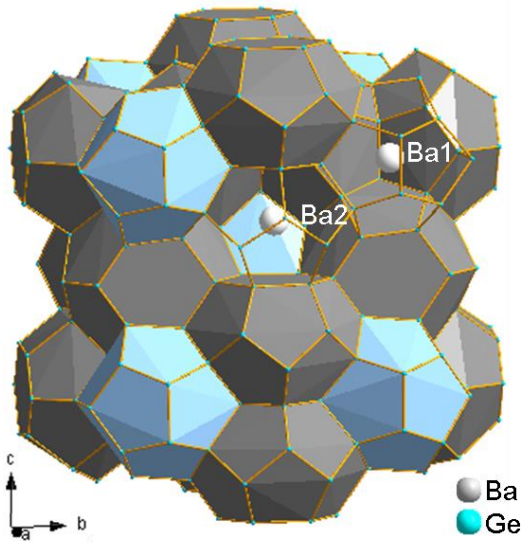

Figure 6. 1 Crystal structure of Ba_8Ge_{43}, distorted pentagondodecahedra (blue) and hexakaidecahedra (grey) in the germanium framework.

Here, we extend the studies described in the previous chapter to type I clathrates based on $M_8X_\delta Ge_{46-\delta}$ (M = Ba, K; X = Al, Li) in order to observe the electrochemical properties of Ge-based clathrates for the first time. Ba_8Ge_{43} was first obtained as a by-product of the decomposition of $Ba_3Ge_4C_2$ [222]. The Ba_8Ge_{43} structure was characterized as a defect type I clathrate type structure with three missing Ge atoms in the covalent germanium framework (a=10.6565(2)Å, space group *Pm-3n*, V=1210.2 $Å^3$)[223]; the appearance of spontaneous vacancies in this case can serve to maintain electron charge balance in off stoichiometry materials. Cabrera et al reported the Ge1(6c) position was partially (48.89%) occupied, and

Ge2 and Ge3 positions were fully occupied. They also reported a site splitting for Ge3 site, i.e. the Ge3 position split into two near sites. In their following study, they reported an investigation of the fully ordered defects in the Ge network (thermal annealed sample) in a superstructure (*Ia-3d*) of the clathrate-I type with a (*Ia-3d*) = 21.3123Å = 2 × a (*Pm-3n*) [224]. In the case of Ba-Al-Ge clathrates, there is Al substitution on the 6c, 16i, and 24k sites[225]. Based on the Zintl concept, the more electropositive "guest" atoms donate their valence electrons to the more electronegative "host" or cage atoms, so the latter can complete their valence requirement and build a covalently bonded cage structure. For $Ba_8Al_xGe_{46-x-y}$, the spontaneous vacancies y can be determined by balancing the electron count in the framework, which equals to (16-x)/4. There has also been experimental evidence showing that Li can occupy framework vacancies in the germanium clathrate $K_8Li_\delta Ge_{46-\delta}$ ($0 \leq \delta \leq 2.3$).[226]

6.2 Experimental Methods

6.2.1 Synthesis of Germanium Clathrate by Arc-melting

A series of clathrates with nominal composition of $Ba_8Al_\delta Ge_{46-\delta}$ (δ = 0, 4, 8, 12, 16) were synthesized using arc-melting. The samples were named according to Alδ, where δ represents the nominal amount of Al, e.g. Al0 means δ = 0 or Ba_8Ge_{46}. Metals of Ba, Si and Al (commercial grade materials with stated purity 99.9% wt) were weighed in the Ar-filled glove box (controlled O_2 and moisture atmosphere) according to the formula $Ba_8Al_\delta Ge_{46-\delta}$. An extra amount (5%) of Ba was loaded since Ba is more volatile than other elements, the total weight of the starting materials was ca. 600 mg. Then, the materials

were quickly transferred to the chamber of a custom-made arc-melter, which were evacuated to ca. 10^{-4} Torr and backfilled with high purity argon. After the initial melting, the formed ingot was taken out and turned over. The melting process was repeated three times to ensure good homogeneity. The weight of the ingot at the end of the process was checked and the observed loss was less than 0.5%. The as-made arc-melted ingots were processed further. HG-Alδ refers to the sample ground by hand using a mortar and pestle, while BM-Alδ refers to the HG-Alδ sample after ball-milling for 40 minutes.

6.2.2 Materials Characterization

6.2.2.1 X-ray Diffraction

Powder X-ray diffraction (XRD), scanning electron microscopy (SEM) and X-ray photoelectron spectroscopy (XPS) were used to perform structural and chemical characterization of the prepared Ge clathrate powders and composite electrodes before and after electrochemical cycling, the electrodes were rinsed several times with propylene carbonate and dried in an Argon-filled glovebox overnight.

6.2.2.2 Electron Microscopy

Powder XRD data were collected using a Panalytical X'pert Pro diffractometer with CuKα radiation operating at 40 kV/40 mA. Scanning electron microscopy (SEM) imaging was performed using an XL 30 ESEM-FEG microscope and a 12 kV electron beam. XPS was performed on a VG ESCALAB 220i-XL with Al Kα anode (1486.6 eV) operating at 63 W and 12 kV. The X-ray takeoff angle was 45° and the data were acquired from the region about ~400 μm of the surface of the sample. Charge compensation was used. A pass energy of 20 eV was used for high-resolution spectra (energy resolution 0.7 eV). The

spectra were calibrated to the hydrocarbon peak at 284.5 eV. Peak fitting was performed using CasaXPS processing software.

6.2.3 Electrochemical Measurement

HG-Alδ and BM-Alδ samples were prepared into slurries by mixing the clathrate sample with 10 wt% carbon black and 10 wt% polyvinylidene difluoride (PVDF) binder in N-methyl pyrrolidone (NMP) as solvent. The slurries were stirred overnight and coated onto Cu foil current collectors using a Meyer rod, and then heated at 120 ^{o}C for 3 hours to remove the solvent. Half-cells were assembled using Li metal as the counter electrode in the Ar-filled glovebox. Electrochemical testing was performed using a Biologic VMP3 galvanostat/potentiostat. Galvanostatic measurements were performed in the 0.01 – 2.5 V vs. Li/Li^{+} range using a current density of 25 mA/g of clathrate. For potentiodynamic measurements, a 5 mV voltage step was used with a threshold current density of 100 mA/g in the same voltage range.

6.3 Results and Discussion

6.3.1 Structural Characterization

XRD was performed on the synthesized Ge clathrates samples before and after grinding. All of the hand ground $Ba_8Al_\delta Ge_{46-\delta}$ samples (**Fig. 6.2A**) displayed crystalline clathrate peaks matching the reflections in Ba_8Ge_{43} (PDF 01-073-5638)[224], which is a 2 x2x2 superstructure of the normal cubic clathrate. For the Al containing samples, the peaks were shifted to lower angles, indicating an increase in the cell parameter. Rietveld

refinement was performed to determine the cell parameters and showed an increase from 21.31 Å for Al0 to 21.67 Å for Al16 (**Table 6.1**). The presence of crystalline Ge, identified by the (111) reflection, was noticeable in Al0 and Al4. Rietveld refinement to determine the phase fraction showed that the amount of Ge impurity was very small (**Table 6.1**). No other crystalline peaks were observed.

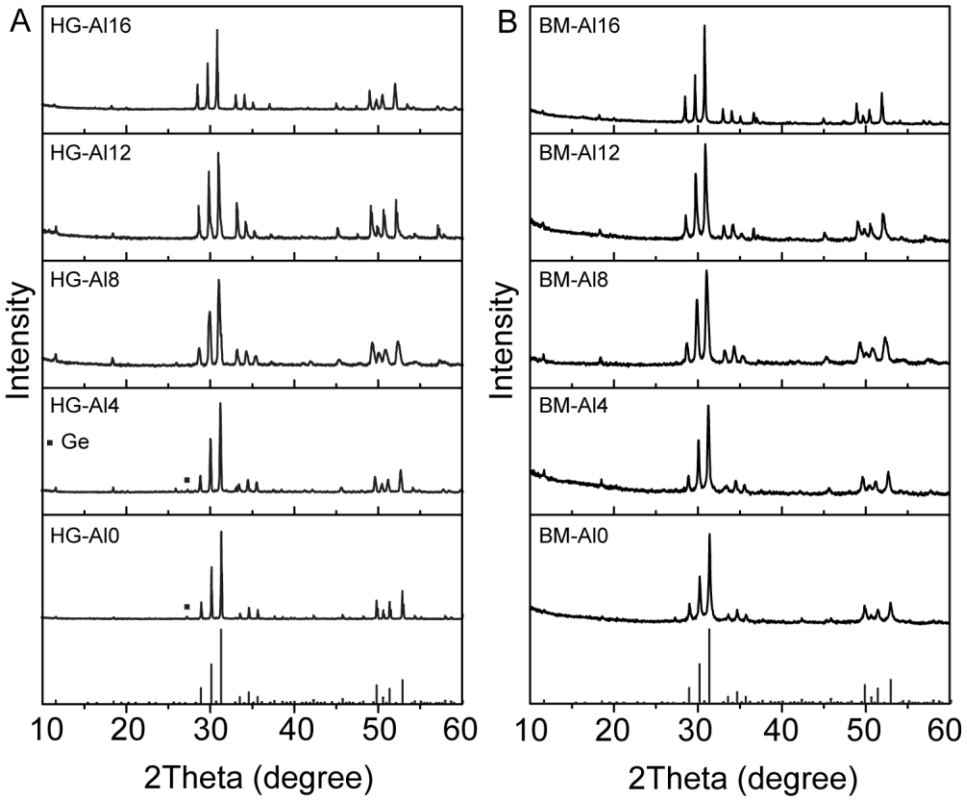

Figure 6. 2 XRD patterns of (A)as-made Ge clathrate and (B) ball-milled Ge clathrate with reference pattern PDF 01-073-5638 corresponding to Ba_8Ge_{43} on the bottom. (■) Ge.

XRD was also performed on the ball-milled clathrate powder (**Fig. 6.2B**). The powder after ball-milling also displayed a crystalline clathrate structure without any change of the

cell parameter and impurities, but the diffraction intensities decreased and the peaks were broader, which is consistent with a smaller particle size in the ball-milled samples.

Table 6. 1 Properties of synthesized Ge clathrates

Sample	a-parameter (Å)	Clathrate %	Ge %
Al0	21.3056	99.7	0.3
Al4	21.3885	98.5	1.5
Al8	21.5553	100	0
Al12	21.6010	100	0
Al16	21.6700	100	0

6.3.2 Electrochemical Characterization

6.3.2.1 Galvanostatic Measurements

The voltage curves obtained from galvanostatic cycling of HG and BM samples are shown in **Figure 6.3,** and the experimental results are summarized in **Table 6.2**, with theoretical capacities and the number of Li inserted (x) per formula unit (f.u.), the charge (lithiation) and discharge (delithiation capacities), corresponding to the number of Li inserted per clathrate formula unit and Coulombic efficiencies (CE) for the first cycle.

The theoretical capacities for the clathrates were calculated using the nominal composition (and its molecular weight) and assuming the clathrates undergo a conversion reaction upon lithiation. (The small weight % of Ge in $x < 8$ was neglected). It is known that germanium can alloy with lithium to form the $Li_{4.4}Ge$ alloy[227]. The highest theoretical capacity assuming full conversion for the Al-free Ge clathrate Al0 was 1201 mAh/g, which

corresponds to insertion of 189 Li per formula unit (f.u.). This value decreased as the Al content increased, as shown in **Table 6.2**.

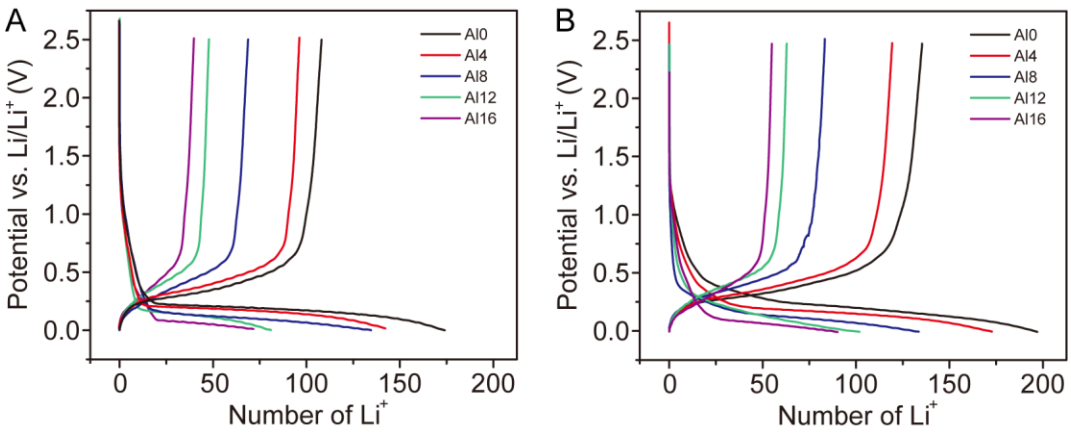

Figure 6. 3 Galvanostatic cycling data of (A) hand ground samples and (B) ball-milled samples.

Table 6. 2 Theoretical conversion capacities and experimentally observed capacities of Ge clathrates.

Al_δ	Theoretical		Experimental			
	Final Product: $Li_{4.4}Ge$		Hand ground samples		Ball-milled samples	
	Capacity (mAh/g)	# of Li per f.u.	Capacity (mAh/g) (CE%)	# of Li per f.u.	Capacity (mAh/g) (CE%)	# of Li per f.u.
0	1201	189	1098/683(62)	173/108	1248/858(69)	197/135
4	1163	184	896/607(68)	142/96	1087/751(69)	173/119
8	1100	167	883/451(51)	134/59	879/548(62)	134/83
12	1030	149	558/329(59)	81/59	702/431(61)	102/63
16	954	132	518/289(56)	72/56	651/397(61)	90/55

Comparing the results of hand ground and ball-milled sample, the ball-milling process can improve the performance, including the capacity and coulombic efficiency, which is reasonable considering Ge clathrate is not a good conductor, and the amount of material get reacted will be increased by decreasing the particle size. And on the other hand, the voltage profiles for the HG and BM samples were quite similar, indicating the ball-milling process do not change the reaction mechanism, so in the following discussion, only ball-milled samples were discussed.

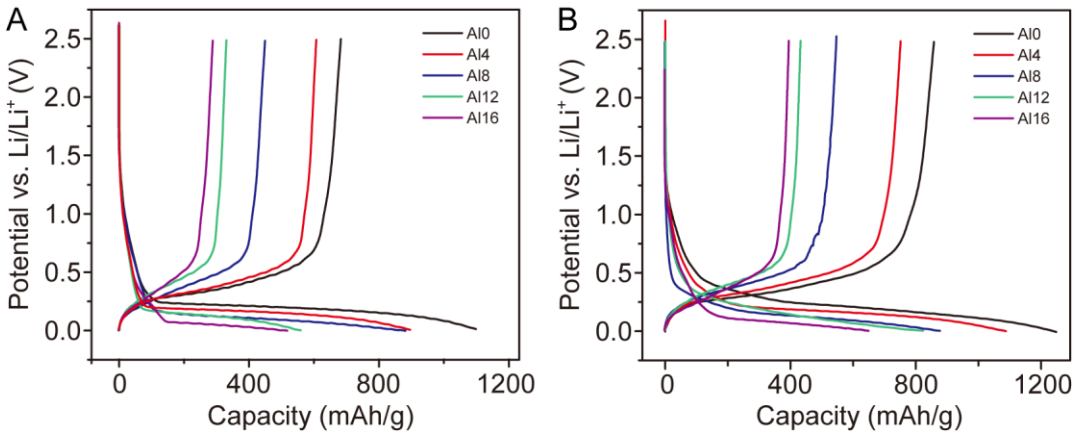

Figure 6. 4 Potential vs. specific capacity plots of the galvanostatic cyling data of (A) hand ground samples and (B) ball-milled samples.

Interestingly, a composition dependency on the first charge capacities was observed. BM-Al0 showed the highest numbers of Li^+ inserted, with x = 197; x decreased as the Al-content in the clathrate increased, with x = 90 for BM-Al16. This corresponds to specific capacities of 1248 mAh/g for Al0 compared to only 651 mAh/g for Al16, as shown in the potential vs. specific capacity plots in **Figure 6.4**. The observed first cycle charge for BM-Al0 is higher than the theoretical conversion capacity, suggesting that there some charge

devoted to formation of the solid electrolyte interphase (SEI) layer. This is confirmed by the low CE of 69% and SEM images (**Fig. 6.5**).

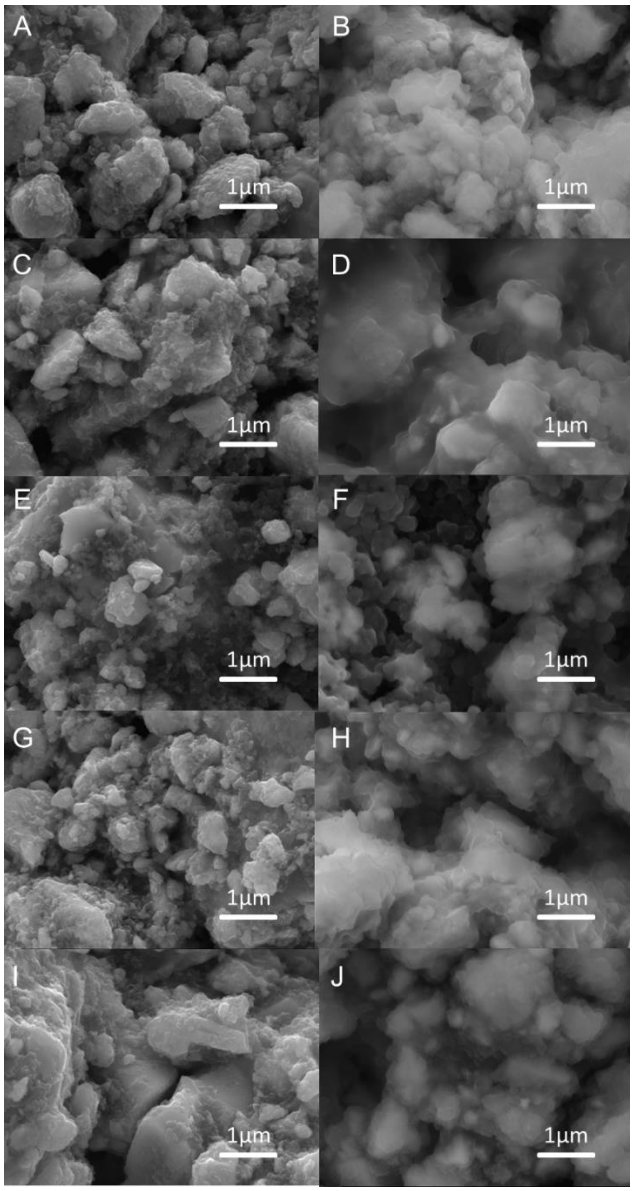

Figure 6. 5 SEM images of (A) pristine and (B)lithiated electrode of BM-Al0. (C) Pristine and (D)lithiated electrode of BM-Al4. (E) Pristine and (F)lithiated electrode of

BM-Al8. (G) Pristine and (H)lithiated electrode of BM-Al12. (I) pristine and (J) lithiated electrode.

Although the first discharge (delithiation) capacities for all of the samples followed a similar trend, with the highest capacities observed in Al0, the values were much lower, around 680 mAh/g. The 1st cycle CE was highest for BM-Al0 and BM-Al4 at 69%, which decreased with the decreasing of Al content, around 61% for the other samples. Further galvanostatic cycling showed the capacities for all the samples decreased rapidly below 100 mAh/g after 10 cycles (**Fig. 6.6**).

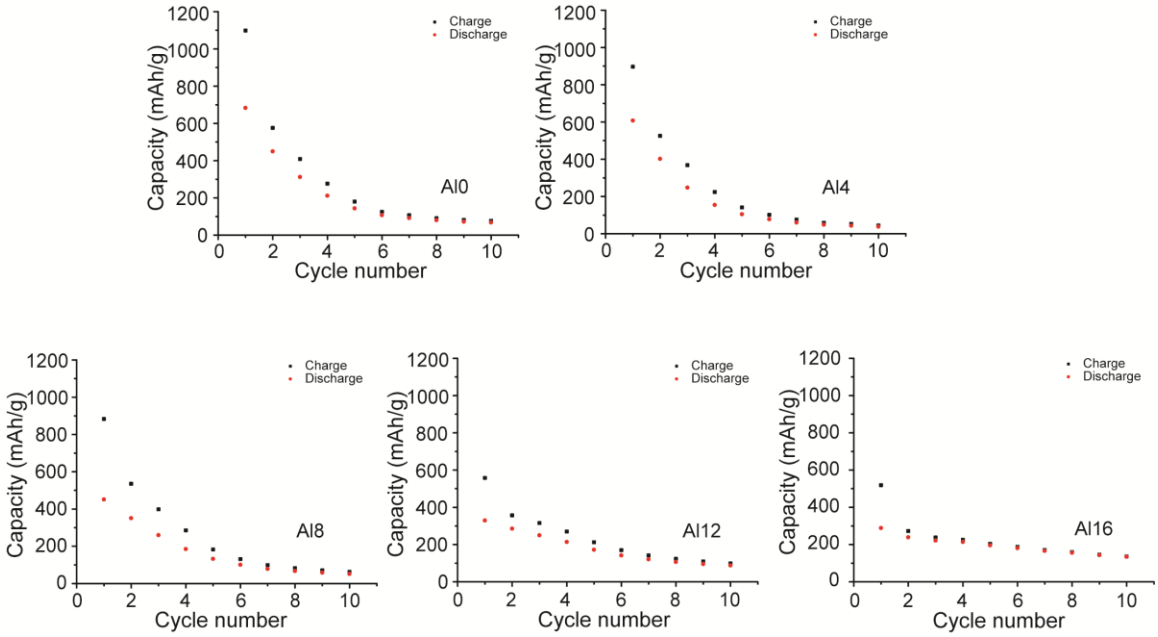

Figure 6. 6 Capacity vs cycle life for all the Ge clathrate samples.

6.3.2.2 Differential Plots

To investigate the electrochemical processes during charging and discharge, the differential capacity of the first two cycles of electrodes cycle at current rate of 100 mA/g were plotted and is shown in **Figure 6.7** with a Ge electrode which has been ball-milled for 40 minutes as a comparison. The dQ plot associated with ball-milled Ge reacting with Li is characterized by two peaks at ~ 0.33 V and 0.16 V, and replaced by one peak at 0.16 V. The peak at ~ 0.31 V is attributed to the lithiation of Ge to form a series of amorphous Li_xGe phases where $0 < x < 3.75$. The peak at 0.16 V for both first and second cycles is attributed to the formation of the amorphous, Li rich Ge alloy, a-$Li_{15}Ge_4$[228,229]. For the BM-Al0 to BM-Al12 samples, the lithiation peaks are broad and from ~0.13 V to 0.20 V, which may be associated with the formation of lithium rich a-LiGe, but due to the Ge bonding with Al and different amount of vacancies, the peak shapes were quite different with the pure Ge. For the lithiation for the BM-Al16 sample, the lithiation occurred around 0.06 V. When considering the crystal structure of $Ba_8Al_xGe_{46-x-y}$, y is the number of vacancies, which is equal to (16-x)/4. The amount of vacancies for BM-16 is the smallest, and equals to zero when the Al equals to 16. So the low reaction voltage may be explained by the different crystal structure containing the least amount of vacancies for Li diffusion.

The delithiation process of the Ge electrode occurres at 0.50 V and 0.66 V, associated with the delithiation of Li poor a-Li_xGe and Li rich a-Li_xGe. For the Ge clathrates, the discharge reactions occur over a broader voltage region, from 0.2 V to 0.6 V and more than one peak was observed, indicating the formation of a series of phases. Therefore, the electrochemical properties of the clathrate are distinct and unique from those observed in lithiation of Ge.

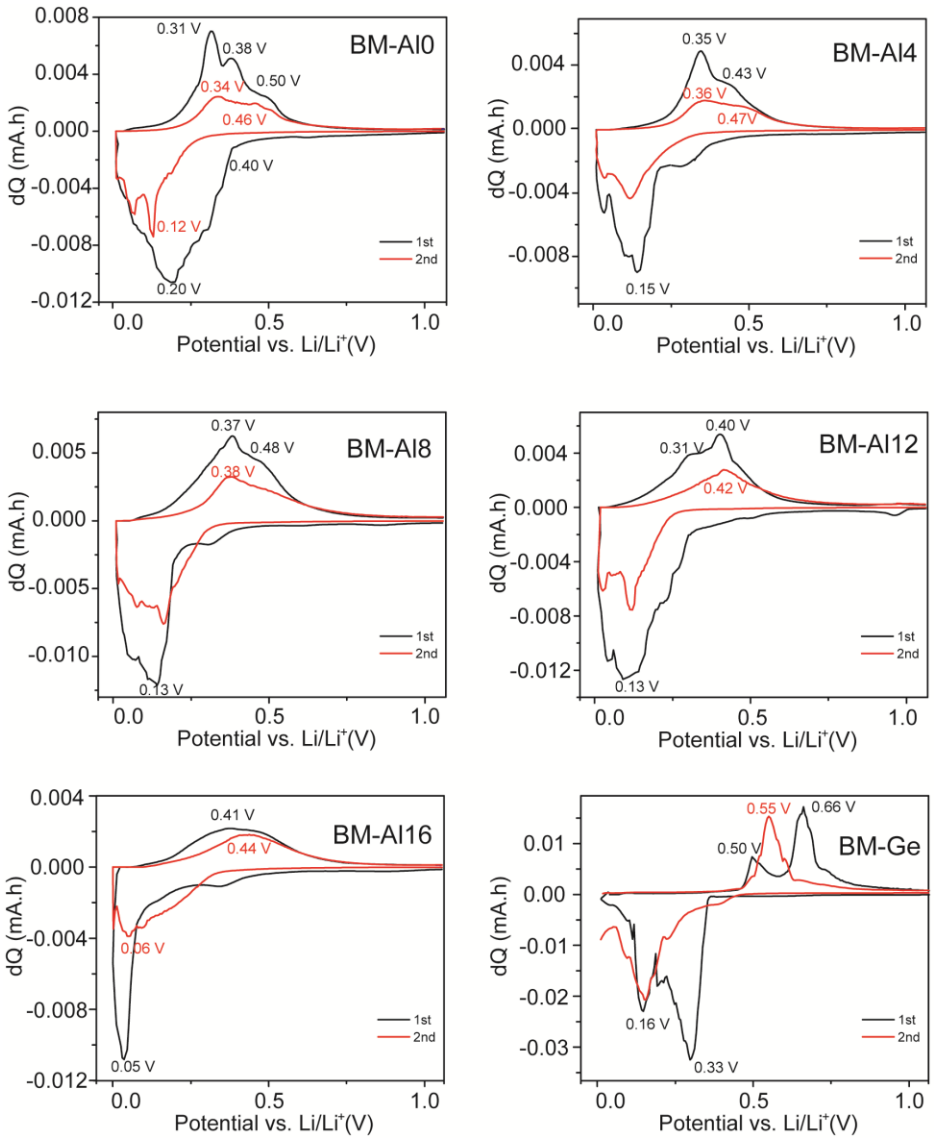

Figure 6. 7 Differential capacity plots of the first and second cycles of different ball-milled Ge clathrate samples and ball-milled Ge. The electrodes were cycled at a 100 mA/g current between 0.01V and 2.5V.

6.3.3 Structural Characterization after Electrochemical Reaction

XRD of the pristine electrodes and electrodes after the first charge was performed. As shown in **Figure 6.8**, the reflections associated with the clathrates all disappeared after one lithiation, suggesting the amorphization of the material and coversion reaction mechanisim. Considering the same trend for the theoretical and experimental capacities, which decreased with the decrease in Ge content, the electrochemical performance may mainly be due to the alloying of Ge and Li, which led to the formation of amorphous phases after the reaction.

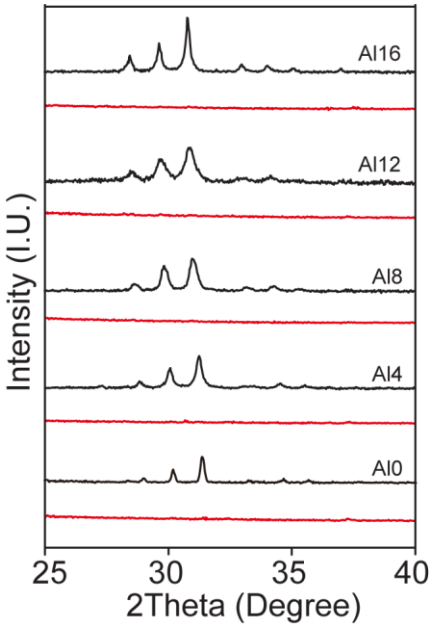

Figure 6. 8 XRD patterns of pristine electrodes (black) and lithiated electrodes (red).

Comparison of SEM images taken of the pristine electrodes compared with electrodes after the first lithiation did show indication of particle volume expansion and coating of the electrode with an SEI layer (**Fig. 6.5**), which may explain the fast decay of the capacities (**Fig. 6.6**)

6.4 Electrochemical Properties of Phosphide Clathrate Materials

Three different materials, $Ba_8Cu_{16}P_{30}$, $Ba_8Cu_{14}Ge_6P_{26}$ and $BaCu_2P_4$ are discussed in this section. These materials were synthesized by the research group of Prof. Kirill Kovnir from the University of California, Davis, and characterized by X-ray diffraction with the simulated patterns as references. No impurities were reported, so the materials were used as received.

$Ba_8Cu_{16}P_{30}$ was first synthesized and characterized by Dünner and Mewis in 1995 [230], and was reported to display semiconducting behavior with a band gap of 0.7 V. It belongs to the space group of Pbcn, a superstructure of the type I cubic clathrate structure without atomic disorder, where the Ba atoms are encapsulated in the cages formed by Cu and P atoms. On the other hand, there have been limited studies reporting the Cu and Ge substituted framework clathrate, $Ba_8Cu_{14}Ge_6P_{26}$. The unconventional clathrate, $BaCu_2P_4$ crystallized in the orthorhombic space group *Fddd*, which can transform to the type I clathrate $Ba_8Cu_{16}P_{30}$ at high temperatures. [231]

6.4.1 Electrochemical Measurement

The clathrate powder was prepared into slurries by mixing the clathrate sample with 10 wt% carbon black and 10 wt% polyvinylidene difluoride (PVDF) in N-methyl pyrrolidone (NMP) as solvent. The slurries were stirred overnight and coated onto Cu foil current collectors using a Meyer rod, and then heated at 120 ^oC to remove the solvent. Pouch cells were assembled using Li metal as the counter electrode, Celgard 2500 as separator, and 1 M $LiPF_6$ (EC:DMC:DEC, 4:2:4 in volume, LBC 3051C, MTI) as electrolyte in the glovebox. Electrochemical testing was performed using a Biologic VMP3.

Galvanostatic measurements were performed from 0.01 – 2.5 V vs. Li/Li^+ range with a C/20 rate. The current density used for $Ba_8Cu_{16}P_{30}$ was 20 mA/g, 39 mA/g for $Ba_8Cu_{14}Ge_6P_{26}$ and 118 mA/g for $BaCu_2P_4$.

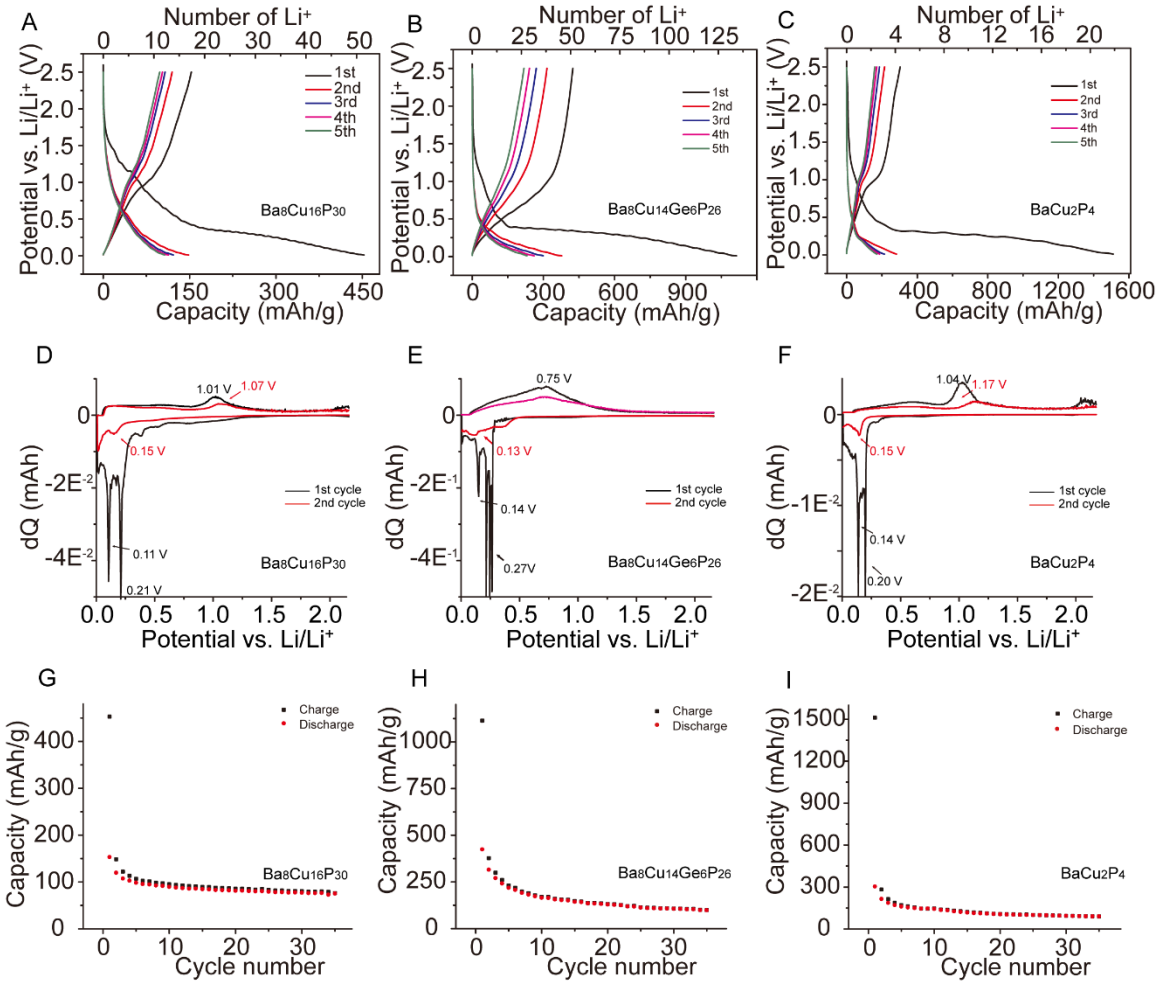

Figure 6. 9 Voltage profile of the first 5 cycles of (A) $Ba_8Cu_{16}P_{30}$, (B) $Ba_8Cu_{14}Ge_6P_{26}$ and (C) $BaCu_2P_4$. Differential plots of (D) $Ba_8Cu_{16}P_{30}$, (E) $Ba_8Cu_{14}Ge_6P_{26}$ and (F) $BaCu_2P_4$. Capacity vs. cycle number of (G) $Ba_8Cu_{16}P_{30}$, (H) $Ba_8Cu_{14}Ge_6P_{26}$ and (I) $BaCu_2P_4$.

The voltage curves obtained from galvanostatic cycling of the samples are shown in **Figure 6.9A-C**. $Ba_8Cu_{16}P_{30}$ exhibited a first charge capacity of 453 mAh/g and a first

discharge capacity of 153 mAh/g, which decreased to 80 mAh/g after 30 cycles (**Fig. 6.9G**). $Ba_8Cu_{14}Ge_6P_{26}$ showed a large increase in capacity, with a 1114 mAh/g charge and 424 mAh/g discharge capacities (**Fig. 6.9B**), which also decreased to about 80 mAh/g after 30 cycles(**Fig. 6.9H**). $BaCu_2P_4$ showed the highest lithiation capacity, exhibited a first charge capacity of 1511 mAh/g and a first discharge capacity of 303 mAh/g, which also fell to 80 mAh/g after 30 cycles (**Fig. 6.9I**).

To better understand the electrochemical reaction of the P clathrate, differential charge plots were also studied as shown in **Figure 6.9D-F.** For $Ba_8Cu_{16}P_{30}$ and $BaCu_2P_4$, two sharp peaks were observed around 0.20 V and 0.11 V during the first lithiation, and suggest a two phase, conversion lithiation mechanism, but the sharp peaks disappeared and a much smaller peak at 0.15 V was observed for the second cycle, which indicated the reaction during the first lithiation is somehow irreversible. For $Ba_8Cu_{14}Ge_6P_{26}$, the two sharp peaks for the first cycle and a much smaller peak for the second cycle were also observed, but the potentials change to 0.27 V, 0.14 V and 0.13 V, respectively, which may due to the Ge substitution. The dQ plots for the clathrate samples are quite distinct with phosphorus. During lithiation, the dQ plot associated with black phosphorus reacting with Li is characterized by two broad peaks at 0.78 V and 0.63 V vs. Li/Li^+ associated with two-phase reactions to form LiP and Li_2P, and a peak near 0.18 V which is attributed to the formation of Li_3P.[232–234]

During the delithiation process, broad peaks centered at 1 V vs. Li/Li^+ were observed in $Ba_8Cu_{16}P_{30}$ and $BaCu_2P_4$. Compare with phosphorus anodes, which exhibited a broad discharge peak at 1.12 V vs. Li/Li^+ in the dQ plots[234], the discharge voltage are slightly lower, which is likely due to the difference of chemical environment. Due to the Ge

substitution, the discharge peak of $Ba_8Cu_{14}Ge_6P_2$ is quite different with the other two samples, which showed a broad peak at 0.75 V. According to the electrochemical investigation, the reactions with Li are similar in $Ba_8Cu_{16}P_{30}$ and $BaCu_2P_4$, but the latter showed a higher capacity, about four times of $Ba_8Cu_{16}P_{30}$; the reaction of $Ba_8Cu_{14}Ge_6P_2$ is different with the other two clathrate due to the Ge substitution, and showed a high capacity of 1114 mAh/g for the first lithiation. During charging, all the samples showed a distinct and unique reaction from those observed in lithiation of phosphorus, but the discharging processes for $Ba_8Cu_{16}P_{30}$ and $BaCu_2P_4$ are similar with the phosphorus.

6.4.2 Structural Characterization after Electrochemical Reaction

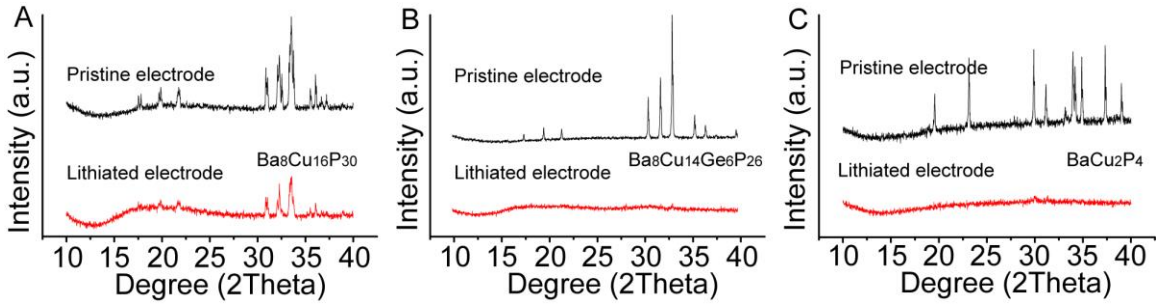

Figure 6. 10 XRD patterns of pristine (black) and lithiated (red) electrodes for (A) $Ba_8Cu_{16}P_{30}$, (B) $Ba_8Cu_{14}Ge_6P_{26}$ and (C) $BaCu_2P_4$.

XRD of the pristine electrodes and electrodes after the first charge was performed. As shown in **Figure 6.10A**, the intensity of the clathrate diffractions decreased after lithiation in sample $Ba_8Cu_{16}P_{30}$, suggesting the partial amorphization of the material, which can explain the low capacity as a result of the incomplete reaction. For the other samples, the

reflections associated with the clathrates all disappeared after one lithiation, suggesting the amorphization of the material and coversion reaction mechanisim.

6.5 Conclusion

In conclusion, we investigated a series of $Ba_8Al_\delta Ge_{46-\delta}$ (δ = 0, 4, 8, 12, 16) for use as an electrochemical energy storage material for the first time. According to the electrochemical and material characterization, the Ge clathrates underwent conversion reactions, with formation of amorphous products after lithiation. The highest numbers of Li^+ inserted observed in BM-Al0, with x=197; *x* decreased as the Ge-content in the clathrate decreased, with *x* = 90 for BM-Al16. This corresponds to specific capacities of 1248 mAh/g for BM-Al0 compared to 651 mAh/g for BM-Al16. By the differential plots analysis, the reaction is different and unique with lithiation of germanium, but still suffer from large volume changes.

The electrochemical properties of phosphorus clathrates were studied as well. $Ba_8Cu_{16}P_{30}$ showed the lowest capacity about 450 mAh/g for the first lithiation, and an incomplete reaction with lithium. $BaCu_2P_4$ showed a similar reaction voltage, with a higher capacity of 1510 mAh/g. $Ba_8Cu_{14}Ge_6P_{26}$ exhibited a capacity of 1110 mAh/g with a different reaction voltage due to the Ge substitution. All of the materials underwent conversion reactions, and suffered from bad capacity retention.

REFERENCES

(1) Energy Density Comparison of Size & Weight http://www.epectec.com/batteries/cell-comparison.html.

(2) Tarascon, J. M.; Armand, M. Issues and Challenges Facing Rechargeable Lithium Batteries. *Nature* **2001**, *414* (6861), 359–367.

(3) Le Blanc, A.; Rouxel, J. Sur Les Types Structuraux Des Composés Intercalaires $MSnS_2$ (M= Li, Na, K, Rb). *Comptes Rendus Acad Sci, Ser. C, Sci Chim.* **1972**, *274*, 786–788.

(4) Steele, B.; Gool, W. Van. *Fast Ion Transport in Solids*; 1973.

(5) Whittingham, M. S. Electrical Energy Storage and Intercalation Chemistry. *Science.* **1976**, *192* (4244), 1126–1127.

(6) Mizushima, K.; Jones, P. C.; Wiseman, P. J.; Goodenough, J. B. $LixCoO_2$ ($0<x\leq1$): A New Cathode Material for Batteries of High Energy Density. *Solid State Ionics* **1981**, *3–4* (C), 171–174.

(7) Thackeray, M. M.; David, W. I. F.; Bruce, P. G.; Goodenough, J. B. Lithium Insertion into Manganese Spinels. *Mater. Res. Bull.* **1983**, *18* (4), 461–472.

(8) Thackeray, M. M.; Johnson, P. J.; de Picciotto, L. A.; Bruce, P. G.; Goodenough, J. B. Electrochemical Extraction of Lithium from $LiMn_2O_4$. *Mater. Res. Bull.* **1984**, *19* (2), 179–187.

(9) Yazami, R.; Touzain, P. A Reversible Graphite-Lithium Negative Electrode for Electrochemical Generators. *J. Power Sources* **1983**, *9* (3), 365–371.

(10) Lee, H.; Yanilmaz, M.; Toprakci, O.; Fu, K.; Zhang, X. A Review of Recent Developments in Membrane Separators for Rechargeable Lithium-Ion Batteries. *Energy Environ. Sci.* **2014**, *7* (12), 3857–3886.

(11) Huggins, R. a. *Advanced Batteries, Materials Science Aspects*; Springer Sciece + Business Media, LLC, 2009.

(12) Wu, H.; Cui, Y. Designing Nanostructured Si Anodes for High Energy Lithium Ion Batteries. *Nano Today* **2012**, *7* (5), 414–429.

(13) Chan, C. K.; McIlwrath, K.; Huggins, R. A. High-Performance Lithium Battery Anodes Using Silicon Nanowires. *Nat. Nanotechnol.* **2008**, *3* (1), 31–35.

(14) Nagaura, T.; Tozawa, K. Lithium Ion Rechargeable Battery. *Prog. Batter. Sol. Cells* **1990**, *9*, 209–212.

(15) Whittingham, M. S. Lithium Batteries and Cathode Materials. *Chem. Rev.* **2004**, *104* (10), 4271–4301.

(16) Barker, J.; Gover, R. K. B.; Burns, P.; Bryan, A.; Saidi, M. Y.; Swoyer, J. L. Structural and Electrochemical Properties of Lithium Vanadium Fluorophosphate, $LiVPO_4F$. *J. Power Sources* **2005**, *146* (1–2), 516–520.

(17) Barpanda, P.; Ati, M.; Melot, B. C.; Rousse, G.; Chotard, J.-N.; Doublet, M.-L.; Sougrati, M. T.; Corr, S. a.; Jumas, J.-C.; Tarascon, J.-M. A 3.90 V Iron-Based Fluorosulphate Material for Lithium-Ion Batteries Crystallizing in the Triplite Structure. *Nat. Mater.* **2011**, *10* (10), 772–779.

(18) Recham, N.; Chotard, J.-N.; Dupont, L.; Delacourt, C.; Walker, W.; Armand, M.; Tarascon, J.-M. A 3.6 V Lithium-Based Fluorosulphate Insertion Positive Electrode for Lithium-Ion Batteries. *Nat. Mater.* **2010**, *9* (1), 68–74.

(19) Nytén, A.; Abouimrane, A.; Armand, M.; Gustafsson, T.; Thomas, J. O. Electrochemical Performance of Li_2FeSiO_4 as a New Li-Battery Cathode Material. *Electrochem. commun.* **2005**, *7* (2), 156–160.

(20) Uebou, Y.; Okada, S.; Egashira, M.; Yamaki, J. I. Cathode Properties of Pyrophosphates for Rechargeable Lithium Batteries. *Solid State Ionics* **2002**, *148* (3–4), 323–328.

(21) Stanley Whittingham, M. Ultimate Limits to Intercalation Reactions for Lithium Batteries. *Chem. Rev.* **2014**, *114* (23), 11683–11720.

(22) Nitta, N.; Wu, F.; Lee, J. T.; Yushin, G. Li-Ion Battery Materials: Present and Future. *Mater. Today* **2015**, *18* (5), 252–264.

(23) Jain, A.; Ong, S. P.; Hautier, G.; Chen, W.; Richards, W. D.; Dacek, S.; Cholia, S.; Gunter, D.; Skinner, D.; Ceder, G.; et al. Commentary: The Materials Project: A Materials Genome Approach to Accelerating Materials Innovation. *APL Mater.* **2013**, *1* (1).

(24) Che, G.; Jirage, K. B.; Fisher, E. R.; Martin, C. R.; Yoneyama, H. Chemical-Vapor Deposition-Based Template Synthesis of Microtubular TiS_2 Battery Electrodes. *J. Electrochem. Soc.* **1997**, *144* (12), 4296–4302.

(25) Cho, J.; Kim, Y.-W.; Kim, B.; Lee, J.-G.; Park, B. A Breakthrough in the Safety of Lithium Secondary Batteries by Coating the Cathode Material with $AlPO_4$ Nanoparticles. *Angew. Chemie Int. Ed.* **2003**, *42* (14), 1618–1621.

(26) Ohzuku, T.; Ueda, A.; Nagayama, M. Electrochemistry and Structural Chemistry of $LiNiO_2$ (R-3m) for 4 Volt Secondary Lithium Cells. *J. Electrochem. Soc.* **1993**, *140* (7), 1862–1870.

(27) Bruce, P. G.; Armstrong, a. R.; Gitzendanner, R. L. New Intercalation Compounds for Lithium Batteries: Layered $LiMnO_2$. *J. Mater. Chem.* **1999**, *9* (1), 193–198.

(28) Martha, S. K.; Haik, O.; Zinigrad, E.; Exnar, I.; Drezen, T.; Miners, J. H.; Aurbach, D. On the Thermal Stability of Olivine Cathode Materials for Lithium-Ion Batteries. *J. Electrochem. Soc.* **2011**, *158* (10), A1115.

(29) Wang, R.; He, X.; He, L.; Wang, F.; Xiao, R.; Gu, L.; Li, H.; Chen, L. Atomic Structure of Li_2MnO_3 after Partial Delithiation and Re-Lithiation. *Adv. Energy Mater.* **2013**, *3* (10), 1358–1367.

(30) Choi, S.; Manthiram, A. Synthesis and Electrochemical Properties of $LiCo_2O_4$ Spinel Cathodes. *J. Electrochem. Soc.* **2002**, *149* (2), A162.

(31) Yamada, A.; Chung, S. C.; Hinokuma, K. Optimized $LiFePO_4$ for Lithium Battery Cathodes. *J. Electrochem. Soc.* **2001**, *148* (3), A224–A229.

(32) Choi, D.; Wang, D.; Bae, I. T.; Xiao, J.; Nie, Z.; Wang, W.; Viswanathan, V. V.; Lee, Y. J.; Zhang, J. G.; Graff, G. L.; et al. $LiMnPO_4$ Nanoplate Grown via Solid-State Reaction in Molten Hydrocarbon for Li-Ion Battery Cathode. *Nano Lett.* **2010**, *10* (8), 2799–2805.

(33) Lloris, J. M.; Pérez Vicente, C.; Tirado, J. L. Improvement of the Electrochemical Performance of $LiCoPO_4$ 5 V Material Using a Novel Synthesis Procedure. *Electrochem. Solid-State Lett.* **2002**, *5* (10), A234.

(34) Sobkowiak, A.; Roberts, M. R.; Younesi, R.; Ericsson, T.; Häggström, L.; Tai, C. W.; Andersson, A. M.; Edström, K.; Gustafsson, T.; Björefors, F. Understanding and Controlling the Surface Chemistry of $LiFeSO_4F$ for an Enhanced Cathode Functionality. *Chem. Mater.* **2013**, *25* (15), 3020–3029.

(35) Poizot, P.; Laruelle, S.; Grugeon, S.; Dupont, L.; Tarascon, J. Nano-Sized Transition-Metal Oxides as Negative-Electrode Materials for Lithium-Ion Batteries. *Nature* **2000**, *407* (6803), 496–499.

(36) Grugeon, S.; Laruelle, S.; Herrera-Urbina, R.; Dupont, L.; Poizot, P.; Tarascon, J.-M. Particle Size Effects on the Electrochemical Performance of Copper Oxides toward Lithium. *J. Electrochem. Soc.* **2001**, *148* (4), A285.

(37) Poizot, P.; Chevallier, F.; Laffont, L.; Morcrette, M.; Rozier, P.; Tarascon, J.-M. Evidence of an Electrochemically Assisted Ion Exchange Reaction in $Cu_{2.33}V_4O_{11}$ Electrode Material vs. Li. *Electrochem. Solid-State Lett.* **2005**, *8* (4), A184.

(38) Morcrette, M.; Martin, P.; Rozier, P.; Vezin, H.; Chevallier, F.; Laffont, L.; Poizot, P.; Tarascon, J.-M. $Cu1.1V_4O_{11}$: A New Positive Electrode Material for Rechargeable Li Batteries. *Chem. Mater.* **2005**, *17* (3), 418–426.

(39) Morcrette, M.; Rozier, P.; Dupont, L.; Mugnier, E.; Sannier, L.; Galy, J.; Tarascon, J.-M. A Reversible Copper Extrusion-Insertion Electrode for Rechargeable Li Batteries. *Nat. Mater.* **2003**, *2*, 755–761.

(40) Badway, F.; Mansour, A. N.; Pereira, N.; Al-Sharab, J. F.; Cosandey, F.; Plitz, I.; Amatucci, G. G. Structure and Electrochemistry of Copper Fluoride Nanocomposites Utilizing Mixed Conducting Matrices. *Chem. Mater.* **2007**, *19* (17), 4129–4141.

(41) Wang, F.; Robert, R.; Chernova, N. A.; Pereira, N.; Omenya, F.; Badway, F.; Hua, X.; Ruotolo, M.; Zhang, R.; Wu, L.; et al. Conversion Reaction Mechanisms in Lithium Ion Batteries: Study of the Binary Metal Fluoride Electrodes. *J. Am. Chem. Soc.* **2011**, *133* (46), 18828–18836.

(42) Li, T.; Chen, Z. X.; Cao, Y. L.; Ai, X. P.; Yang, H. X. Transition-Metal Chlorides as Conversion Cathode Materials for Li-Ion Batteries. *Electrochim. Acta* **2012**, *68*, 202–205.

(43) Bodenez, V.; Dupont, L.; Morcrette, M.; Surcin, C.; Murphy, D. W.; Tarascon, J. M. Copper Extrusion/reinjection in Cu-Based Thiospinels by Electrochemical and Chemical Routes. *Chem. Mater.* **2006**, *18* (18), 4278–4287.

(44) Crosnier, O.; Mounsey, C.; Herle, P. S.; Taylor, N.; Nazar, L. F. Crystal Structure and Electrochemical Behavior of Li_2CuP: A Surprising Reversible Crystalline-Amorphous. *Chem. Mater.* **2003**, *15* (8), 4890–4892.

(45) Crosnier, O.; Nazar, L. F. Facile Reversible Displacement Reaction of Cu_3P with Lithium at Low Potential. *Electrochem. Solid-State Lett.* **2004**, *7* (7), A187–A189.

(46) Schwieger, J. N.; Kraytsberg, A.; Ein-Eli, Y. Copper Sulfates as Cathode Materials for Li Batteries. *J. Power Sources* **2011**, *196* (3), 1461–1468.

(47) Parzych, G.; Mikhailova, D.; Oswald, S.; Eckert, J.; Ehrenberg, H. Study of the Conversion Reaction Mechanism for Copper Borate as Electrode Material in Lithium-Ion Batteries. *J. Electrochem. Soc.* **2011**, *158* (8), A898.

(48) Badway, F.; Cosandey, F.; Pereira, N.; Amatucci, G. G. Carbon Metal Fluoride Nanocomposites. *J. Electrochem. Soc.* **2003**, *150* (10), A1318.

(49) Li, L.; Meng, F.; Jin, S. High-Capacity Lithium-Ion Battery Conversion Cathodes Based on Iron Fluoride Nanowires and Insights into the Conversion Mechanism. *Nano Lett.* **2012**, *12* (11), 6030–6037.

(50) Li, C.; Gu, L.; Tong, J.; Tsukimoto, S.; Maier, J. A Mesoporous Iron-Based Fluoride Cathode of Tunnel Structure for Rechargeable Lithium Batteries. *Adv. Funct. Mater.* **2011**, *21* (8), 1391–1397.

(51) Gmitter, A. J.; Badway, F.; Rangan, S.; Bartynski, R. a.; Halajko, A.; Pereira, N.; Amatucci, G. G. Formation, Dynamics, and Implication of Solid Electrolyte Interphase in High Voltage Reversible Conversion Fluoride Nanocomposites. *J. Mater. Chem.* **2010**, *20* (20), 4149.

(52) Sina, M.; Thorpe, R.; Rangan, S.; Pereira, N.; Bartynski, R. A.; Amatucci, G. G.; Cosandey, F. Investigation of SEI Layer Formation in Conversion Iron Fluoride Cathodes by Combined STEM/EELS and XPS. *J. Phys. Chem. C* **2015**, *119* (18), 9762–9773.

(53) Silicon anode Li-ion battery technology http://www.nexeon.co.uk/technology-2/benefits-of-nexeon-technology/ (accessed Mar 29, 2017).

(54) Kaskhedikar, N. A.; Maier, J. Lithium Storage in Carbon Nanostructures. *Adv. Mater.* **2009**, *21* (25–26), 2664–2680.

(55) Zhang, W. J. A Review of the Electrochemical Performance of Alloy Anodes for Lithium-Ion Batteries. *J. Power Sources* **2011**, *196* (1), 13–24.

(56) Barbara L Dutrow; Christine M. Clark. X-ray Powder Diffraction (XRD) http://serc.carleton.edu/research_education/geochemsheets/techniques/XRD.html (accessed Mar 29, 2017).

(57) Purdue University - Scanning Electron Microscope https://www.purdue.edu/ehps/rem/rs/sem.htm (accessed Mar 29, 2017).

(58) *EC-Lab Sofrware: Techniques and Applications*, version 10.; BioLogic Science Instruments, 2014.

(59) Weppner, W.; Huggins, R. A. Determination of the Kinetic Parameters of Mixed-Conducting Electrodes and Application to the System Li_3Sb. *J. Electrochem. Soc.* **1977**, *124*, 1569–1578.

(60) Yamakawa, N.; Jiang, M.; Grey, C. P. Investigation of the Conversion Reaction Mechanisms for Binary Copper(II) Compounds by Solid-State NMR Spectroscopy and X-Ray Diffraction. *Chem. Mater.* **2009**, *21* (14), 3162–3176.

(61) Debart, A.; Dupont, L.; Patrice, R.; Tarascon, J.-M. Reactivity of Transition Metal (Co, Ni, Cu) Sulphides versus Lithium: The Intriguing Case of the Copper Sulphide. *Solid State Sci.* **2006**, *8* (6), 640–651.

(62) Podhajecky, P.; Scrosati, B. Copper Oxide Cathodes for Lithium Organic Electrolyte Batteries. *J. Power Sources* **1985**, *16* (4), 309–317.

(63) Manthiram, A.; Goodenough, J. B. Lithium Insertion into $Fe_2(MO_4)_3$ Frameworks: Comparison of M = W with M = Mo. *J. Solid State Chem.* **1987**, *71* (2), 349–360.

(64) Manthiram, A.; Goodenough, J. B. Lithium Insertion into $Fe_2(SO_4)_3$ Frameworks. *J. Power Sources* **1989**, *26*, 403–408.

(65) Aricò, A. S.; Bruce, P.; Scrosati, B.; Tarascon, J.; Schalkwijk, walter van. Nanostructured Materials for Advanced Energy Conversion and Storage Devices. *Nat. Mater.* **2005**, *4*, 366–377.

(66) Sabelli, C.; Trosti-Ferroni, R. A Structural Classification of Sulfate Minerals. *Period. Miner.* **1985**, *54*, 1–46.

(67) Helliwell, M.; Smith, J. V. Brochantite. *Acta Crystallogr. Sect. C Cryst. Struct. Commun.* **1997**, *53*, 1369–1371.

(68) Merlino, S.; Perchiazzi, N.; Franco, D. Brochantite, $Cu_4SO_4(OH)_6$: OD Character, Polytypism and Crystal Structures. *Eur. J. Mineral.* **2003**, *15* (2), 267–275.

(69) Woods, T. L.; Garrels, R. M. Use of Oxidized Copper Minerals as Environmental Indicators. *Appl. Geochemistry* **1986**, *1* (2), 181–187.

(70) Livingston, R. a. Influence of the Environment on the Patina of the Statue of Liberty. *Environ. Sci. Technol.* **1991**, *25* (8), 1400–1408.

(71) Chiavari, C.; Rahmouni, K.; Takenouti, H.; Joiret, S.; Vermaut, P.; Robbiola, L. Composition and Electrochemical Properties of Natural Patinas of Outdoor Bronze Monuments. *Electrochim. Acta* **2007**, *52*, 7760–7769.

(72) Vilminot, S.; Richard-Plouet, M.; André, G.; Swierczynski, D.; Bourée-Vigneron, F.; Marino, E.; Guillot, M. Synthesis, Structure and Magnetic Properties of Copper Hydroxysulfates. *Cryst. Eng.* **2002**, *5*, 177–186.

(73) Vilminot, S.; Richard-Plouet, M.; Andre, G.; Swierczynski, D.; Bouree-Vigneron, F.; Kurmoo, M.; André, G.; Swierczynski, D.; Bourée-Vigneron, F.; Kurmoo, M. Nuclear and Magnetic Structures and Magnetic Properties of Synthetic Brochantite, $Cu_4(OH)_6SO_4$. *Dalt. Trans* **2006**, *4* (11), 1455–1462.

(74) Xia, C.; Ning, W. A Novel Bio-Electrochemical Ascorbic Acid Sensor Modified with $Cu_4(OH)_6SO_4$ Nanorods. *Analyst* **2011**, *136* (2), 288–292.

(75) Brigandi, L. M.; Leber, P. A.; Yoder, C. H. Synthesis and Analysis of Copper Hydroxy Double Salts. *J. Chem. Educ.* **2005**, *82* (11), 1662.

(76) Prasad, S. V. S.; Sitakara Rao, V. Thermal Analysis, X-Ray Diffraction and Infrared Spectroscopic Study of Synthetic Brochantite. *J. Therm. Anal.* **1985**, *30* (3), 603–609.

(77) Tanaka, H.; Kawano, M.; Koga, N. Thermogravimetry of Basic copper(II) Sulphates Obtained by Titrating NaOH Solution with $CuSO_4$ Solution. *Thermochim. Acta* **1991**, *182* (2), 281–292.

(78) Candal, R. J.; Regazronib, A. E.; Blesaajb, M. A. Precipitation of Copper (II) Hydrous Oxides and Copper (II) Basic Salts. *J. Mater. Chem.* **1992**, *2*, 657–661.

(79) Jia, W.; Reitz, E.; Sun, H.; Zhang, H.; Lei, Y. Synthesis and Characterization of Novel Nanostructured Fishbone-like $Cu(OH)_2$ and CuO from $Cu_4SO_4(OH)_6$. *Mater. Lett.* **2009**, *63* (5), 519–522.

(80) Kaş, R.; Birer, Ö. Sonochemical Shape Control of Copper Hydroxysulfates. *Ultrason. Sonochem.* **2012**, *19* (3), 692–700.

(81) Jeong, S.; Woo, K.; Kim, D.; Lim, S.; Kim, J. S.; Shin, H.; Xia, Y.; Moon, J. Controlling the Thickness of the Surface Oxide Layer on Cu Nanoparticles for the Fabrication of Conductive Structures by Ink-Jet Printing. *Adv. Funct. Mater.* **2008**, *18* (5), 679–686.

(82) Washio, I.; Xiong, Y.; Yin, Y.; Xia, Y. Reduction by the End Groups of Poly(vinyl Pyrrolidone): A New and Versatile Route to the Kinetically Controlled Synthesis of Ag Triangular Nanoplates. *Adv. Mater.* **2006**, *18* (13), 1745–1749.

(83) Secco, E. A. Spectroscopic Properties of SO4 (and OH) in Different Molecular and Crystalline Environments. I. Infrared Spectra of $Cu_4(OH)_6SO_4$, $Cu_4(OH)_4OSO_4$, and $Cu_3(OH)_4SO_4$. *Can. J. Chem.* **1988**, No. 2, 329–336.

(84) Liu, X.; Zhang, J.; Kang, Y.; Wu, S.; Wang, S. Brochantite Tabular Microspindles and Their Conversion to Wormlike CuO Structures for Gas Sensing. *Cryst EngComm* **2012**, *14* (2), 620–625.

(85) Li, T.; Ai, X. P.; Yang, H. X. Reversible Electrochemical Conversion Reaction of Li_2O/CuO Nanocomposites and Their Application as High-Capacity Cathode Materials for Li-Ion Batteries. *J. Phys. Chem. C* **2011**, *115* (13), 6167–6174.

(86) Prakash, A. S.; Larcher, D.; Morcrette, M.; Hegde, M. S.; Leriche, J. B.; Masquelier, C. Synthesis, Phase Stability, and Electrochemically Driven Transformations in the $LiCuO_2$-Li_2CuO_2 System. *Chem. Mater.* **2005**, *17* (17), 4406–4415.

(87) Marx, N.; Bourgeois, L.; Carlier, D.; Wattiaux, A.; Suard, E.; Le Cras, F.; Croguennec, L. Iron(III) Phosphates Obtained by Thermal Treatment of the Tavorite-Type $FePO_4.H_2O$ Material: Structures and Electrochemical Properties in Lithium Batteries. *Inorg. Chem.* **2012**, *51* (5), 3146–3155.

(88) Kim, K. S. Charge Transfer Transition Accompanying X-Ray Photoionization in Transition-Metal Compounds. *J. Electron Spectros. Relat. Phenomena* **1974**, *3* (3), 217–226.

(89) Hayez, V.; Franquet, A.; Hubin, A.; Terryn, H. XPS Study of the Atmospheric Corrosion of Copper Alloys of Archaeological Interest. *Surf. Interface Anal.* **2004**, *36* (8), 876–879.

(90) Ghijsen, J.; Tjeng, L.; van Elp, J.; Eskes, H.; Westerink, J.; Sawatzky, G.; Czyzyk, M. Electronic Structure of Cu_2O and CuO. *Phys. Rev. B* **1988**, *38* (16), 11322–11330.

(91) Hernandez, J.; Wrschka, P.; Oehrlein, G. S. Surface Chemistry Studies of Copper Chemical Mechanical Planarization. *J. Electrochem. Soc.* **2001**, *148* (7), G389.

(92) Martin, L.; Martinez, H.; Poinot, D.; Pecquenard, B.; Frédéric Le Cras. Comprehensive X-Ray Photoelectron Spectroscopy Study of the Conversion Reaction Mechanism of CuO in Lithiated Thin Film Electrodes. *J. Phys. Chem. C* **2013**, *117*, 4421–4430.

(93) Bodenez, V.; Dupont, L.; Laffont, L.; Armstrong, A. R.; Shaju, K. M.; Bruce, P. G.; Tarascon, J.-M. The Reaction of Lithium with $CuCr_2S_4$—lithium Intercalation and Copper Displacement/extrusion. *J. Mater. Chem.* **2007**, *17* (30), 3238.

(94) Zhao, R.; Yang, T.; Miller, M. A.; Chan, C. K. Electrochemical Properties of Nanostructured Copper Hydroxysulfate Mineral Brochantite upon Reaction with Lithium. *Nano Lett.* **2013**, *13* (12), 6055–6063.

(95) Alpers, C. N.; Nordstrom, D. K.; Ball, J. W. Solubility of Jarosite Solid Solutions Precipitated from Acid Mine Waters, Iron Mountain, California, USA. *Sci. Geol.* **1989**, *42* (4), 281–298.

(96) Dill, H. G. The Geology of Aluminum Phosphate and Sulphates of the Alunite Group Minerals: A Review. *Earth Sci. Rev.* **2001**, *53*, 35–93.

(97) Alpers, C. N.; Jambor, J. L.; Nordstrom, D. K. *Sulfate Minerals: Crystallography, Geochemistry, and Environmental Significance*; Mineralogical Society of America: Washington, DC, 2000.

(98) Das, G. K.; Acharya, S.; Anand, S.; Das, R. P. Jarosites: A Review. *Miner. Process. Extr. Metall. Rev.* **1996**, 185–210.

(99) Bigham, J. M.; Nordstrom, D. K. Iron and Aluminum Hydroxysulfates from Acid Sulfate Waters. *Rev. Mineral. geochemistry* **2000**, *40* (1), 351–403.

(100) Obrovac, M. N.; Christensen, L. Structural Changes in Silicon Anodes during Lithium Insertion/Extraction. *Electrochem. Solid-State Lett.* **2004**, *7* (5), A93–A96.

(101) Klingelhöfer, G.; Morris, R. V.; Bernhardt, B.; Schröder, C.; Rodionov, D. S.; Jr., P. A. de S.; Yen, A.; Gellert, R.; Evlanov, E. N.; Zubkov, B.; et al. Jarosite and Hematite at Meridiani Planum from Opportunity's Mössbauer Spectrometer. *Science.* **2004**, *306*, 1740–1745.

(102) Grohol, D.; Nocera, D. G. Hydrothermal Oxidation-Reduction Methods for the Preparation of Pure and Single Crystalline Alunites: Synthesis and Characterization of a New Series of Vanadium Jarosites. *J. Am. Chem. Soc.* **2002**, *124* (11), 2640–2646.

(103) Dutrizac, E.; Chen, T. Synthesis and Properties of V^{3+} Analogues of Jarosite-Group Minerals. **2003**, *41*, 479–488.

(104) Grohol, D.; Nocera, D.; Papoutsakis, D. Magnetism of Pure Iron Jarosites. *Phys. Rev. B* **2003**, *67*, 1–13.

(105) Gnanavel, M.; Pralong, V.; Lebedev, O. I.; Caignaert, V.; Bazin, P.; Raveau, B. Lithium Intercalation into the Jarosite-Type Hydroxysulfate: A Topotactic Reversible Reaction from a Crystalline Phase to an Inorganic Polymer-like Structure. *Chem. Mater.* **2014**, *26*, 4521–4527.

(106) Ding, Y. L.; Wen, Y.; Van Aken, P. A.; Maier, J.; Yu, Y. Jarosite Nanosheets Fabricated via Room-Temperature Synthesis as Cathode Materials for High-Rate Lithium Ion Batteries. *Chem. Mater.* **2015**, *27* (8), 3143–3149.

(107) Xu, W.; Xie, Z.; Cui, X.; Zhao, K.; Zhang, L.; Mai, L.; Wang, Y. Direct Growth of an Economic Green Energy Storage Material: A Monocrystalline Jarosite-$KFe_3(SO_4)_2(OH)_6$-nanoplates@rGO Hybrid as a Superior Lithium-Ion Battery Cathode. *J. Mater. Chem. A* **2016**, *4* (10), 3735–3742.

(108) Ding, Y. L.; Wen, Y.; Chen, C. C.; Van Aken, P. A.; Maier, J.; Yu, Y. Nanosheets of Earth-Abundant Jarosite as Novel Anodes for High-Rate and Long-Life Lithium-Ion Batteries. *ACS Appl. Mater. Interfaces* **2015**, *7* (19), 10518–10524.

(109) Wills, A. S.; Harrison, A. Structure and Magnetism of Hydronium Jarosite, a Model Kagomé Antiferromagnet. *J. Chem. Soc. Faraday Trans.* **1996**, *92* (12), 2161.

(110) Grohol, D.; Huang, Q.; Toby, B. H.; Lynn, J. W.; Lee, Y. S.; Nocera, D. G. Powder Neutron Diffraction Analysis and Magnetic Structure of Kagomé-Type Vanadium Jarosite $NaV_3(OD)_6(SO_4)_2$. *Phys. Rev. B* **2003**, *68* (9), 94404.

(111) Becker, U.; Gasharova, B. AFM Observations and Simulations of Jarosite Growth at the Molecular Scale: Probing the Basis for the Incorporation of Foreign Ions into Jarosite as a Storage Mineral. *Phys. Chem. Miner.* **2001**, *28* (8), 545–556.

(112) Dobley, A.; Zavalij, P. Y.; Stanley Whittingham, M. Sodium trivanadium(III) Bis(sulfate) Hexahydroxide. *Acta Crystallogr. Sect. C Cryst. Struct. Commun.* **2000**, *56* (11), 1294–1295.

(113) Bigham, J. M.; Jones, F. S.; Özkaya, B.; Sahinkaya, E.; Puhakka, J. A.; Tuovinen, O. H. Characterization of Jarosites Produced by Chemical Synthesis over a Temperature Gradient from 2 to 40 °C. *Int. J. Miner. Process.* **2010**, *94* (3–4), 121–128.

(114) Sandré, A. L.; Gaunand, A. Influence of Semi-Batch Operation on the Precipitation of Natrojarosite Particles from Sulfate Solutions. *J. Cryst. Growth* **2012**, *342* (1), 50–56.

(115) J. E. Dutrizac. Factors Affecting Alkali Jarosite Precipitation. *Metall. Trans. B* **1983**, *14* (4), 531–539.

(116) Dutrizac, J. E.; Jambor, J. L. Behaviour of Cesium and Lithium during the Precipitation of Jarosite-Type Compounds. *Hydrometallurgy* **1987**, *17* (2), 251–265.

(117) Keller, L.; McCarthy, G.; Grant-in-Aid. North Dakota State Univertiy. *Fargo, North Dakota, USA Int. Gentre Diffr. Data Grant-in-Aid* **1984**.

(118) Kato, T. The Crystal Structures of Jarosite and Svanbergite.pdf. *Mineral. J.* **1977**, *8*, 419–430.

(119) Basciano, L. C.; Peterson, R. C. Crystal Chemistry of the Natrojarosite-Jarosite and Natrojarosite-Hydronium Jarosite Solid-Solution Series: A Synthetic Study with Full Fe Site Occupancy. *Am. Mineral.* **2008**, *93* (5–6), 853–862.

(120) Barret, J. *Inorganic Chemistry in Aqueous Solution*; Royal Society of Chemistry, 2003.

(121) Yamakawa, N.; Jiang, M.; Key, B.; Grey, C. P. Identifying the Local Structures Formed during Lithiation of the Conversion Material, Iron Fluoride, in a Li Ion Battery: A Solid-State NMR, X-Ray Diffraction, and Pair Distribution Function Analysis Study. *J. Am. Chem. Soc.* **2009**, *131* (30), 10525–10536.

(122) Liu, J.; Li, Y.; Fan, H.; Zhu, Z.; Jiang, J.; Ding, R.; Hu, Y.; Huang, X. Iron Oxide-Based Nanotube Arrays Derived from Sacrificial Template-Accelerated Hydrolysis: Large-Area Design and Reversible Lithium Storage. *Chem. Mater.* **2010**, *22* (1), 212–217.

(123) Wang, Z.; Luan, D.; Madhavi, S.; Li, C. M.; Lou, X. W. D. α-Fe2O3 Nanotubes with Superior Lithium Storage Capability. *Chem. Commun. (Camb).* **2011**, *47*, 8061–8063.

(124) Xu, S.; Hessel, C. M.; Ren, H.; Yu, R.; Jin, Q.; Yang, M.; Zhao, H.; Wang, D. α-Fe_2O_3 Multi-Shelled Hollow Microspheres for Lithium Ion Battery Anodes with Superior Capacity and Charge Retention. *Energy Environ. Sci.* **2014**, *7*, 632.

(125) Chen, K.; Dong Noh, Y.; Huang, W.; Ma, J.; Komarneni, S.; Xue, D. Microwave-Hydrothermal Synthesis of Fe-Based Materials for Lithium-Ion Batteries and Supercapacitors. *Ceram. Int.* **2014**, *40* (2), 2877–2884.

(126) Sun, B.; Horvat, J.; Kim, H. S.; Kim, W.-S.; Ahn, J.; Wang, G. Synthesis of Mesoporous α-Fe_2O_3 Nanostructures for Highly Sensitive Gas Sensors and High Capacity Anode Materials in Lithium Ion Batteries. *J. Phys. Chem. C* **2010**, *114* (44), 18753–18761.

(127) Setiawati, E.; Hayashi, M.; Tsuda, M.; Hayashi, K.; Kobayashi, R. Electrochemical Properties of Carbon-Composite NASICON-Type Iron Sulfate $Fe_2(SO_4)_3$ as a Cathode for Lithium Secondary Batteries. *J. Power Sources* **2013**, *244*, 207–213.

(128) Gmitter, A. J.; Halajko, A.; Sideris, P. J.; Greenbaum, S. G.; Amatucci, G. G. Subsurface Diffusion of Oxide Electrolyte Decomposition Products in Metal Fluoride Nanocomposite Electrodes. *Electrochim. Acta* **2013**, *88*, 735–744.

(129) Mao, W. -f.; Tang, H. -q.; Tang, Z. -y.; Yan, J.; Xu, Q. Configuration of Li-Ion Vanadium Batteries: $Li_3V_2(PO_4)_3$(cathode) || $Li_3V_2(PO_4)_3$(anode). *ECS Electrochem. Lett.* **2013**, *2* (7), A69–A71.

(130) Hong, H. Crystal Structures and Crystal Chemistry in the System $Na_{1+x}Zr_2Si_xP_{3-x}O_{12}$. *Mater. Res. Bull.* **1976**, *11* (2), 173–182.

(131) Goodenough, J. B.; Hong, H. Y.; Kafalas, J. A. Fast Na^+ Ion Transport in Skeleton Structures. *Mat. Res. Bull.* **1976**, *11* (2), 203–220.

(132) Meunier, M.; Izquierdo, R.; Hasnaoui, L.; Quenneville, E.; Ivanov, D.; Girard, F.; Morin, F.; Yelon, A.; Paleologou, M. Pulsed Laser Deposition of Superionic Ceramic Thin Films: Deposition and Applications in Electrochemistry. *Appl. Surf. Sci.* **1998**, *127–129*, 466–470.

(133) Yao, S.; Shimizu, Y.; Miura, N.; Yamazoe, N. Solid Electrolyte CO_2 Sensor Using Binary Carbonate Electrode. *Chem. Lett.* **1990**, *19* (11), 2033–2036.

(134) SAITO, Y.; Maruyama, T. Recent Developments of the Sensors for Carbon Oxides Using Solid Electrolytes. *Solid State Ionics* **1988**, *28–30*, 1644–1647.

(135) Aono, H. Ionic Conductivity of Solid Electrolytes Based on Lithium Titanium Phosphate. *J. Electrochem. Soc.* **1990**, *137* (4), 1023–1027.

(136) Imanishi, N.; Hasegawa, S.; Zhang, T.; Hirano, A.; Takeda, Y.; Yamamoto, O. Lithium Anode for Lithium-Air Secondary Batteries. *J. Power Sources* **2008**, *185* (2), 1392–1397.

(137) Feng, J.; Xia, H.; Lai, M. O.; Lu, L. NASICON-Structured $LiGe_2(PO_4)_3$ with Improved Cyclability for High-Performance Lithium Batteries. *J. Phys. Chem. C* **2009**, *113* (47), 20514–20520.

(138) Delmas, C.; Cherkaoui, F.; Nadiri, A.; Hagenmuller, P. A Nasicon-Type Phase as Intercalation Electrode: $NaTi_2(PO_4)_3$. *Mater. Res. Bull.* **1987**, *22* (5), 631–639.

(139) Aatiq, A.; Delmas, C.; El Jazouli, A.; Gravereau, P. Structure and Electrochemical Study of $Li_{2x}Mn_{(1-x)}TiCr(PO_4)_3$ (x=0-0.50) with Nasicon-like Structure. *Ann. Chim. Sci. Mat.* **1998**, *23*, 121–124.

(140) Aatiq, A.; Delmas, C.; El Jazouli, A. Structural and Electrochemical Study of $Li_{0.5}Mn_{0.5}Ti_{1.5}Cr_{0.5}(PO_4)_3$. *J. Solid State Chem.* **2001**, *158* (2), 169–174.

(141) Masquelier, C.; Padhi, A.; Nanjundaswamy, K.; Goodenough, J. B. New Cathode Materials for Rechargeable Lithium Batteries: The 3-D Framework Structures $Li_3Fe_2(XO_4)_3$(X=P, As). *J. Solid State Chem.* **1998**, *135* (2), 228–234.

(142) Delmas, C.; Nadiri, A.; Soubeyroux, J. L. The Nasicon-Type Titanium Phosphates $ATi_2(PO_4)_3$ (A= Li, Na) as Electrode Materials. *Solid State Ionics* **1988**, *28*, 419–423.

(143) Luo, J.-Y.; Cui, W.-J.; He, P.; Xia, Y.-Y. Raising the Cycling Stability of Aqueous Lithium-Ion Batteries by Eliminating Oxygen in the Electrolyte. *Nat. Chem.* **2010**, *2* (9), 760–765.

(144) Wessells, C.; Huggins, R. A.; Cui, Y. Recent Results on Aqueous Electrolyte Cells. *J. Power Sources* **2011**, *196* (5), 2884–2888.

(145) Zhang, T.; Imanishi, N.; Hasegawa, S.; Hirano, A.; Xie, J.; Takeda, Y.; Yamamoto, O.; Sammes, N. Li⁄polymer Electrolyte⁄water Stable Lithium-Conducting Glass Ceramics Composite for Lithium–air Secondary Batteries with an Aqueous Electrolyte. *J. Electrochem. Soc.* **2008**, *155* (12), A965–A969.

(146) Xu, X.; Yang, T.; Shui, M.; Lu, Z.; Gao, S.; Shu, J.; Zheng, W.; Cheng, L.; Feng, L.; Ren, Y. The Preparation and Lithium Mobility of Zinc Based NASICON-Type Solid Electrolyte $Li_{1+2x+2y}Al_xZn_yTi_{2-x-y}Si_xP_{3-x}O_{12}$. *Ceram. Int.* **2014**, *40* (2), 3819–3822.

(147) S. Wong, P. J. Newman, A. S. Best, K. M. Nairn, D. R. M.; Forsyth, M. Towards Elucidating Microscopic Structural Changes in Li-Ion Conductors $Li_{1+y}Ti_{2-y}Al_y[PO_4]_3$ and $Li_{1+y}Ti_{2-y}Al_y[PO_4]_{3-x}[MO_4]_x$ (M=V and Nb): X-Ray and ^{27}Al and ^{31}P NMR Studies. *J. Mater. Chem.* **1998**, *8* (10), 2199–2203.

(148) Best, A. S.; Newman, P. J.; MacFarlane, D. R.; Nairn, K. M.; Wong, S.; Forsyth, M. Characterisation and Impedance Spectroscopy of Substituted $Li_{1.3}Al_{0.3}Ti_{1.7}(PO_4)_{3-x}(ZO_4)_x$ (Z = V, Nb) Ceramics. *Solid State Ionics* **1999**, *126* (1), 191–196.

(149) Forsyth, M.; Wong, S.; Nairn, K. M.; Best, A. S.; Newman, P. J.; Macfarlane, D. R. NMR Studies of Modified Nasicon-Like, Lithium Conduction Solid Electrolytes. *Solid State Ionics* **1999**, *124* (9), 213–219.

(150) Manthiram, A.; Goodenough, J. B. Lithium Insertion into $Fe_2(SO_4)_3$ Frameworks. *J. Power Sources* **1989**, *26* (3), 403–408.

(151) Padhi, A. K.; Manivannan, V.; Goodenough, J. B. Tuning the Position of the Redox Couples in Materials with NASICON Structure by Anionic Substitution. *J. Electrochem. Soc.* **1998**, *145* (5), 1518–1520.

(152) Patoux, S.; Masquelier, C. Lithium Insertion into Titanium Phosphates, Silicates, and Sulfates. *Chem. Mater.* **2002**, *14* (12), 5057–5068.

(153) Mieritz, D.; Davidowski, S. K.; Seo, D. K. Accessing Alkali-Free NASICON-Type Compounds through Mixed Oxoanion Sol-Gel Chemistry: Hydrogen Titanium Phosphate Sulfate, $H_{1-x}Ti_2(PO_4)_{3-x}(SO_4)_x$ (x=0.5-1). *J. Solid State Chem.* **2016**, *242*, 116–125.

(154) Aatiq, A.; Ménétrier, M.; Croguennec, L.; Suard, E.; Delmas, C. On the Structure of $Li_3Ti_2(PO_4)_3$. *J. Mater. Chem.* **2002**, *12* (10), 2971–2978.

(155) Halsey, G. Physical Adsorption on Non-Uniform Surfaces. *J. Chem. Phys.* **1948**, *16*, 931–937.

(156) Catti, M.; Ibberson, R. M. Order-Disorder of the Hydronium Ion and Low-Temperature Phase Transition of $(H_3O)Zr_2(PO_4)_3$ NASICON by Neutron Diffraction. *J. Phys. Chem. B* **2002**, *106* (46), 11916–11921.

(157) Bove, L. E.; Catti, M.; Paciaroni, A.; Sacchetti, F. Neutron Scattering Study of the Dynamics of Hydronium Ion in $(H_3O)Zr_2(PO_4)_3$ Nasicon across the Order - Disorder Transition. *J. Phys. Chem. B* **2004**, *108* (26), 8910–8914.

(158) Aatiq, A.; Menetrier, M.; El Jazouli, A.; Delmas, C. Structural and Lithium Intercalation Studies of $Mn_{(0.5-x)}Ca_xTi_2(PO_4)_3$ Phases ($0<X<0.50$). *Solid State Ionics* **2002**, *150*, 391–405.

(159) Patoux, S.; Masquelier, C. Lithium Insertion into Titanium Phosphates, Silicates and Sulfates. *Chem Mater* **2002**, *14* (16), 5057–5068.

(160) Schmidt, J. P.; Chrobak, T.; Ender, M.; Illig, J.; Klotz, D.; Ivers-Tiffée, E. Studies on $LiFePO_4$ as Cathode Material Using Impedance Spectroscopy. *J. Power Sources* **2011**, *196* (12), 5342–5348.

(161) Hu, S.; Li, Y.; Yin, J.; Wang, H.; Yuan, X.; Li, Q. Effect of Different Binders on Electrochemical Properties of $LiFePO_4$/C Cathode Material in Lithium Ion Batteries. *Chem. Eng. J.* **2014**, *237*, 497–502.

(162) Chen, S. Z.; Zhang, P. Y.; Zhu, W. P.; Chen, L.; Xu, S. M. Deactivation of TiO_2 Photocatalytic Films Loaded on Aluminium: XPS and AFM Analyses. *Appl. Surf. Sci.* **2006**, *252* (20), 7532–7538.

(163) Raj, K. J. A.; Shanmugam, R.; Mahalakshmi, R.; Viswanathan, B. XPS and IR Spectral Studies on the Structure of Phosphate and Sulphate Modified Titania - A Combined DFT and Experimental Study. *Indian J. Chem. - Sect. A Inorganic, Phys. Theor. Anal. Chem.* **2010**, *49* (1), 9–17.

(164) Shi, Z.; Wang, Q.; Ye, W.; Li, Y.; Yang, Y. Synthesis and Characterization of Mesoporous Titanium Pyrophosphate as Lithium Intercalation Electrode Materials. *Microporous Mesoporous Mater.* **2006**, *88* (1–3), 232–237.

(165) Nocuń, M. Structural Studies of Phosphate Glasses with High Ionic Conductivity. *J. Non. Cryst. Solids* **2004**, *333* (1), 90–94.

(166) Senguttuvan, P.; Rousse, G.; Arroyo Y De Dompablo, M. E.; Vezin, H.; Tarascon, J. M.; Palacín, M. R. Low-Potential Sodium Insertion in a Nasicon-Type Structure through the Ti(III)/Ti(II) Redox Couple. *J. Am. Chem. Soc.* **2013**, *135* (10), 3897–3903.

(167) Park, S. Il; Gocheva, I.; Okada, S.; Yamaki, J. Electrochemical Properties of $NaTi_2(PO_4)_3$ Anode for Rechargeable Aqueous Sodium-Ion Batteries. *J. Electrochem. Soc.* **2011**, *158* (10), A1067–A1070.

(168) Zhou, M.; Liu, L.; Yi, L.; Yang, Z.; Mao, S.; Zhou, Y.; Hu, T.; Yang, Y.; Shen, B.; Wang, X. Synthesis of $LiTi_2(PO_4)_3$-Acetylene Black Nanocomposites for Lithium Ion Batteries by the Polyvinyl Alcohol Assisted Sol-Gel Method and Ball-Milling. *J. Power Sources* **2013**, *234*, 292–301.

(169) Shaju, K. M.; Subba Rao, G. V.; Chowdari, B. V. R. Influence of Li-Ion Kinetics in the Cathodic Performance of Layered $Li(Ni_{1/3}Co_{1/3}Mn_{1/3})O_2$. *J. Electrochem. Soc.* **2004**, *151* (9), A1324.

(170) Prosini, P. P.; Lisi, M.; Zane, D.; Pasquali, M. Determination of the Chemical Diffusion Coefficient of Lithium in $LiFePO_4$. *Solid State Ionics* **2002**, *148* (1–2), 45–51.

(171) Kasper, J. S.; Hagenmuller, P.; Pouchard, M.; Cros, C. Clathrate Structure of Silicon Na_8Si_{46} and Na_xSi_{136} (x<11). *Science.***1965**, *150*, 1713–1714.

(172) Kawaji, H.; Horie, H.; Yamanaka, S.; Ishikawa, M. Superconductivity in the Silicon Clathrate Compound $(Na, Ba)_xSi_{46}$. *Phys. Rev. Lett.* **1995**, *74* (8), 1427–1429.

(173) Reny, E.; San-Miguel, A.; Guyot, Y.; Masenelli, B.; Mélinon, P.; Saviot, L.; Yamanaka, S.; Champagnon, B.; Cros, C.; Pouchard, M.; et al. Vibrational Modes in Silicon Clathrate Compounds: A Key to Understanding Superconductivity. *Phys. Rev. B* **2002**, *66* (1), 14532.

(174) Connétable, D.; Timoshevskii, V.; Masenelli, B.; Beille, J.; Marcus, J.; Barbara, B.; Saitta, A. M.; Rignanese, G.-M.; Mélinon, P.; Yamanaka, S.; et al. Superconductivity in Doped sp^3 Semiconductors: The Case of the Clathrates. *Phys. Rev. Lett.* **2003**, *91* (24), 247001.

(175) Kume, K.; Kawaji, H.; Yamanaka, S.; Ishikawa, M. NMR Study in the Superconducting Silicon Clathrate Compound NaxBaySi46. *Phys. Rev. B* **1996**, *54* (18), 242–246.

(176) Herrmann, F. W. Superconductivity in Silicon Based Barium-Inclusion Clathrates. *Chem. Phys. Lett.* **1998**, *283* (January), 29–32.

(177) Yamanaka, S.; Enishi, E.; Fukuoka, H.; Yasukawa, M. High-Pressure Synthesis of a New Silicon Clathrate Superconductor, Ba 8Si 46. *Inorg. Chem.* **2000**, *39* (1), 56–58.

(178) Kume, T.; Fukuoka, H.; Koda, T.; Sasaki, S.; Shimizu, H.; Yamanaka, S. High-Pressure Raman Study of Ba Doped Silicon Clathrate. *Phys. Rev. Lett.* **2003**, *90* (15), 155503.

(179) Fukuoka, H.; Kiyoto, J.; Yamanaka, S. Superconductivity of Metal Deficient Silicon Clathrate Compounds, Ba8-xSi46 ($0 < X < 1.4$). *Inorg. Chem.* **2003**, *42* (9), 2933–2937.

(180) Toulemonde, P.; Adessi, C.; Blase, X.; San Miguel, A.; Tholence, J. L. Superconductivity in the $(Ba_{1-x}Sr_x)_8Si_{46}$ Clathrates ($x \leq 0.75$): Experimental and Ab Inito Investigation. *Phys. Rev. B* **2005**, *71* (9), 94504.

(181) Blake, N. P.; Mollnitz, L.; Kresse, G.; Metiu, H. Why Clathrates Are Good Thermoelectrics: A Theoretical Study of $Sr_8Ga_{16}Ge_{30}$. *J. Chem. Phys.* **1999**, *111* (7), 3133–3144.

(182) Nolas, G. S.; Slack, G. A.; Schujman, S. B. Chapter 6 Semiconductor Clathrates: A Phonon Glass Electron Crystal Material with Potential for Thermoelectric Applications. *Semicond. Semimetals* **2001**, *69*, 255–300.

(183) Tsujii, N.; Roudebush, J. H.; Zevalkink, A.; Cox-Uvarov, C. A.; Jeffery Snyder, G.; Kauzlarich, S. M. Phase Stability and Chemical Composition Dependence of the Thermoelectric Properties of the Type-I Clathrate $Ba_8Al_xSi_{46-x}$ ($8 \leq x \leq 15$). *J. Solid State Chem.* **2011**, *184* (5), 1293–1303.

(184) Condron, C. L.; Martin, J.; Nolas, G. S.; Piccoli, P. M. B.; Schultz, A. J.; Kauzlarich, S. M. Structure and Thermoelectric Characterization of Ba8Al14Si31. *Inorg. Chem.* **2006**, *45* (23), 9381–9386.

(185) Condron, C. L.; Kauzlarich, S. M.; Nolas, G. S. Structure and Thermoelectric Characterization of $A_xBa_{8-x}Al_{14}Si_{31}$ (A = Sr, Eu) Single Crystals. *Inorg. Chem.* **2007**, *46* (7), 2556–2562.

(186) Condron, C. L.; Kauzlarich, S. M.; Ikeda, T.; Jeffery Snyder, G.; Haarmann, F.; Jeglic, P. Synthesis, Structure, and High-Temperature Thermoelectric Properties of Boron-Doped $Ba_8Al_{14}Si_{31}$ Clathrate I Phases. *Inorg. Chem.* **2008**, *47* (18), 8204–8212.

(187) Christensen, M.; Johnsen, S.; Iversen, B. B. Thermoelectric Clathrates of Type I. *Dalton Trans.* **2010**, *39* (4), 978–992.

(188) Cros, C.; Pouchard, M.; Hagenmuller, P. Sur Une Nouvelle Famille de Clathrates Mineraux Isotypes Des Hydrates de Gaz et de Liquides. Interpretation Des Resultats Obtenus. *J. Solid State Chem.* **1970**, *2* (4), 570–581.

(189) Mott, N. F. Properties of Compounds of Type NaxSi46 and Na_xSi_{136}. *J. Solid State Chem.* **1973**, *6* (3), 348–351.

(190) Neiner, D.; Okamoto, N. L.; Condron, C. L.; Ramasse, Q. M.; Yu, P.; Browning, N. D.; Kauzlarich, S. M. Hydrogen Encapsulation in a Silicon Clathrate Type I Structure: $Na_{5.5}(H_2)_{2.15}Si_{46}$: Synthesis and Characterization. *J. Am. Chem. Soc.* **2007**, *129* (45), 13857–13862.

(191) Neiner, D.; Okamoto, N. L.; Yu, P.; Leonard, S.; Condron, C. L.; Toney, M. F.; Ramasse, Q. M.; Browning, N. D.; Kauzlarich, S. M. Synthesis and Characterization of $K_{8-x}(H_2)_ySi_{46}$. *Inorg. Chem.* **2010**, *49* (3), 815–822.

(192) San-Miguel, A.; Kéghélian, P.; Blase, X.; Mélinon, P.; Perez, A.; Itié, J.; Polian, A.; Reny, E.; Cros, C.; Pouchard, M. High Pressure Behavior of Silicon Clathrates: A New Class of Low Compressibility Materials. *Phys. Rev. Lett.* **1999**, *83* (25), 5290–5293.

(193) Eisenmann, B.; Schäfer, H.; Zagler, R. Die Verbindungen $A_8^{II}B_{16}^{III}B_{30}^{IV}$ (A^{II}=Sr,Ba; B^{III}=Al,Ga; B^{IV}=Si,Ge,Sn) Und Ihre Kafigstrukturen. *J. Less-Common Met.* **1986**, *118*, 43.

(194) Cordier, G.; Woll, P. Neue Ternäre Intermetallische Verbindungen Mit Clathratstruktur: $Ba_8(T,Si)_6Si_{40}$ Und $Ba_6(T,Ge)_6Ge_{40}$ Mit T ≡ Ni, Pd, Pt, Cu, Ag, Au. *J. Less-Common Met.* **1991**, *169* (2), 291–302.

(195) Yan, X.; Giester, G.; Bauer, E.; Rogl, P.; Paschen, S. Ba-Cu-Si Clathrates: Phase Equilibria and Crystal Chemistry. *J. Electron. Mater.* **2010**, *39* (9), 1634–1639.

(196) Schafer, H. On the Problem of Polar Intermetallic Compounds: The Stimulation of E. Zintl's Work for the Modern Chemistry of Intermetallics. *Ann. Rev. Mater. Sci.* **1985**, *15*, 1–41.

(197) Li, Y.; Raghavan, R.; Wagner, N. a.; Davidowski, S. K.; Baggetto, L.; Zhao, R.; Cheng, Q.; Yarger, J. L.; Veith, G. M.; Ellis-Terrell, C.; et al. Type I Clathrates as Novel Silicon Anodes: An Electrochemical and Structural Investigation. *Adv. Sci.* **2015**, *2* (6), 1500057.

(198) Wagner, N. A.; Raghavan, R.; Zhao, R.; Wei, Q.; Peng, X.; Chan, C. K. Electrochemical Cycling of Sodium-Filled Silicon Clathrate. *ChemElectroChem* **2014**, *1* (2), 347–353.

(199) Peng, X.; Wei, Q.; Li, Y.; Chan, C. K. First-Principles Study of Lithiation of Type I Ba-Doped Silicon Clathrates. *J. Phys. Chem. C* **2015**, *119* (51), 28247–28257.

(200) Mudryk, Y.; Rogl, P.; Paul, C.; Berger, S.; Bauer, E.; Hilscher, G.; Godart, C.; Noel, H. Thermoelectricity of Clathrate I Si and Ge Phases. *J.phys. Condens. Matter* **2002**, *14*, 7991–8004.

(201) Okamoto, N. L.; Oh, M. W.; Nishii, T.; Tanaka, K.; Inui, H. Crystal Structure and Thermoelectric Properties of the Type-I Clathrate Compound Ba_8Ge_{43} with an Ordered Arrangement of Ge Vacancies. *J. Appl. Phys.* **2006**, *99* (3).

(202) Kaltzoglou, A.; Hoffmann, S. D.; Fässler, T. F. Order-Disorder Phase Transition in Type-I Clathrate $Cs_8Sn_{44}\square_2$. *Eur. J. Inorg. Chem.* **2007**, No. 26, 4162–4167.

(203) Liu, B.; Jia, X.; Sun, H.; Sun, B.; Zhang, Y.; Liu, H.; Kong, L.; Huo, D.; Ma, H. HPHT Synthesis, Structure and Electrical Properties of Type-I Clathrates $Ba_8Al_xSi_{46-x}$. *J. Solid State Chem.* **2016**, *233*, 363–367.

(204) Aydemir, U.; Candolfi, C.; Ormeci, A.; Borrmann, H.; Burkhardt, U.; Oztan, Y.; Oeschler, N.; Baitinger, M.; Steglich, F.; Grin, Y. Synthesis, Crystal Structure, and Physical Properties of the Type-I Clathrate $Ba_{8-\delta}Ni_{x\square y}Si_{46-x-y}$. *Inorg. Chem.* **2012**, *51*, 4730–4741.

(205) Anno, H.; Shirataki, R. Effect of Heat Treatment in Air on the Surface of a Sintered $Ba_8Al_{16}Si_{30}$-Based Clathrate. *J. Electron. Mater.* **2014**, *43* (6), 1847–1856.

(206) Nagatomo, Y.; Mugita, N.; Nakakohara, Y.; Saisho, M.; Tajiri, M.; Teranishi, R.; Munetoh, S. Thermoelectric Properties of Single Crystalline $Ba_8Al_xSi_{46-x}$ clathrate by Using Flux Czochralski Method. *J. Phys. Conf. Ser.* **2012**, *379* (1), 12008.

(207) Barr, T. L. An XPS Study of Si as It Occurs in Adsorbents, Catalysts, and Thin Films. *Appl. Surf. Sci.* **1983**, *15* (1–4), 1–35.

(208) He, J.; Klug, D. D.; Uehara, K.; Preston, K. F.; Ratcliffe, C. I.; Tse, J. S. NMR and X-Ray Spectroscopy of Sodium−Silicon Clathrates. *J. Phys. Chem. B* **2001**, *105* (17), 3475–3485.

(209) Kume, T.; Koda, T.; Sasaki, S.; Shimizu, H.; Tse, J. S. High-Pressure Raman Study of the Potassium-Doped Silicon Clathrate K_8Si_{46}. *Phys. Rev. B - Condens. Matter Mater. Phys.* **2004**, *70* (5), 1–4.

(210) Shimizu, H.; Kume, T.; Kuroda, T.; Sasaki, S.; Fukuoka, H.; Yamanaka, S. High-Pressure Raman Study of the Ba-Doped Silicon Clathrate $Ba_{24}Si_{100}$ up to 27 GPa. *Phys. Rev. B - Condens. Matter Mater. Phys.* **2005**, *71* (9), 1–5.

(211) Condron, C. L.; Porter, R.; Guo, T.; Kauzlarich, S. M. Crystal Structures, Raman Spectroscopy, and Magnetic Properties of $Ba_{7.5}Al_{13}Si_{29}$ and $Eu_{0.27}Ba_{7.22}Al_{13}Si_{29}$. *Inorg. Chem.* **2005**, *44* (25), 9185–9191.

(212) Schroder, K. W.; Celio, H.; Webb, L. J.; Stevenson, K. J. Examining Solid Electrolyte Interphase Formation on Crystalline Silicon Electrodes: Influence of Electrochemical Preparation and Ambient Exposure Conditions. *J. Phys. Chem. C* **2012**, *116* (37), 19737–19747.

(213) Ding, N.; Xu, J.; Yao, Y. X.; Wegner, G.; Fang, X.; Chen, C. H.; Lieberwirth, I. Determination of the Diffusion Coefficient of Lithium Ions in Nano-Si. *Solid State Ionics* **2009**, *180* (2–3), 222–225.

(214) Nguyen, S. H.; Lim, J. C.; Lee, J. K. Electrochemical Characteristics of Bundle-Type Silicon Nanorods as an Anode Material for Lithium Ion Batteries. *Electrochim. Acta* **2012**, *74*, 53–58.

(215) Simon, P.; Gogotsi, Y. Materials for Electrochemical Capacitors. *Nat. Mater.* **2008**, *7* (11), 845–854.

(216) Li, J.; Dahn, J. R. An in Situ X-Ray Diffraction Study of the Reaction of Li with Crystalline Si. *J. Electrochem. Soc.* **2007**, *154* (3), A156–A161.

(217) Hatchard, T. D.; Dahn, J. R. In Situ XRD and Electrochemical Study of the Reaction of Lithium with Amorphous Silicon. *J. Electrochem. Soc.* **2004**, *151* (6), A838–A842.

(218) Kim, T.; Park, S.; Oh, S. M. Solid-State NMR and Electrochemical Dilatometry Study on Li^+ Uptake/Extraction Mechanism in SiO Electrode. *J. Electrochem. Soc.* **2007**, *154* (12), A1112.

(219) Warrier, P.; Koh, C. A. Silicon Clathrates for Lithium Ion Batteries: A Perspective. *Appl. Phys. Rev.* **2016**, *3* (4), 40805.

(220) Huggins, R. a.; Nix, W. D. Decrepitation Model for Capacity Loss during Cycling of Alloys in Rechargeable Electrochemical Systems. *Ionics (Kiel).* **2000**, *6* (1–2), 57–63.

(221) Lee, S. W.; McDowell, M. T.; Berla, L. A.; Nix, W. D.; Cui, Y. Fracture of Crystalline Silicon Nanopillars During Electrochemical Lithium Insertion. *Proc. Natl. Acad. Sci. U. S. A.* **2012**, *109*, 4080–4085.

(222) Jan Curda, Wilder Carrillo-Cabrera, Andre Schmeding, Karl Peters, M. S.; Schnering, H. G. von. Tribarium Tetrahedro-Tetragermanide Acetylenide, $Ba_3[Ge_4][C_2]$: Synthesis, Structure, and Properties. *Z. Anorg. Allg. Chem.* **1997**, *623*, 929–936.

(223) Carrillo-Cabrera, W.; Curda, J.; Peters, K.; Paschen, S.; Baenitz, M.; Grin, Y.; Schnering, H. G. von. Crystal Structure of the Defect Clathrate-I, Ba_8Ge_{43}. *Z. Krist. NCS* **2000**, *215*, 321–322.

(224) Carrillo-Cabrera, W.; Budnyk, S.; Prots, Y.; Grin, Y. Ba8Ge43 Revisited: A 2a'x2a'x2a' Superstructure of the Clathrate-I Type with Full Vacancy Ordering. *Zeitschrift fur Anorg. und Allg. Chemie* **2004**, *630* (13–14), 2267–2276.

(225) Gou, W.; Rodriguez, S. Y.; Li, Y.; Ross, J. H. NMR Experiments and Electronic Structure Calculations in Type-I BaAlGe Clathrates. *Phys. Rev. B - Condens. Matter Mater. Phys.* **2009**, *80* (14), 1–9.

(226) Liang, Y.; Böhme, B.; Ormeci, A.; Borrmann, H.; Pecher, O.; Haarmann, F.; Schnelle, W.; Baitinger, M.; Grin, Y. A Clathrate-I Phase with Li-Ge Framework. *Chem. - A Eur. J.* **2012**, *18* (32), 9818–9822.

(227) Yoon, S.; Park, C.-M.; Sohn, H.-J. Electrochemical Characterizations of Germanium and Carbon-Coated Germanium Composite Anode for Lithium-Ion Batteries. *Electrochem. Solid-State Lett.* **2008**, *11* (4), A42.

(228) Chockla, A. M.; Klavetter, K. C.; Mullins, C. B.; Korgel, B. A. Solution-Grown Germanium Nanowire Anodes for Lithium-Ion Batteries. *ACS Appl. Mater. Interfaces* **2012**, *4* (9), 4658–4664.

(229) Baggetto, L.; Notten, P. H. L. Lithium-Ion (De)Insertion Reaction of Germanium Thin-Film Electrodes: An Electrochemical and In Situ XRD Study. *J. Electrochem. Soc.* **2009**, *156* (3), A169–A175.

(230) Dünner, J.; Mewis, A. Ba8Cu16P30.-A New Ternary Variant of the Clathrate I Type Structure. *ChemInform* **1995**, *26* (24).

(231) Dolyniuk, J. A.; Wang, J.; Lee, K.; Kovnir, K. Twisted Kelvin Cells and Truncated Octahedral Cages in the Crystal Structures of Unconventional Clathrates, AM_2P_4 (A = Sr, Ba; M = Cu, Ni). *Chem. Mater.* **2015**, *27* (12), 4476–4484.

(232) Kim, Y.; Park, Y.; Choi, A.; Choi, N. S.; Kim, J.; Lee, J.; Ryu, J. H.; Oh, S. M.; Lee, K. T. An Amorphous Red Phosphorus/carbon Composite as a Promising Anode Material for Sodium Ion Batteries. *Adv. Mater.* **2013**, *25* (22), 3045–3049.

(233) Sun, L.-Q.; Li, M.-J.; Sun, K.; Yu, S.-H.; Wang, R.-S.; Xie, H.-M. Electrochemical Activity of Black Phosphorus as an Anode Material for Lithium-Ion Batteries. *J. Phys. Chem. C* **2012**, *116* (28), 14772–14779.

(234) Park, C.-M.; Sohn, H.-J. Black Phosphorus and Its Composite for Lithium Rechargeable Batteries. *Adv. Mater.* **2007**, *19* (18), 2465–2468.

APPENDIX

A STATEMENT OF COAUTHORS` PERMISSIONS

I, Ran Zhao, committed that all co-authors have granted their permissions for the usage of following publications in this dissertation.

(1) R. Zhao, T. Yang, M.A. Miller, C.K. Chan, Electrochemical Properties of Nanostructured Copper Hydroxysulfate Mineral Brochantite upon Reaction with Lithium, *Nano Lett*. 13 (2013) 6055–6063.

(2) Zhao, Y. Li, C.K. Chan, Synthesis of Jarosite and Vanadium Jarosite Analogues using Microwave Hydrothermal Reaction and Evaluation of Composition-Dependent Electrochemical Properties, *J. Phys. Chem. C*. 120 (2016) 9702–9712.

(3) R. Zhao, D. Mieritz, D.-K. Seo, C.K. Chan, New Hydrogen Titanium Phosphate Sulfate Electrodes for Li-ion and Na-ion Batteries, *J. Power Sources*. 343 (2017) 197–206.